

Single Cell Pico Force Microscopy – A novel tool for high resolution measurement of cell forces

Thesis by

Blake Waters Axelrod

In Partial Fulfillment of the Requirements

for the Degree of

Doctor of Philosophy

California Institute of Technology

Pasadena, California

2009

(Defended January 28, 2009)

© 2009

Blake Waters Axelrod

All Right Reserved

Acknowledgement

I dedicate this thesis to my wife, Jenifer. I could not have done it without her support, perspective and humor.

I am also deeply indebted to my advisor, Michael Roukes, for posing a fascinating and meaningful problem to solve, handing me a seemingly bottomless box of tools and resources, and then being willing and able to get out of the way so that I could muddle along on my own time and ultimately learn a few things. John Tan played an enormously important role in the early conceptualization of Single Cell Pico Force Microscopy, his experience measuring forces from adherent cells was critical to building a strong foundation for the project. Scott Fraser also provided a number of important and insightful suggestions along the way; I am very appreciative of his ability to focus fully on my work when I am talking to him about it.

I am very grateful to a number of Caltech staff, the unsung heroes, who quietly make everything that goes on here possible. I thank Exie Marie Leagons for keeping the Roukes Group humming smoothly. I thank Steve Stryker and Nils Asplund for their problem solving and machining abilities, which have been so central to my work. I thank Ali Ghaffari for the work he does keeping the Watson cleanroom clean and functional, without which I could never have done the quality microfluidics or photo lithography work necessary for my research. I thank Guy Derosé for his efforts maintaining the EBPG. I also owe many thanks to Marilyn Kushner of the Berkeley MicroLab whose mask making service has also been critical to my research.

Finally, I thank my parents for raising me with the quixotic self confidence necessary to start and finish both a Ph.D. and such a complex research project.

Abstract

Nearly all eukaryotic cells exert forces on their surroundings to generate and maintain tension within their cytoskeleton which is critical for normal cell function. In addition, cells exert forces on their surroundings to orient themselves within an organism, thus gaining information that influences cell fate and behavior, a process called mechanotransduction. In order to study mechanotransduction, a tool is needed that can observe the molecular level sensing events that trigger a decision by a cell as well as the ultimate response that occurs on the whole cell level. There are a number of optical techniques that are used to measure forces from adherent cells at the single cell level; some are good for measuring whole cell forces and some for measuring single molecule level forces, but none have the dynamic range necessary to span both regimes, which is critical for understanding mechanotransduction. To address this need, I have developed a Nano-ElectroMechanical Systems (NEMS) based tool, Single-Cell-Pico-Force-Microscopy (SCPFM), that measures forces exerted by adherent cells with macro-molecular level force sensitivity and sufficient dynamic range to monitor whole cell responses to stimuli with macro-molecular resolution. I have used SCPFM to measure force versus time data from a NIH-3T3 fibroblast as it is perturbed with Cytochalasin D (CD) and allowed to recover in growth media. Within the data there are three excellent examples of previously inaccessible molecular-mechanical processes that illustrate the immense potential of SCPFM to significantly enhance resolution of cell biology at the single cell level: 1) an initial contraction upon exposure to CD followed by the expected force drop, 2) small force oscillations, roughly 400pN peak-to-peak, with frequency that is monotonically dependent on the force being exerted by the lamellipodia, and 3) large, stable, quantized force steps of order 1nN are manifested when a cell's cytoskeleton is perturbed with CD and allowed to recover in growth media. I propose two complimentary experimental efforts to undertake: a systematic effort to build a library of molecular-mechanical force signatures of various common cytoskeleton reactions and an effort to stimulate and observe compliance sensing and response in adherent cells.

Table of contents

1. Introduction	1
2. Cell forces and mechanotransduction	6
2.1 Why cells exert forces	6
2.2 How cells exert forces	8
2.3 By the numbers	10
2.4 Existing technologies	11
3. The tool: Single-Cell-Pico-Force-Microscopy	15
3.1 The goal	15
3.2 The NEMS force sensor	16
3.2.1 The spring constant	17
3.2.2 Strain in the piezoresistor	18
3.2.3 The Wheatstone bridge and transducer responsivity	18
3.2.4 Noise I: piezoresistor noise	20
3.2.5 Instrumentation I & noise II: bandwidth and voltage noise	21
3.2.6 Device optimization: dependence of force resolution on geometry	23
3.2.7 Instrumentation II: nulling and dynamic range	28
3.2.8 Thermal drifts	30
3.3 Device fabrication	31
3.3.1 Fabrication basics	31
3.3.1.1 SU-8	33
3.3.1.2 Polyimide	34
3.3.1.3 Parylene	34
3.3.2 The all-polymer process	35

3.3.3 SiN membrane process	41
3.4 Microfluidics	50
3.5 Surface control	55
3.6 Sample holder and incubator	63
3.7 Tissue culture in microfluidics	64
3.7.1 Temperature	66
3.7.2 Carbon dioxide	67
3.7.3 Feeding/media exchange	67
3.7.4 Materials	68
3.7.5 Cell chamber shape	69
3.7.6 Conditioned media	69
3.7.7 Fluorescence microscopy	69
3.7.8 Tissue culture summary	70
3.8 Recap & future directions	71
4. Proof of principle	73
4.1 Basic idea	73
4.2 Cytochalasin	75
4.3 Comparison with mPADs	75
4.4 Fine structure	76
4.4.1 Fine structure I: initial spasm	77
4.4.2 Fine structure II: small oscillations	78
4.4.3 Fine structure III: steps	80
4.5 Problems repeating measurements	85

5. Next steps	88
5.1 Next generation SCPFM	88
5.1.1 Polymer NEMS with off-chip multiplexing	88
5.1.2 LETI silicon NEMS with on-chip multiplexing	89
5.2 First experiments	90
5.2.1 Pharmacological perturbations: building a library of molecular-mechanical force signatures of basic cytoskeleton reactions, or fishing with drugs	90
5.2.1.1 Actin-myosin	91
5.2.1.2 Microtubules	92
5.2.1.3 ECM and integrins	93
5.2.1.4 Upstream regulation	94
5.2.2 Mechanical perturbations: molecular mechanisms of mechanotransduction	95
5.2.2.1 Mechanical stimulation	96
5.2.2.2 Mechanotransduction and response	99
5.3 Long term vision	101
5.3.1 High-density, high-throughput pharmaceutical screening	102
Appendix 1: Beam deflection derivation	104
Appendix 2: All-polymer process fabrication details	106
Appendix 3: Silicon nitride membrane fabrication process details	112
Appendix 4: Microfluidics fabrication process molds	119
Appendix 5: Microfluidics fabrication process soft-lithography	122
Appendix 6: Additional dynamics data	123
References	125

List of Figures

Figure 1. Measurement Space	12
Figure 2. Beam Deflection Diagram	16
Figure 3. Beam Geometry Diagram	17
Figure 4. Force Resolution vs Time Resolution I	24
Figure 5. Force Resolution vs Beam Width and Beam Thickness	25
Figure 6. Force Resolution vs PZR Offset and PZR Width	26
Figure 7. Force Resolution vs PZR Thickness	27
Figure 8. Force Resolution vs Time II	27
Figure 9. Non-Linear Effects on the Transducer Responsivity	28
Figure 10. Measurement Space with SCPFM	30
Figure 11. All-Polymer Fabrication Process	38
Figure 12. Stress and Cracking in Polymer Chips	39
Figure 13. Completed All-Polymer Chips	39
Figure 14. Cell Culture in All-Polymer Chips	40
Figure 15. Hybrid Etch Before and After	43
Figure 16. Hydrofluoric Acid Etch Reactions	44
Figure 17. Silicon Nitride Fabrication Process	45
Figure 18. Microfluidics Encapsulated NEMS Chips	47
Figure 19. Finished Force Sensors	48
Figure 20. Pad Size and Bridge Curling	49
Figure 21. Force Sensor Calibration	50
Figure 22. Microfluidics Schematic	53
Figure 23. Surface Chemistry in Petri Dish	58
Figure 24. Pad Size and Cell Spreading	59
Figure 25. Surface Chemistry in Microfluidics	60

Figure 26. Electrocleaning and Surface Chemistry in Microfluidics	62
Figure 27. Microscope Mounted Incubator and Sample Holder	64
Figure 28. Proof of Principle Data	73
Figure 29. The Chen Group's mPADS	76
Figure 30. Fine Structure I: Initial Spasm	77
Figure 31. Fine Structure II: Small Oscillations	80
Figure 32. Fine Structure III: Steps	81
Figure 33. Back Steps	82
Figure 34. Anatomy of Step	83
Figure 35. Statistical and Dynamic Data	83
Figure 36. Additional Dynamics Data	123
Figure 37. Step Flat and Transition Data	124

List of Tables

Table 1. Lock-in amplifier: equivalent noise bandwidth and time resolution	21
Table 2. Lock-in amplifier: equivalent noise bandwidth, time constant and filter	22
Table 3. Pre-Amplifier comparison	23
Table 4. Polymer comparison	35
Table 5. Surface-Volume ratio comparison	41
Table 6. Fluid flow numbers	55
Table 7. Surface chemistry contact angle	60
Table 8. Durotaxis parameters	99

Nomenclature I: Symbols

a – material dependent hooge parameter

Δ -- displacement

E – Young’s modulus

ε – strain

e_i – amplifier voltage noise

F – force

f – frequency

ζ – thickness of piezoresistive wire

G – tension force

I – moment of inertia

i_i – amplifier current noise

K – spring constant

k_B – Boltzmann’s constant

κ – transducer responsivity

l – substrate length

L – length of beam

λ – filter setting

N – number of carriers

n – carrier density

π_l – longitudinal piezoresistance coefficient

R – resistance

δR – change in resistance

$r(x)$ – radius of curvature

\vec{r} – cartesian vector

p – force contraction dipole

$\vec{\rho}$ – cartesian vector

ρ – resistivity

S_{Th} – thermal noise voltage spectral density

S_H – hooge noise voltage spectral density

σ_0 – surface stress distribution

T – substrate thickness

t – thickness of beam

τ – time constant

u – distance between piezoresistive wire and edge of beam (pzt “offset”)

u_{ij} – strain tensor

ν – poisson ratio

V – voltage

V_0 – input voltage

δV – voltage signal

v – width of piezoresistive wire

w – width of beam

ΔW – work

x – x-coordinate

y – y-coordinate

$\Delta X(r)$ – displacement of surface at r in x direction

$\Delta Y(x)$ – displacement of centerline of beam in y direction

δz – vertical displacement

Nomenclature II: Abbreviations

AC – Alternation Current

AFM – Atomic Force Microscopy

BJT – Bipolar Junction Transistor

CB – Cytochalasin B

CCD – Charge-Coupled Device

CD – Cytochalasin D

CFDRC -- CFD Research Corporation

CIPC – Isopropyl N-3-chlorophenyl carbamate

CMOS – Complimentary Metal-Oxise-Semiconductor

CPD – Critical Point Drier

DIC – Differential Interference Contrast

DMEM – Dulbecco's Modified Eagle Media

DNA – DeoxyriboNucleic Acid

ECM – Extra-Cellular Matrix

ECR – Electron Cyclotron Resonance

ESEM – Environmental Scanning Electron Microscope

FDA – Food and Drug Administration

FN – Fibronectin

GFP – Green Fluorescent Protein

GUI – Graphical User Interface

HEPES – 4-(2-HydroxyEthyl)-1-PiperazineEthaneSulfonic acid

HCS – High Content Screening

HF – Hydrofluoric Acid

HTS – High Throughput Screening

JFET – Junction Field-Effect-Transistor

KOH – Potassium Hydroxide

LPCVD – Low Pressure Chemical Vapor Deposition

MEMS – Micro ElectroMechanical System

mPADs – microfabricated Post Array Detectors

MPTS -- Mercapto-Propyl-Trimethoxy-Silane

NEMS – Nano ElectroMechanical System

PBS – Phosphate Buffer Solution

PDMS – Poly-DiMethyl-Siloxane

PEG – PolyEthylene-Glycol

PMMA – Poly(Methyl MethAcrylate)

PZR – PieZoResistor

RGD – Arginine-Glycine-Aspartic Acid

RIE – Reactive Ion Etch

SAM – Self-Assembled Monolayer

SCPFM – Single Cell Pico Force Microscopy

SiN – Silicon Nitride

SOI – Silicon On Insulator

SURF – Summer Undergraduate Research Fellowship

TIRF – Total Internal ReFlection

TFM – Traction Force Microscopy

UV – Ultra Violet

Chapter 1. Introduction

The goal of my research is to build new tools for studying biology using nano-electromechanical-systems (NEMS). Specifically, I have developed a tool for measuring the force exerted by an individual lamellipodia from an adherent cell, which I call Single-Cell-Pico-Force-Microscopy (SCPFM). SCPFM is built around a NEMS force sensor and includes a large suite of supporting technology that I have developed and integrated into a complete system. Before I get into the details of SCPFM, I will use this introduction to discuss the principles that have guided me in this research in an effort to clarify the advantages and disadvantages of NEMS tools as well as to explain the specific path that I have taken in my research.

The basic idea behind building NEMS based tools for biology is that NEMS are able to interact mechanically with biological systems and transduce that mechanical interaction into an electronic signal. This is a significant departure from the traditional optical tools, specifically optical microscopy, which dominate the biological sciences [1]. Even in the subfield of cellular mechanotransduction, all existing tools, such as microfabricated post array detectors (mPADS) [2], traction force microscopy (TFM) [3, 4], atomic force microscopy (AFM) [5] and the variety of optical bead implementations [6, 7], use optical readout. There are a few tools in biology which readout electronic signals, such as patch clamps [8, 9] and neuronal electrophysiology [10, 11]. These tools work well for studying the electronic characteristics of cells (ion gradients, action potentials, etc.) but they are not useful for studying cellular mechanics. The combination of mechanical interaction and electronic signal sets NEMS tools apart.

It is the area of signal readout – optical vs electrical – that sets fundamental limits on tool performance. Optical measurements are massively parallel spatial measurements with fundamental limits in spatial resolution imposed by the diffraction limits of light and fundamental limits in sensitivity imposed by CCD dark current [12]. In contrast, the electronic readout of NEMS is inherently serial and the

fundamental limits of the sensitivity are imposed by the thermal motions of either the biological system under study [13, 14] or the measurement electronics [15, 16], depending on the system. A well designed NEMS transducer and electronics can achieve significant improvements in sensitivity over optical systems [17]. These differences are rooted in the particle nature of photons and electrons, which are bosons and fermions respectively. This is an important point: NEMS tools will not achieve the parallel data gathering ability of optical microscopy; they do, however, offer significant advantages with respect to the sensitivity that can be achieved.

There are a few techniques which manage to circumvent these limitations. Far-field optical nanoscopy is a collection of fluorescence imaging techniques that can achieve nanometer resolution [18] and recent demonstrations of materials with negative diffraction in the visible spectrum offer hope of optical nanoscopy without fluorescence [19]. Within bio-mechanics optical bead and AFM measurements are able to measure forces at high resolution using optical readout. However, each of these techniques actually extracts data serially: optical beads through the single bead, AFM through the single tip and optical nano-scopy by toggling fluorescent molecules between excited and quenched states using two excitation lasers in a scanning pattern. Thus, these techniques follow the same pattern of tradeoffs that I have outlined in the previous paragraph. Additionally, optical beads and AFM have drawbacks that NEMS devices can address: the forces that optical beads can measure or apply are limited by the laser trap strength ($\sim 500\text{pN}$) and thus have very poor dynamic range [6]. AFM's are limited in their geometrical configuration which limits their ability to interact with the cell in a physiologically relevant manner [5]; furthermore, they cannot be integrated with complex microfluidics [20].

The serial nature of NEMS measurements restricts studies to individual cells or even parts of an individual cell such as a single lamellipodium. This is obviously necessary to observe subtle phenomena which would otherwise be averaged out over many cells. Looking at cells one at a time rather than averages over large numbers of cells also enables the observation of heterogeneity within cell

populations including outlier behavior that occurs at low probability [21]. This is important because individual cells play a significant role in important areas of biology such as development [22] and cancer [23]. The role of noise and stochastic processes in cell behavior also highlights the existence and importance of outlier cells [24, 25].

There is a flip side to this situation; one can be easily misled by inappropriately generalizing the behavior of an outlier cell to that of the majority. The obvious solution to this problem is to make many measurements on many cells. This places certain requirements on the NEMS tool: to provide biological information measurements must be easily repeatable. This is a significant shift from the typical device physics research paradigm; a large amount of engineering must be done upfront to refine the ease of use of the tool before the principle science – the biology – can be tackled.

One good way to address these issues is to leverage the scalability of micro and nanofabrication techniques to build so many NEMS devices that they are disposable and measurements are not limited by devices quantity. This can be done at a variety of scales: many NEMS devices within an area smaller than a cell, many NEMS devices on a single chip and many chips on a single wafer. I use the latter two techniques aggressively in this work. This is not, however, the same as achieving the parallel nature of optical measurements. Each NEMS device must be contacted and measured individually, which scales measurement complexity and the fanout problem linearly with the number of devices. Multiplexing techniques can reduce the proliferation of measurement electronics and aid the fanout problem, but only at the expense of time resolution which will also degrade linearly with the number of multiplexed devices. This is not to say that these techniques aren't useful, only that there are tradeoffs and they are not infinitely scalable.

NEMS based tools for biology rely on a range of technologies, many of which have been developed or matured only within the past 5-10 years. Micro and nanofabrication – using photo and electron beam

lithography to fabricate structures with micron and nanometer dimensions – is obviously critical [26]. The development of wafer-scale electron beam lithography is particularly important to making NEMS devices in disposable quantities. Micro ElectroMechanical Systems (MEMS) and NEMS structures are an extension of micro and nanofabrication that couple electrical and mechanical characteristics (*i.e.*, computers chips with moving parts). MEMS and NEMS devices were originally developed for operation in vacuum [17] and have only recently moved to operation in air and water [27, 28]. Key to this advance has been the development of new transduction methods such as the piezoresistive effect used in this research [27, 29]. However, I believe the most important technological advance has been large scale integrated microfluidics [30-33], without which wetting NEMS devices in a controlled manner would be impossible. Microfluidics enable a number of critical technologies for integrating NEMS with biology: control of fluid mechanics, separation of fluids and electronics, precise control of chemical and biological reagents, and the reduction of chamber volumes to the nano-liter level necessary to deliver cells and reagents to electronically addressed devices in a timely manner.

As I said before, the goal of my research is to develop tools. To be useful these tools must be robust and user-friendly. The chips, NEMS and microfluidics, must be disposable. Inspired by our efforts to fund and build workstations for our collaborators, I have set as a goal that the interface will be sufficiently user friendly that a biology graduate student could use the tool, including setup and take down, after 1-2 weeks of training. These problems are principally ones of engineering. I have had to develop new fabrication technologies and novel devices for this project, but most of my effort has gone toward refining the fabrication process to enable production on a sufficient scale for the devices to be abundant and disposable. A great deal of effort has also gone into integrating the various disparate technologies involved: the NEMS, microfluidics, surface chemistry, electronic measurement, cell culture, fluorescent microscopy and computer control. So much effort devoted to engineering and refining a tool without basic proof of principle data is effectively putting the cart in front of the horse, but I believe that has been necessary and I now have the proof of principle data to justify this approach.

In summary, these are the principles that have guided my research: fabrication and microfluidics technologies have developed sufficiently in the past decade that NEMS based tools for the biological sciences are achievable. NEMS devices can deliver significant advantages in measurement sensitivity but not in parallel data gathering. In order to deliver biological information, measurements must be easily repeatable. In order for measurements to be easily repeatable, the NEMS devices and microfluidics must be abundant enough to be disposable, experimental routines such as surface chemistries and tissue culture must be routine, and the system must be automated, bug free and with a user-friendly interface.

In this thesis, I will discuss what I have done to achieve some of these goals and the hurdles that remain in the areas where I have not yet met these goals. In Chapter 2 I will discuss the relevant biology: what we know about how and why cells exert forces on their surroundings and I will review the existing tools used in this field. In Chapter 3 I will describe the technology which I have developed, Single-Cell-Pico-Force-Microscopy, in detail. I have succeeded in demonstrating the principle and potential of SCPFM by measuring the force relaxation and contraction while the force generating ability of a single fibroblast is repeatedly disrupted with Cytochalasin D and allowed to recover in growth media. I will present and discuss this data in Chapter 4. Finally, I will discuss the next steps in device development, biology experiments and the long term vision for SCPFM as a tool for pharmaceutical screening, particularly for cancer therapeutics, in Chapter 5.

Chapter 2. Cell forces and mechanotransduction

2.1 Why cells exert forces

Nearly all eukaryotic cells exert forces on their surroundings. By pulling on their surroundings, cells are able to generate and maintain tension within their cytoskeleton which is critical for normal cell function. Tension enables cells to control their shape, respond quickly and globally to mechanical changes in their surroundings, and likely plays an important role in the way cells place and organize the organelles within their interior [34-36]. In addition to creating a basal level of tension for normal operation, cells exert forces on their surroundings in order to move around (motility) and in order to learn about their surroundings and orient themselves in three-dimensional space, a process called mechanotransduction by the *in vitro* biologists [37, 38] and mechanoreciprocity by the medical field [39-42].

Motility is the process whereby cells move themselves in space. There are a variety of methods eukaryotic cells use to travel; for instance, sperm cells use large flagella (tails) to swim and keratocytes, which form skin and heal wounds in amphibians and fish, travel by constantly extending lamellipodia and skip the contraction step, thus rolling like a tank tread [43, 44]. However, most eukaryotic cells use the fibroblast phenotype to travel: they send forward extensions, lamellipodia on flat, *in vitro* surfaces and narrower filopodia when in three-dimensional tissues, which anchor to the extra cellular matrix (ECM) and pull the cell forward using the same molecular machinery used to generate basal tension within cells. Many cells are motile in the early phases of development, typically with a fibroblast phenotype, as they move to various places in the developing organism. Neurons are also very motile during development; they send out growth cones to seek out other neurons and form synapses. Immune system cells such as neutrophils are motile throughout an organism's life; they travel using the fibroblast phenotype, typically following chemotactic gradients, in search of infections to be attacked [43].

Mechanotransduction plays a major role in tissue formation and stem cell differentiation. Experiments demonstrate that substrate compliance plays a significant role in stem cell differentiation: cells on stiff substrates differentiate toward bone cells whereas cells on soft substrates differentiate toward nerve cells [45]. Fibroblast motility has been shown to depend on substrate compliance, an effect termed durotaxis [46]. ECM compliance sensing has further been shown to play a significant role in regulating tissue development [47] and basic models have been proposed [48]. In each of these instances, cells take mechanical cues from their surroundings, process the information and respond accordingly.

The details of how cells probe, process and respond to mechanical stimuli are not well understood, but there is agreement on the basic process. Cells reach out to the ECM with a lamellipodia or filopodia, form a weak connection to the ECM through transmembrane proteins, such as integrins or cadherins, and apply force through that connection using contractile actin-myosin stress fibers that connect to the transmembrane proteins through molecular bundles called focal contacts. The compliance of the cell's surroundings determines how that force is distributed. A compliant ECM will deflect, thus relieving the force across the focal contact and transmembrane proteins, whereas a stiff ECM will not deflect, thus passing the force to the molecules in the focal contact and the transmembrane proteins which may cause one or more of these molecules to undergo a conformation change that opens new binding sites which leads to transformation of the focal contact to a focal adhesion and an upregulation of force. Thus the force sensing molecules in the focal adhesion act as a molecular-mechanical switches. Various models exist and various molecules have been identified as potential molecular switches [38, 49-52]. The opposite can occur too: neurons prefer to pull on soft substrates and will abandon contacts on hard substrates; models exist for this situation as well [53]. But the principle is the same: the ECM compliance dictates the cell's response to an applied force through molecular-mechanical events.

The cytoskeleton is not simply an organ within a cell to create shape and regulate mechanical properties. The cytoskeleton is extensively coupled, mechanically and chemically, to all organelles within a cell and

many, if not all, signaling networks within a cell [54]. The state and behavior of the cytoskeleton is fundamental to nearly all aspects of cell behavior and health. Illustrating this point are a number of diseases that have roots in mechanical malfunctions of cells. Ingber has written a nice review article in which he highlights 63 diseases that fall into a range of seemingly unrelated areas of medicine from orthopedics to cardiology to neurology. Yet the diseases all have their origins in changes in cell mechanics, tissue structure or molecular-mechanical energy conversion within the cells [55]. Ingber's article powerfully illustrates the fundamental nature of cell mechanics as the basis for a range of disparate diseases.

Cancer provides a number of poignant examples of phenotype changes that couple to cell mechanics. AFM measurements indicate that cancer cells are more compliant than healthy cells [5]. Metastasis requires a dramatic change in cytoskeleton regulation from stationary cells to highly motile cells which can then spread the cancer throughout the patient [56]. In another example, glioblastoma multiforme metastasis appears to be directed and activated by the mechanics of tissue boundaries [57]. Cell division, which when uncontrolled is another hallmark of cancer, is heavily dependent upon cytoskeleton mechanics [58]. Accordingly, numerous successful cancer chemotherapeutics, such as Taxol and the Vinca alkaloids, work by subtly disrupting microtubule dynamics thereby preventing cell division which disproportionately attacks cancer cells. These are dramatic phenomena that do not require high resolution mechanical measurements to observe, but they are indicative of the potential of using mechanical measurements, not only for fundamental biology, but also to study and develop treatments for specific pathologies.

2.2 How cells exert forces

The cytoskeleton is comprised of three distinct molecular structures: actin mesh and stress fibers, microtubules made of tubulin, and intermediate filaments. Each of these structures are made from small

monomer units that are assembled into complex and dynamic structures. Cells utilize equilibrium dynamics and a large variety of cytoskeleton binding molecules to control the formation and rearrangement of these cytoskeleton structures. Intermediate filaments give the central body area of the cell its characteristic stiffness and play an organizing role in the placement of organelles within the cell. In general, intermediate filaments are thought to be rather static and thus are not often studied. Microtubules are long filaments made from tubulin monomers that radiate outward from a central microtubule organizing center. Microtubules play a major organizing role during cell division and are believed to coordinate motility and cell shape by stabilizing and destabilizing focal adhesions [43, 59, 60].

Actin can form a surprising range of different structures within a cell. Actin monomers form directional filaments, with an assembling end and a disassembling end, each with its own rate constant for assembly and disassembly. Furthermore, actin binds a GTP molecule which affects actin's binding properties; as a result each actin monomer has four different binding and unbinding rate constants [61-63]. The range of binding constants as well as various actin binding molecules such as the molecular motor myosin and ARP 2/3, which binds actin filaments in a branching formation, enables a cell to create a wide range of structures and functions with actin. Two of the most common are treadmilling actin meshes which typically are formed at the edge of a cell, where it is referred to as cortical actin, and stress fibers which are bundles of long actin filaments that are cross-linked by bundles of myosin motors. The myosin motor bundles pull adjacent actin filaments in opposite directions, thus generating large contractile forces using the same basic machinery as muscles. Stress fibers are the source of the contractile forces which cells use to generate tension, pull themselves forward and probe the compliance of their surroundings [43].

Stress fibers terminate in focal adhesions which are complex plaques of molecules that connect stress fibers to transmembrane proteins such as integrins and cadherins [50, 64-66]. Focal adhesions play a central role in regulating cell force and are believed to be the site of the molecular switching events

central to mechanotransduction [38, 49, 52]. Focal adhesions start as very small connections called focal contacts that will grow into large, high force connections on stiff substrates but are typically abandoned on soft substrates [49, 64]. Significant work has been done to identify and understand the numerous components of focal adhesions, including the identification of potential molecular switches that can exist in two distinct conformations including integrins [67-69], vinculin [70-72], talin [73], pp60src [74] and fibronectin [49, 75-78].

2.3 By the numbers

In order to study a process like mechanotransduction, we need a tool that can observe the molecular level switching or force sensing events that are believed to trigger a decision by a cell as well as the ultimate response or rearrangement that occurs on the whole cell level [79]. Whole cell events, such as lamellipodia contraction and motility, generate 10's of nanoNewtons of force at individual focal adhesions and take from 10 minutes up to a couple of hours to evolve [2, 3].

At the small end of the spectrum, there are many different molecular events that manifest force responses within cells. Actin polymerization is the driving force behind lamellipodia extension and is proposed as a force sensing mechanism in neural growth cone extension. Actin polymerization stall forces have been measured by the Theriot group using optical beads to be 0.1-1pN [80]. Microtubule polymerization also generates forces, measured at ~ 2.8 pN [81], and is known to play a major role in cell division. Myosin V is the principle generator of contractile force in cells and has been well studied at the single molecule level with optical beads. Single myosin steps move 30-38nm and can generate forces of 6-8pN in a single step [82]. The small focal adhesion proteins vinculin [70-72], talin [73], and pp60src [74] have been suggested as candidate molecular switches in focal adhesions, but the force dynamics of these molecules have not been studied. Force induced unfolding events in integrins and fibronectin have been studied with AFM by the Vogel group and require forces in the 10-40pN range to induce unfolding

events [77, 83, 84]. It is difficult to estimate the time resolution needed to observe these events in a living cell from optical bead and AFM experiments; however, ~ 1 ms is the conventional assumption made within the field [79].

Two groups have used optical bead measurements to observe single molecule events in cells. The Rohrbach group was able to measure filopodia contraction and found single steps, most likely from individual myosin V molecules, with force dependent step size – larger counter forces resulted in smaller step sizes – that ultimately stalled above 19 pN [7]. The steps occur on a roughly 100ms time scale. The Sheetz group has successfully anchored optical beads to focal contacts on the top of spread cells and pulled on the beads. They observe a succession of 2pN “slip bonds” at a load dependent time scale of seconds [6].

2.4 Existing technologies for measuring cell forces

There are a number of optical techniques that are used to measure forces from adherent cells at the single cell level. Some are good for measuring whole cell forces and some for measuring single molecule level forces, but none have the dynamic range necessary to span both regimes; see Figure 1 [85, 86]. Traction force microscopy and mPADs are both good ways for measuring whole cell forces: they have force resolution of ~ 1 nN and time resolution of 10's of seconds, but they can measure forces in excess of 100nNs and can be monitored for hours. mPADs, developed by the Chen group, is the simpler of the two methods: posts are fabricated from PDMS, cells are allowed to spread on the posts and the cells deflect the posts, which operate as simple Hookian springs, when they contract [2]. The deflections are measured using an optical microscope. The downside of mPADs is that the cells are spread on a discontinuous surface and it is not clear how this will affect the cell's behavior. The Chen group has recently succeeded in putting magnets inside some of the posts and using them to apply forces to a cell

[87]. Active mechanical perturbation of cells is a particularly interesting and presently underserved area of research.

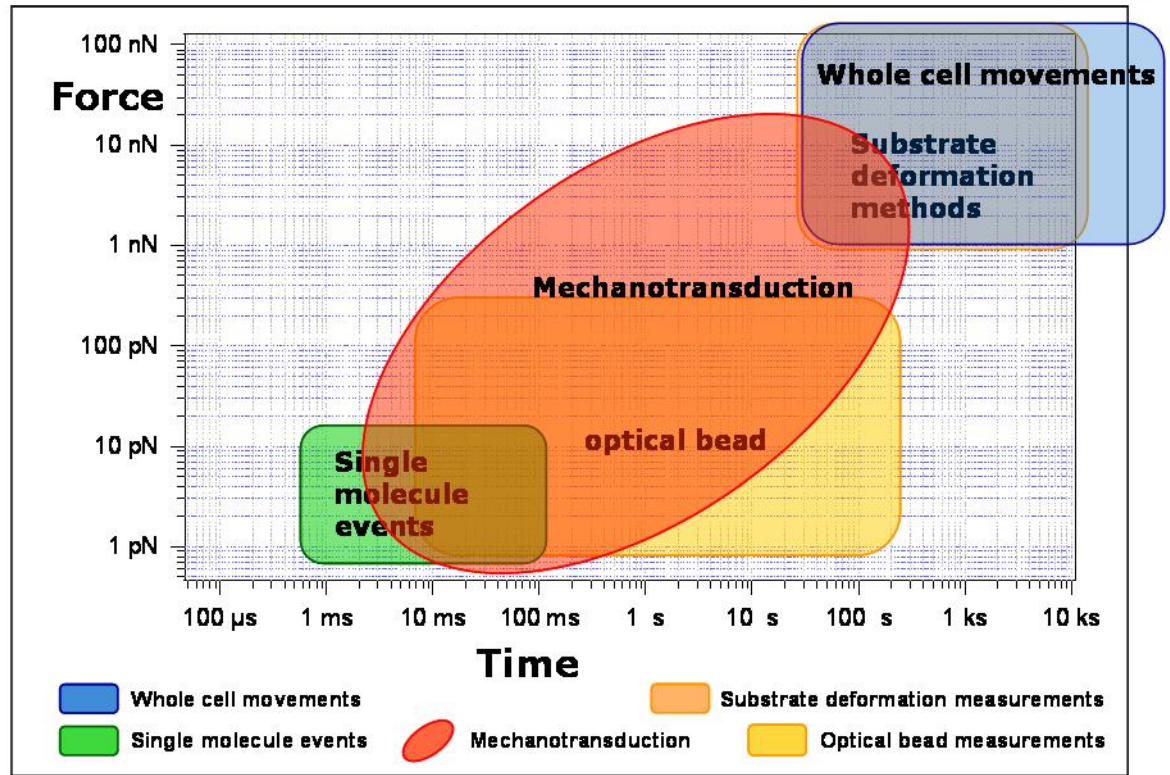


Figure 1. The measurement range in force and time of substrate deformation methods, such as mPADs and TFM, and optical bead measurements is plotted with the ranges in which single molecule events, whole cell movements and mechanotransduction occur.

Traction force microscopy was developed by Wang and Dembo in the late 90's. A polyacrilamide gel is formed with a random pattern of small (typically 40nm) fluorescent beads close to the gel's surface; when cells spread, contract and travel along the surface, the beads move and those movements are measured with a fluorescent microscope [3, 4]. The upside of TFM is that the cells are spread on a flat and continuous surface, and fabricating the substrates does not require photo lithography to make the original mold (a significant hurdle for most biology groups). The downside of TFM has been the computation required to extract force data from the measured deflection data, because the substrate is a continuous half plane and every point is coupled to every other point. The problem is ill posed and cannot be solved exactly. Until recently, the only algorithm written to analyze TFM image data was a maximum likely

hood based algorithm written by Dembo that required extensive computation time – days to resolve a single frame of data – and was not widely distributed by Dembo, thus severely limiting TFM use. However, quite recently the Waterman group has revamped TFM by introducing a two color bead system, developing a set of algorithms that run much faster than Dembo's and when used together give improved spatial resolution, $\sim 1\mu\text{m}$ with force resolution of roughly 1nN [88]. With these advances, TFM is starting to gain more widespread use.

At the other end of the spectrum, optical beads can measure events with the sub-picoNewton and millisecond resolution needed to observe single molecule events. However, the upper limits of optical beads are limited to 100's of picoNewtons by the trap strength and 10's-100's of seconds by drifts [89]. Optical beads are also difficult to couple to cells in physiologically relevant ways [6, 7].

Atomic Force Microscopy has been used recently to measure the compliance of spread cells, adding quantitative analysis to the stiffness increase seen in tumor cells and perhaps opening an avenue to investigate intermediate filaments [5, 90]. These days one can purchase an AFM that is setup to monitor living adherent cells, so it is reasonably easy to probe the compliance of a cell's body. However, setting up an AFM to measure the adherent forces generated by a cell has not been done and I am not optimistic for the prospects of it happening.

Due in part to the fact that none of these force measurement techniques have the resolution and dynamic range to measure from single molecule up to whole cell events, much of the work done to elucidate cell mechanics, motility and mechanotransduction has actually been done with optical techniques that track cells and molecules in time but are unable to measure force. The Sheetz group has done most of their work with Differential Interference Contrast (DIC) and Total Internal Refraction (TIRF) microscopy [52, 91, 92]. The Geiger group has an impressive library of fluorescently labeled focal adhesion and cytoskeleton proteins which they transfect into live cells and image with Confocal microscopy as

adhesion evolve in real time [93, 94]. The Waterman group has developed and continued to advance fluorescent speckle microscopy which adds a computational analysis to Confocal fluorescence microscopy that is able to track individual clusters of fluorescent proteins based upon the unique, random clustering – the speckle – of the fluorophores [95-98]. These microscopy techniques enable researchers to connect single and macro molecular dynamics with whole cell behaviors, but are unable to measure force. High resolution force-time records of ECM compliance sensing and response events will provide useful information; for instance, the magnitude of the forces needed to drive a decision event will indicate the rough number of molecular switches involved or the rate of force generation will yield information about how forces are regulated.

Chapter 3. The Tool: Single-Cell-Pico-Force-Microscopy

3.1 Goal

There is room in the mechanotransduction field for a NEMS based force sensor to make a significant contribution. The principle advantage of such a tool will be force measurement resolution and dynamic range. Specifically, the tool needs force resolution (ideally) in the single molecule range ($<10\text{pN}$) and at least in the macro-molecular range ($<100\text{pN}$), and needs to have five decades of dynamic range so that it can measure into the 100's of nN in order to observe whole cell processes. Of course, molecular level force resolution is meaningless without molecular level time resolution (1-10ms) and similarly for the dynamic range, five decades of time dynamic range are necessary to continuously observe molecular events in a cell for hours. Optical microscopy, preferably both fluorescence and a contrast enhancing technique such as phase optics, is necessary for confirming cell placement vis-à-vis the force sensor and cell viability at a minimum. Confocal fluorescence would enable tracking of molecular events. Microfluidic encapsulation is also necessary for a range of reasons from separating the electronics from the fluidics to delivering cells directly to the specific device. Microfluidic encapsulation further enables precision fluidic control and thus precision pharmacological perturbation of the cell being studied. It must be routine to culture cells within the tool, specifically on the force sensor – studying dead and dying cells is of limited utility. The entire system must be automated and user friendly. And lastly, the devices must be abundant and disposable. These are the specific goals for which I have designed Single-Cell-Pico-Force-Microscopy (SCPFM) to address.

I have developed SCPFM, a tool that meets nearly all of these requirements by utilizing novel polymer NEMS force sensors [99]. SCPFM is a fully integrated, monolithic instrument that combines the near-single molecule force measurement capabilities of NEMS based force sensors with integrated microfluidics that enable precision fluid control, and thereby precision pharmacological stimulation of

individual cells. SCPFM enables the systematic study of the molecular-mechanical responses of individual cells to pharmacological and mechanical stimulation.

3.2 The NEMS force sensor

The NEMS force sensor is a doubly clamped beam with an integrated piezoresistive (strain coupled) force sensor [27]. The sensor, which is positioned adjacent to a bridge that localizes an adherent cell, includes a fibronectin coated attachment point for a cell lamellipodium. Upon attachment an adherent cell contracts and exerts force upon the sensor, shown in Figure 2. The NEMS devices are fabricated from polymer instead of traditional MEMS materials, such as silicon-on-insulator (SOI), principally because polymer's low Young's modulus enables improved sensitivity and the fabrication of devices that are compliance matched to typical biological materials. Additionally, the material costs for the polymers are significantly less than traditional semiconductor materials such as SOI.

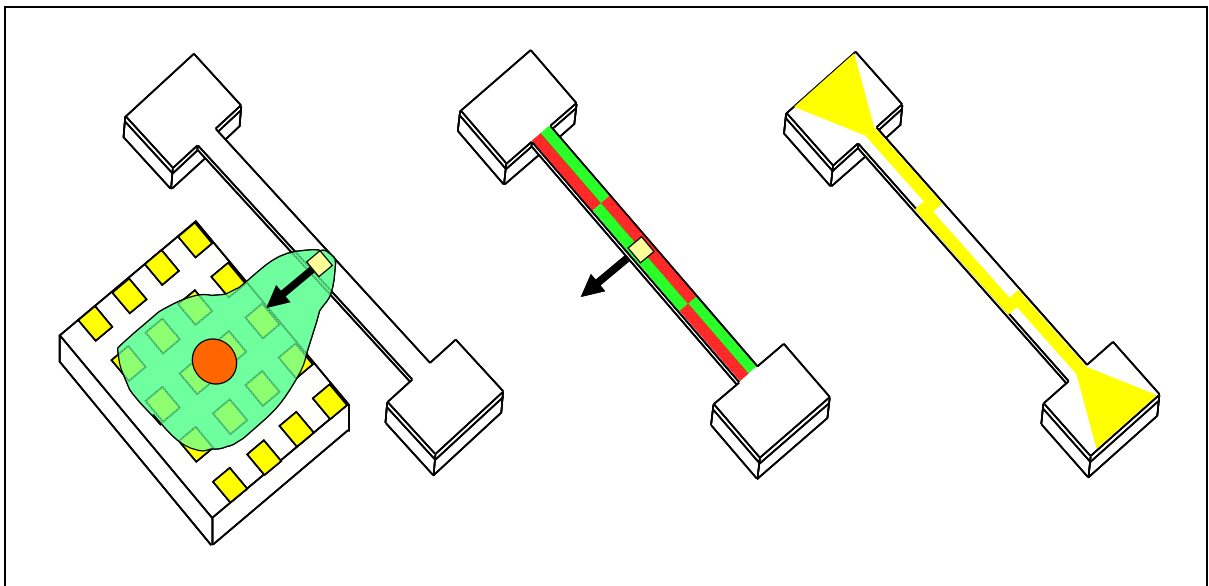


Figure 2. At left an adherent cell is spread adjacent to a force sensing beam, a lamellipodium from the cell attaches to fibronectin coated pad on the beam (in yellow) and contracts, deflecting the beam toward the cell (black arrow). The deflection induces strains in the beam shown at center: the green regions are under tensile stress and the red regions compressive. The piezoresistive force sensor is patterned across the beam in a zig-zag pattern so as to couple to the tensile strains only, shown at right.

3.2.1 The spring constant

The force sensor is a doubly clamped beam with a piezoresistor patterned in a zig-zag shape that breaks the symmetry in the plane of the beam, thus coupling the force sensor to displacements in the plane. I estimate the spring constant of the beam as follows: the displacement of the center line of a doubly clamped beam due to a force exerted at the beam's mid point is given by (see Appendix 1 for derivation)

$$\Delta Y(x) = F \frac{x^2(3L - 4x)}{4Et w^3}, \quad (1)$$

where x extends from zero to $L/2$, t , w , and L are the thickness, width and length of the beam as shown below (Figure 3), E is the young's modulus and F is the applied force [100].

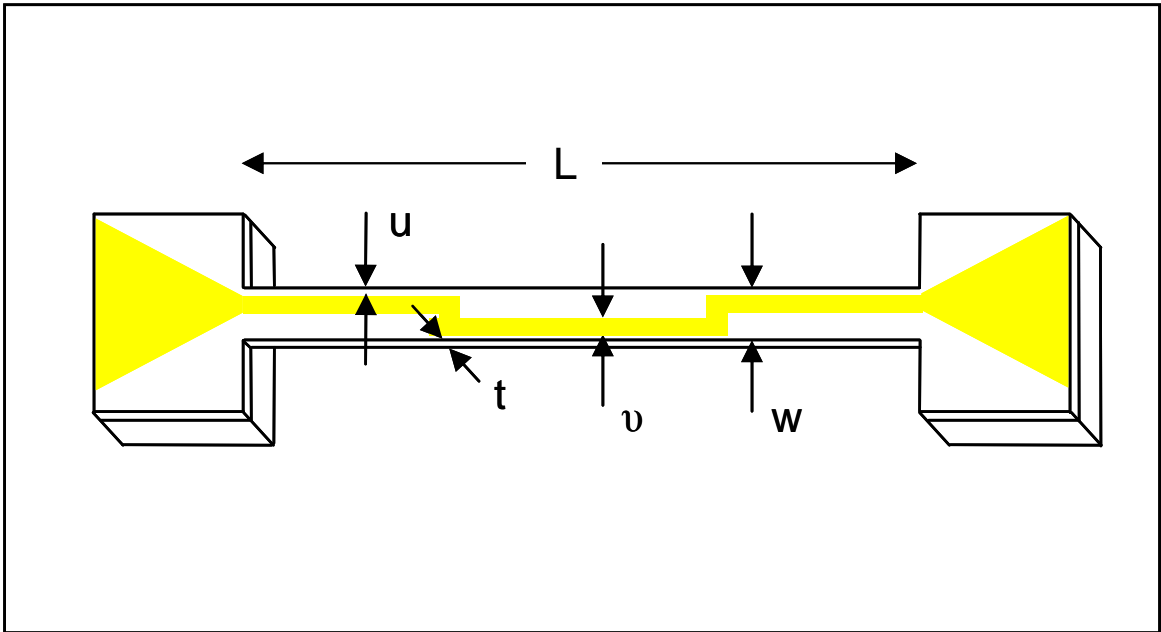


Figure 3. Diagram of force sensing beam with zig-zag patterned piezoresistor for coupling to in-plane strains. L is the length of the beam, w , the width and t is the thickness. v is the width of the piezoresistor and u is the offset between the edge of the piezoresistor and the edge of the beam.

I define the effective spring constant, K , by the displacement at the midpoint, $x=L/2$:

$$K = \frac{F}{\Delta Y(x = L/2)} = \frac{16Et w^3}{L^3}. \quad (2)$$

3.2.2 Strain in the piezoresistor

A strain gauge is integrated into the beam by patterning a zig-zag piezoresistor of width ν and thickness ζ symmetrically across the four quarters of the beam, shown in yellow in Figure 3. The zig-zag pattern will maximize the strain induced by the displacement described in equation (1). The strain in an infinitesimal element of the PZR conductor at x,y is given by [100]:

$$\varepsilon = \frac{y}{r(x)}, \quad (3)$$

where y is the displacement in the y direction from the center line of the beam and r is the radius of curvature of the center line at that point. I approximate the radius of curvature:

$$\frac{1}{r(x)} = \frac{d^2}{dx^2} \Delta Y(x) = F \frac{6L - 24x}{4Et w^3}. \quad (4)$$

Each quarter of the piezoresistor will be symmetric with strain, thus I need only integrate over one quarter of the wire to determine the average strain:

$$\bar{\varepsilon} = \frac{1}{area} \int \frac{y}{r(x)} d(area) = \frac{F}{(\nu)(L/4)} \int_{w/2-u-\nu}^{w/2-u} \int_0^{L/4} \frac{y(6L - 24x)}{4Et w^3} dx dy, \quad (5)$$

where u is the offset between the edge of the piezoresistor and the edge of the beam, as shown in Figure

3. Equation (5) is easily integrated:

$$\bar{\varepsilon} = \frac{3 F L (w - 2u - \nu)}{8 E t w^3}. \quad (6)$$

3.2.3 The Wheatstone bridge and the transducer responsivity

The strain gauge uses the piezoresistive effect [29] to convert the induced strain, equation (6), into a change in resistance:

$$\frac{\delta R}{R} = \pi_l \varepsilon = \frac{3 \pi_l}{8 E} \frac{L(w-2u-\nu)}{tw^3} F, \quad (7)$$

where π_l is the longitudinal piezoresistance coefficient for the wire. For the silicon used to fabricate Jessica Arlett's BioNEMs cantilevers, a piezoresistance coefficient of 40 is expected and Jessica measured roughly 47 for the transducer responsivity with the AFM [101]. For gold, geometric considerations predict a piezoresistance coefficient of 2 for bulk metals [29], but Thaysen *et al.* [102] report a value of roughly 4; the discrepancy is possibly due to thin film effects. In the calculations that follow, I assume the conservative value of 2 for the longitudinal piezoresistance coefficient of gold, which is supported by AFM tests.

The force sensing beam will be integrated into an on chip Wheatstone bridge [103-105] with one suspended reference beam and two supported balance resistors. When optimally balanced the Wheatstone bridge converts a change in resistance into a voltage signal according to

$$\delta V = V_0 \frac{1}{4} \frac{\delta R}{R}, \quad (8)$$

where V_0 is the voltage applied to the bridge. Combining equations (7) and (8) we obtain the proportionality constant between the applied force and the measured voltage signal: the transducer responsivity, κ , of the force sensing beam:

$$\delta V = \frac{3 \pi_l}{32 E} \frac{L(w-2u-\nu)}{tw^3} V_0 F = \kappa F, \quad (9)$$

$$\kappa = \frac{3 \pi_l}{32 E} \frac{L(w-2u-\nu)}{tw^3} V_0. \quad (10)$$

3.2.4 Noise I: piezoresistor noise

The voltage signal given by equation (9), δV , will be buried within electrical noise. There will be four electrical contributions to the noise: amplifier voltage noise e_n , amplifier current noise i_n , Johnson noise, and 1/f noise. The voltage spectral density of Johnson noise is frequency independent [15, 16]:

$$S_{Th} = 4k_B TR = \frac{4k_B T \rho L}{\zeta \nu}, \quad (11)$$

where k_B is the Boltzman constants, T is the temperature, the second equality comes from the geometric dependence of the resistance and ρ is the resistivity, ζ , ν , and L are the piezoresistor dimensions as defined in Figure 3. The amplifier voltage and current noise spectral densities, e_n^2 and i_n^2 , are also frequency independent. They can be estimated from the amplifier's specification sheet – the current noise will be negligible because the resistance of the metal strain gauge is $\sim 200\Omega$. The voltage noise will be significant and can be measured accurately using a spectrum analyzer. Hooge noise, or 1/f-noise, is named after its frequency dependence [106]:

$$S_H = \frac{\alpha V^2}{fN} = \frac{\alpha V^2}{fn\zeta\nu L}, \quad (12)$$

where α is material dependent constant, N is the number of carriers, n is the density of carriers and f is the frequency. The noise voltage power is determined by integrating the spectral density over the measurement frequency range:

$$\langle V_{Noise}^2 \rangle = (f_{\max} - f_{\min}) \left(\frac{4k_B T \rho L}{\zeta \nu} + e_n^2 + \left(\frac{i_n \rho L}{2\zeta \nu} \right)^2 \right) + \frac{\alpha V^2}{n\zeta \nu L} \ln \left[\frac{f_{\max}}{f_{\min}} \right]. \quad (13)$$

The force noise is determined by combing equations (9) and (13):

$$F_{Noise}^2 = \left(\frac{32 E 1}{3 \pi_l V_0} \frac{tw^3}{L(w-2u-\nu)} \right)^2 \left((f_{\max} - f_{\min}) \left(\frac{4k_B T \rho L}{\zeta \nu} + e_n^2 + \left(\frac{i_n \rho L}{2\zeta \nu} \right)^2 \right) + \frac{\alpha V^2}{n\zeta \nu L} \ln \left[\frac{f_{\max}}{f_{\min}} \right] \right). \quad (14)$$

3.2.5 Instrumentation I: bandwidth and voltage noise

The bandwidth, f_{min} and f_{max} , in equations (13) and (14) is determined by the lock-in amplifier used, in particular the source frequency f , the time constant τ , and the low pass filter roll-off. I will be using a SRS 830 lock-in which has a maximum source frequency of 100kHz, a minimum time-constant of 10 μ s and low pass filter settings of 6 db/oct, 12 db/oct, 18 db/oct or 24 db/oct. The time resolution δ will be determined by the time constant and low pass filter settings, Table 1 summarizes the relationship between these three variables.

Equivalent noise bandwidth ($f_{max}-f_{min}$)	Time resolution, δ
$1/4\tau = 5/4\delta = \lambda\delta$	5τ
$1/8\tau = 7/8\delta = \lambda\delta$	7τ
$3/32\tau = 27/32\delta = \lambda\delta$	9τ
$5/64\tau = 50/64\delta = \lambda\delta$	10τ

Table 1. Time resolution, δ , as a function of time constant, τ , and the equivalent noise bandwidth for each time setting.

For a given filter setting, λ , and source frequency, f , we can determine the force noise and thus force resolution as a function of the time resolution:

$$F_{Noise} = \left(\frac{32}{3} \frac{E}{\pi_i} \frac{1}{V_0} \frac{tw^3}{L(w-2u-v)} \right) * \sqrt{\left(\frac{\lambda}{\delta} \left(\frac{4k_B T \rho L}{\zeta v} + e_n^2 + \left(\frac{i_n \rho L}{2\zeta v} \right)^2 \right) + \frac{\alpha V^2}{n\zeta v L} \ln \left[\frac{f + \lambda/2\delta}{f - \lambda/2\delta} \right] \right)} \quad (15)$$

The source frequency, f , determines the center of the integration window defined by f_{min} and f_{max} . Above the 1/f shoulder – about 100Hz for bipolar junction based pre-amplifiers – the noise spectrum will be

flat, so the drive frequency should not matter as long as it is large enough that the integration window does not extend below the $1/f$ shoulder; *i.e.*, $f_{min} > 100\text{Hz}$. I am interested in the time resolution range from $50\mu\text{s}$ up to 0.1s ; Table 3 lists the appropriate time constant, filter setting and equivalent noise bandwidth for the time resolution settings between $50\mu\text{s}$ and 0.1s . The choice of actual drive frequency is a bit complicated. In theory, above the $1/f$ shoulder the noise spectrum is flat and any drive frequency that places the equivalent noise bandwidth window above the $1/f$ shoulder should work equally well. For the analysis in the following sections, I assume a flat spectrum above the $1/f$ shoulder. However, in practice there will be stray capacitances which will result in phase shifts between the two branches of the Wheatstone bridge. These phase shifts are harder to null out at higher frequencies, but at the lower frequencies $1/f$ noise and noise peaks from power lines (60Hz , 180Hz & 300Hz are most prominent) complicate the noise spectrum.

Time resolution	Time constant	Filter setting	Equivalent noise bandwidth ($f_{max}-f_{min}$)
$50\mu\text{s}$	$10\mu\text{s}$	6 dB/oct	25 kHz
$100\mu\text{s}$	$10\mu\text{s}$	24 dB/oct	7812.5 Hz
1ms	$100\mu\text{s}$	24 dB/oct	781.25 Hz
10ms	1ms	24 dB/oct	78.125 Hz
100ms	10ms	24 dB/oct	7.8125 Hz

Table 2. Time constant, filter setting and equivalent noise bandwidth for time resolution settings between $50\mu\text{s}$ and 100ms .

The noise voltage and noise current, e_n and i_n , are determined by the choice of pre-amplifier. Table 3 lists specifications for four pre-amps: the SRS 560 is a general purpose junction field-effect-transistor (JFET) pre-amp found in most labs, the SRS 552 is a bipolar-junction-transistor (BJT) pre-amp with especially low noise voltage at the expense of a high noise current, the INA103 is a BJT differential amplifier built into a single monolithic integrated circuit, and the DLPVA-100 is an ultra low noise BJT amplifier with limited bandwidth. I have built INA103 pre-amps that can be integrated into the SCPFM microscope

mounted incubator; however, there are some instabilities that arise with the INA103's when the force sensors are immersed in water. I believe these instabilities can be fixed with an input filter, but haven't demonstrated this yet. So, for the analysis that follows and with the data after that, I used the SRS552 pre-amps.

pre-Amplifier	Gain	Current Noise	Voltage Noise
SRS 560	100		4 nV/rtHz
SRS 552	100		1.8 nV/rtHz
INA 103	100	2 pA/rtHz	1.0 nV/rtHz
DLPVA-100	1000	3 pA/rtHz	800 pV/rtHz
DLPVA-100	10,000	3 pA/rtHz	420 pV/rtHz
DLPVA-100	100,000	3 pA/rtHz	400 pV/rtHz

Table 3. Gain, current noise and voltage noise for a variety of pre-amplifiers.

3.2.6 Device optimization: dependence of force resolution on geometry

I now have all the information necessary to use equation (15) to estimate the force noise for the strain sensor. However, equation (15) has one glaring omission: it does not include the mechanical properties of the gold piezoresistor, which stiffens the beam more than one would expect from a simple comparison of the independent spring constants of the polymer beam and metal wire [28]. I use finite element simulations run with CFDRC (CFD Research Corporation) software to simulate the behavior of the full force sensor including the metal wire. That is, I use CFDRC to calculate the displacement, equation 1, and the strain, equation 6, for a given geometry and force. In this section I calculate the force resolution of the force sensor as a function of different geometric parameters in order to optimize the device design. In these calculations, I assume a signal to noise ratio of 1. Before I get to the geometry optimization, Figure 4 shows the basic relation between time resolution and force resolution for three representative beams: longer integration times reduce the noise.

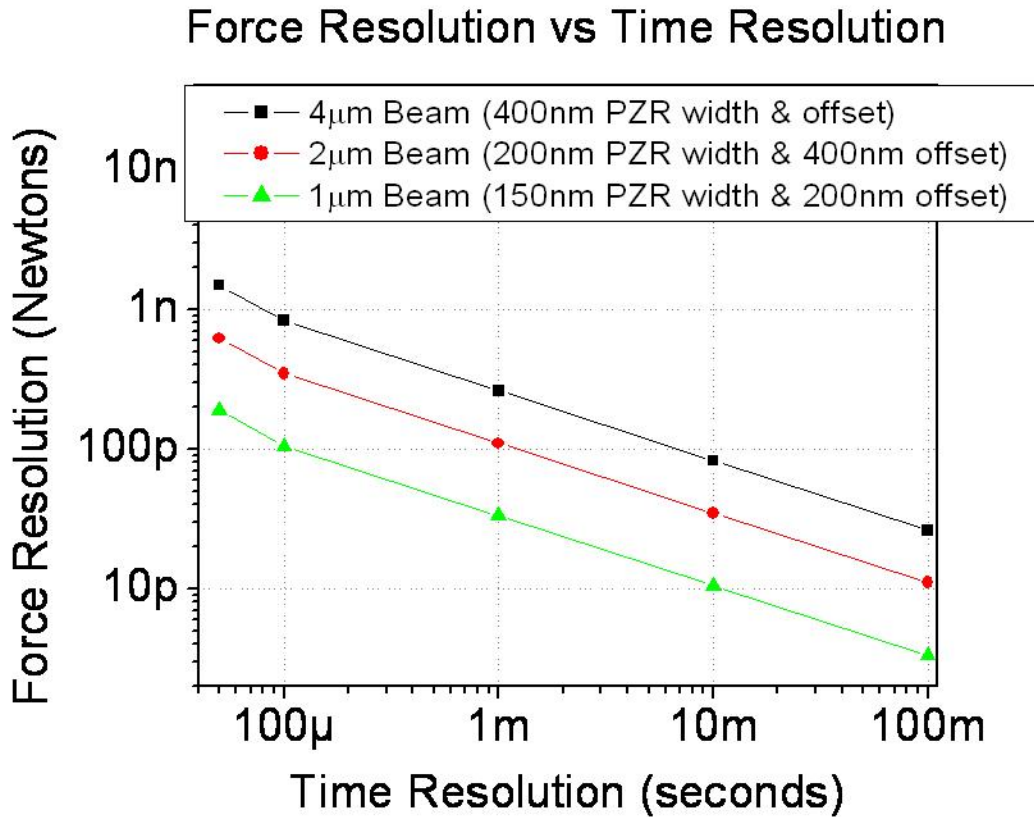


Figure 4. Force resolution versus time resolution for 1, 2 and 4 μm wide beams each of which is 400nm thick with PZR thickness 40nm.

The effects of a few geometric parameters are both intuitively obvious and clear from equation (15): longer, narrower and thinner beams are more sensitive. The force resolution scales linearly with the inverse length and thickness. The in-plane spring constant of a simple doubly clamped beam scales with the cube of the width, but the force resolution scales roughly with the square of the width because wider beams allow room for the piezoresistor to be positioned farther from the center line of the beam and thus couple to larger strains. Building longer, narrower and thinner beams must be balanced against yields which drop for more extreme geometries – I can fabricate 2 μm and 4 μm wide devices with $\sim 75\%$ yields, but so far yields of 1 μm beams have been $\sim 20\%$ – and against the need to present a biologically relevant compliance to the cell. Additionally, adjusting all beam and piezoresistor geometric parameters, except the length, can be done easily from device-to-device, whereas adjusting the length requires two

new photo lithography masks. As a result, all of my fabrication and all of the calculations that follow are for $100\mu\text{m}$ long beams. Figure 5 illustrates the expected dependence of the force resolution on beam width and thickness.

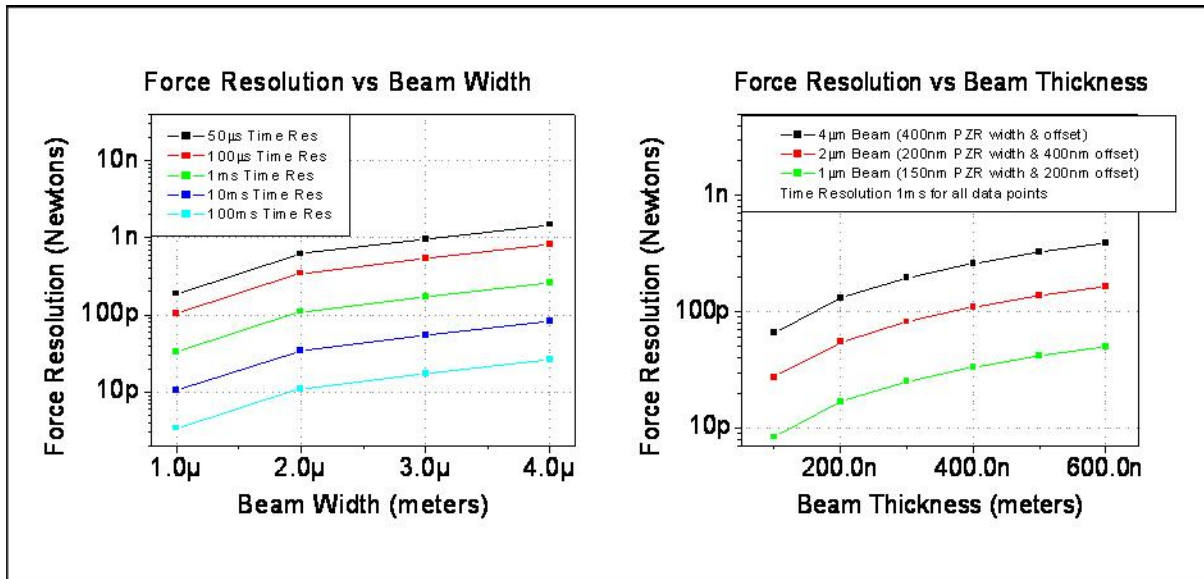


Figure 5. Force resolution versus beam width, at left, and force resolution versus beam thickness at right.

The effects of the piezoresistor dimensions on the transducer responsivity are more complicated than the beam dimensions. Larger piezoresistors have lower noise and the potential to integrate over more of the high strain portions of the beam; however, large piezoresistors will stiffen the beam and reduce the responsivity. Thus, there are optimal values for the piezoresistor width and thickness that depend upon the beam width, thickness and the alignment tolerance with which the piezoresistor can be aligned to the beam – a parameter I refer to as the piezoresistor offset, u in Figure 3. Figure 6 shows the force resolution as a function of piezoresistor offset and piezoresistor width. The offset is determined by the quality of the alignment algorithm used by the electron beam lithography tool – the Leica EBPG, which can only be used with the nitride membrane fabrication process (section 3.3.3) can easily achieve 30-50nm offsets, whereas the FEI Quanta is limited to 200-400nm offsets depending upon the yield one is comfortable with. The piezoresistor width is the easiest piezoresistor parameter to control and adjust,

and has the most significant impact on the mechanical properties of the beam. Figure 7 shows the force resolution as a function of piezoresistor thickness.

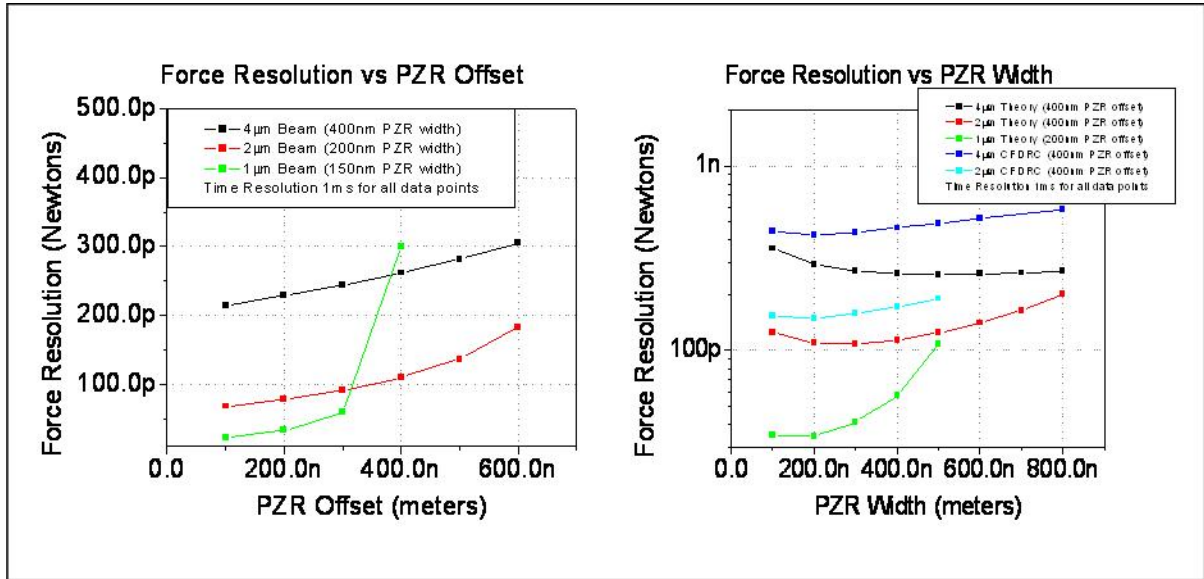


Figure 6. Force resolution versus piezoresistor offset, at left, and force resolution versus piezoresistor width at right. The offset is a function of the alignment between different lithography layers which is strongly dependent upon the electron beam lithography tool; the Quanta is limited to 200-400nm offsets, whereas the EBPG can routinely do 30-50nm offsets. It is not worth trying to fabricate 1µm wide beams with the Quanta. The width dependence is interesting because there are actual optimal values: narrower wires have higher Johnson noise but wider wires stiffen the beam. The figure at right also compares analog theory (equation 15) which does not include the mechanical effect of the piezoresistor with the finite element calculations, which do include the piezoresistor.

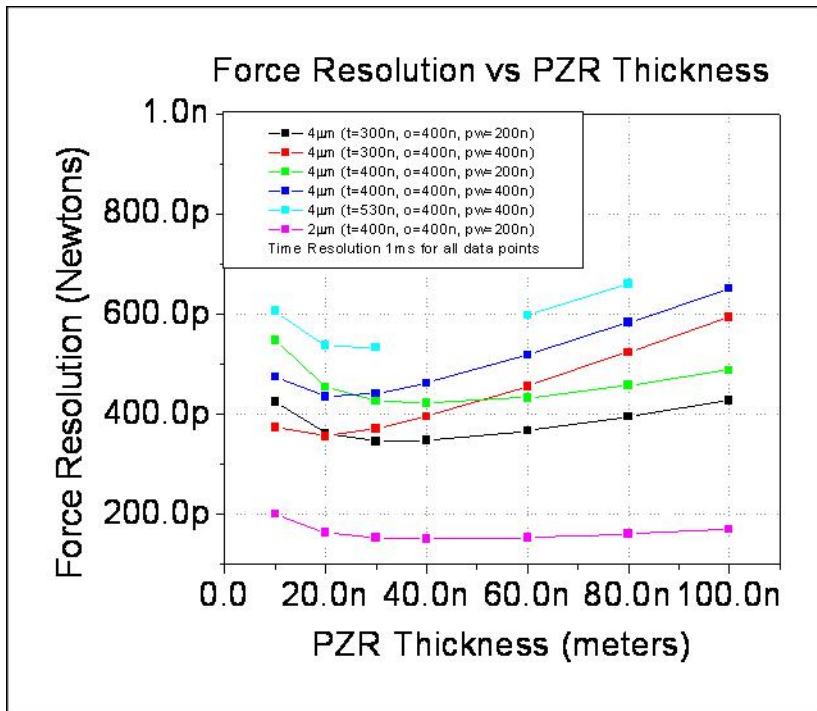


Figure 7. Force resolution versus piezoresistor thickness. For the same reasons as the piezoresistor width, there is an optimal value for the thickness. Unfortunately, the thickness is determined by the piezoresistor evaporation, so it cannot be varied across a single wafer and the thickness monitor is accurate within only about 20%.

The force resolution versus time resolution for the most recent batch of devices that I fabricated is plotted in Figure 8, and SEM images of the devices are shown in Figure 19.

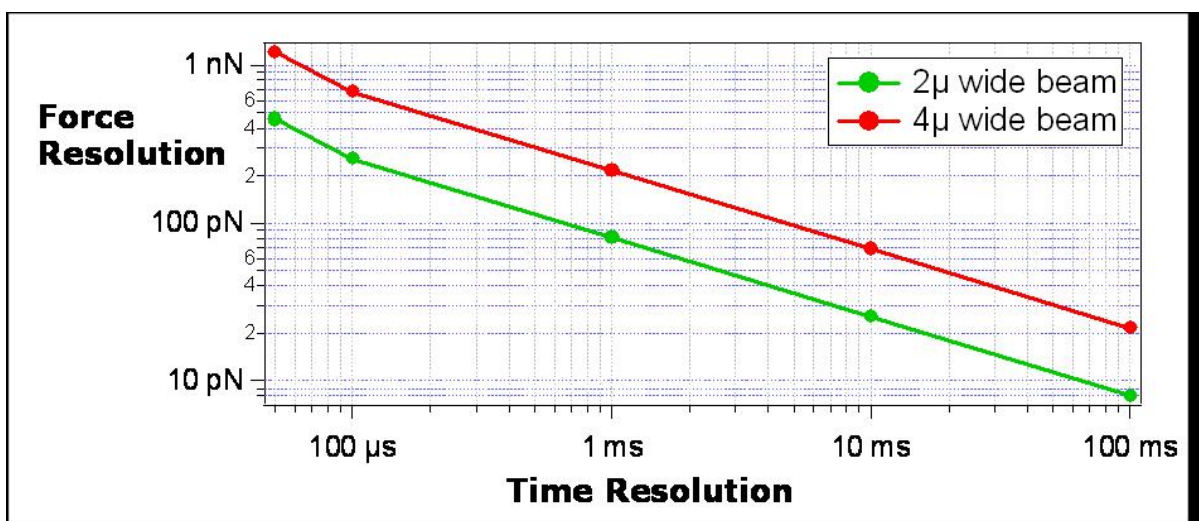


Figure 8. Force resolution as a function of time resolution for the most recent batch of force sensors, pictured in Figure 19. These devices are $100\mu\text{m}$ long, $2\mu\text{m}$ and $4\mu\text{m}$ wide, and 220nm thick. The piezoresistor in these devices is 200nm wide, 50nm thick and offset from the beam edge by 200nm .

3.2.7 Instrumentation II: nulling & dyanmic range

In the previous sections I have estimated the minimum force resolution – both absolute force level and minimum detectible change in force. Another key parameter is the dynamic range of the measurement: the maximum force that can be measured at the same instrument settings that enable the optimized force resolution calculated previously.

There are two processes that may limit the maximum force: 1) the onset of non-linearities in the strain-sensor deformation, and 2) saturation of electronics. A Summer Undergraduate Research Fellowship (SURF) student, Ted Dickle, spent some time investigating the transducer responsivity's dependence upon both applied force and the out of plane component of the applied force – cells spread very flat and pull almost tangentially to flat surfaces, but not perfectly. Ted found that for forces less than 100nN and angles less than 5 degrees, non-linear effects can be neglected (Figure 9).

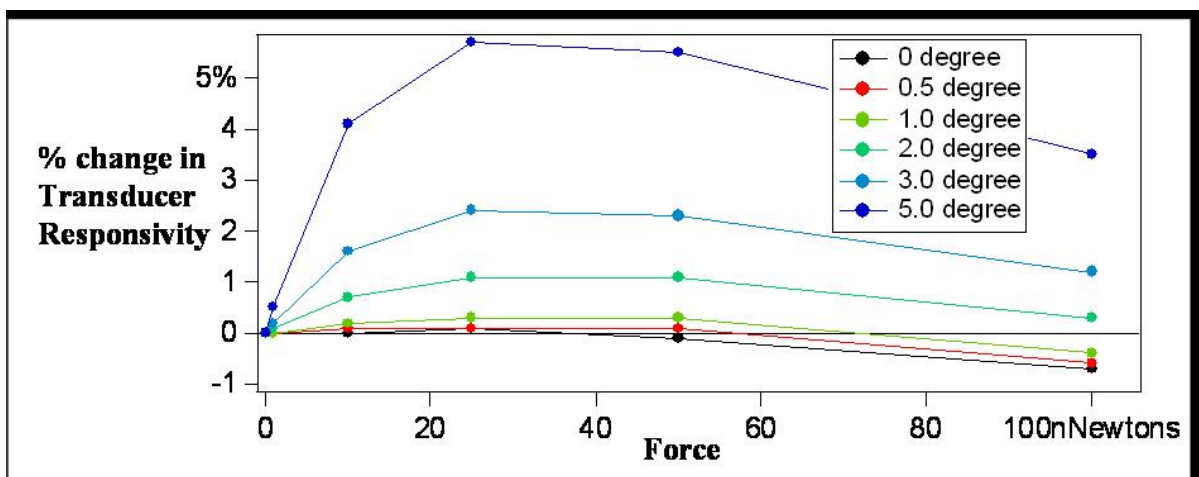


Figure 9. Non-linear effects manifest as changes in the transducer responsivity. The percent change in transducer responsivity is plotted as a function of applied force for a range of out-of-plane pulling angles. The plot shows results from a finite element simulation (CFDRC), done by SURF student Ted Dickle, of a $2\mu\text{m}$ wide beam. There are two competing effects that create the rise and then fall in the percent change

in transducer responsivity: buckling of the beam due to the out of plane force component distorts the strain field and raises the responsivity, whereas at higher forces nonlinear stiffening of the beam reduces the responsivity. Overall, the percent change for pulling angles of 3° or less are very small; however, the sudden rise in responsivity from 0 to 20nNs for the 5 ° pulling angle is a little worrisome and must be kept in mind when interpreting data.

Instrument saturation is limited by the lock-in amplifier's maximum input sensitivity of 1V or the minimum bit size of the 24 bit analog-to-digital converter card that I use to stream the data from the lock-in to my computer (National Instruments, PCI-4722). For the purposes of this discussion, I assume a relatively high 1V drive voltage and transducer responsivity of 1000V/N which will give a force sensitivity of 20pN with 10ms time resolution. A 100nN force will thus generate a 100 μ V signal at the input of my pre-amplifier. The 100nN signal will add to the zero-force signal due to fabrication imbalances in the Wheatstone bridge. Fabrication issues limit that balance to about 1 in 10³, which gives a 1mV signal from a 1V drive, but the two branches of my Wheatstone bridges have separate inputs so I can use a 6-decade ratio transformer (an AC voltage divider) to reduce the imbalance further. In practice, I can reduce the imbalance to roughly 1 in 10⁵, which gives a 10 μ V fabrication imbalance signal which add to the 100nN signal. The combined 110 μ V signal is amplified by the pre-amplifier before reaching the lock-in. The SRS552 pre-amp and the INA103 both typically operate with a gain of 100, which boosts the 110 μ V to a reasonable 11mV signal and a lock-in sensitivity of 100mV resulting in another factor of 100 gain before the A-to-D converter. If I assume 20 bits of that 24 are usable, the minimum bit works out to be 1pN which does not limit the 20pN electronic noise; the electronics measurement system has a full five decades of dynamic range. It is worth noting that the Fempto DLPVA-100 pre-amplifier, which has impressively low voltage noise of 400pV/rtHz and 420pV/rtHz but high gain of 100dB and 80dB respectively (Table 3), will saturate the lock-in amplifier's input at the two low noise settings. Figure 10 plots the sensitivity and dynamic range of SCPFM, substrate deformation methods and optical bead methods with the biological regimes of interest in a force vs time depiction of the measurement space.

(Figure 10)

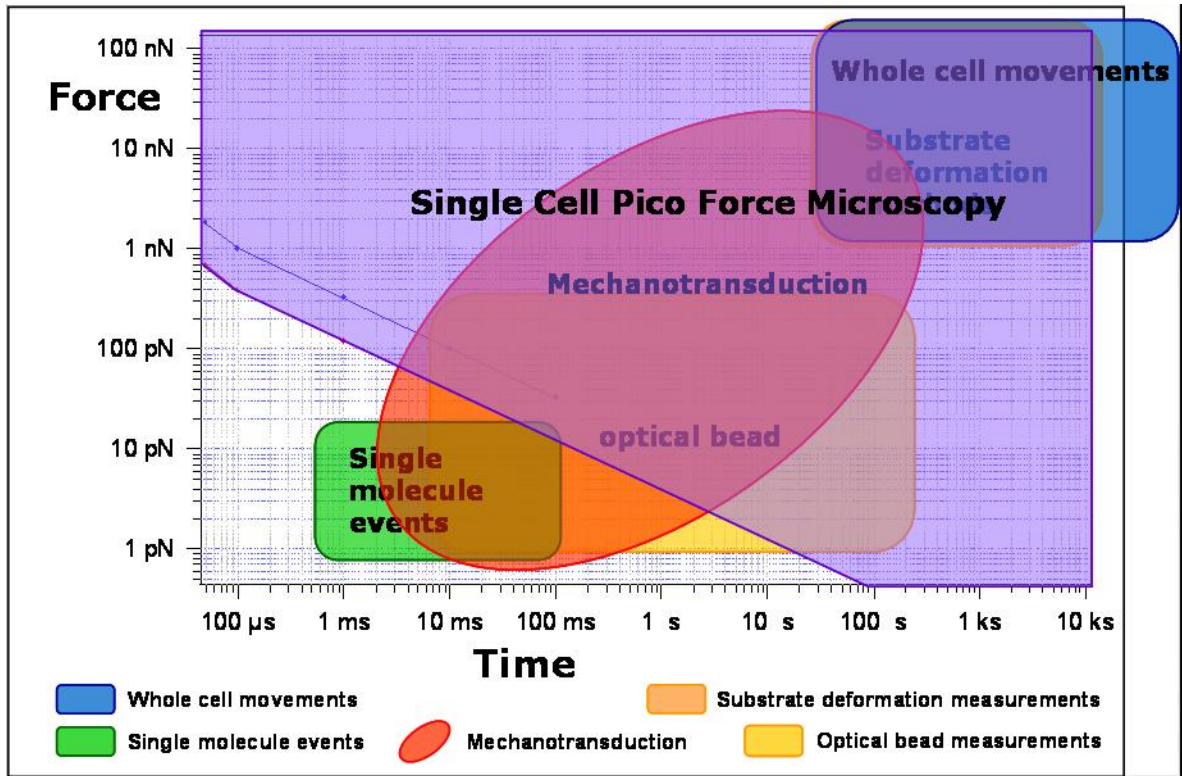


Figure 10. The measurement range in force and time of substrate deformation methods, optical bead measurements and SCPFM is plotted with the ranges in which single molecule events, whole cell movements and mechanotransduction occur. SCPFM has the sensitivity necessary to observe macromolecular events and the dynamic range to monitor whole cell movements.

3.2.8 Thermal drifts

Long term measurements are limited by systemic drifts in the system. There are intermittent drifts that can be bad on some days and completely absent on others. At present I don't understand and do not have control of these drifts.

Temperature drifts can cause problems. Large imbalances in the Wheatstone bridge will convert thermal drifts of the entire Wheatstone bridge into signals [107]. I am typically able to balance my devices to 1 part in 10^5 at which point a 1C degree drift – one part in 310 – results in a shift of 3 parts in 10^8 , which is well below my measurement threshold. I am fairly confident in the thermal stability of my system within 1C; see section 3.6.1 for further discussion.

Drifts in the temperature difference between the force sensing and reference arms of the Wheatstone bridge pose a much greater problem because they are directly translated into a measured change in resistance. At room temperature, the bulk resistivity of gold depends linearly on temperature, T [108]:

$$\rho_{gold} = \left(8.23 \times 10^{-11} \Omega \cdot m / K\right) T - 0.19 \times 10^{-8} \Omega \cdot m. \quad (16)$$

Plugging in the piezoresistor geometry for a typical force sensor indicates that the temperature coefficient is nearly unity: $0.69 \Omega/K$. The exact signal that a given temperature drift between beams will create depends on the specific beam geometry, drive voltage, pre-amplifier and lock-in settings. However, plugging the numbers from the data I will present in chapter 4, 0.5V drive voltage, 37.5 V/N transducer responsivity and a 100ms time resolution, shows that a $20\mu K$ drift in temperature between the two legs of the Wheatstone bridge will create a 200pN signal – which is the measured noise floor. The entire Wheatstone bridge is integrated onto the NEMS chips; the two legs are positioned within $30\mu m$ of each other, precisely to reduce the possibility of drifts between the two beams.

3.3 Device fabrication

3.3.1 Fabrication basics

The NEMS devices are fabricated from lithographically patternable polymer instead of traditional MEMS materials, such as SOI, principally because polymer's low Young's modulus enables improved sensitivity and the fabrication of devices that are compliance matched to typical biological materials. Additionally, the material costs for polymers are significantly less than traditional semiconductor materials. The first efforts to fabricate MEMS devices from polymers focused on making AFM tips from SU-8 [102]. Springing from that work the Boisen group has put significant effort into fabricating cantilever based MEMS detectors from SU-8 [109]. My work is the first effort to fabricate NEMS devices from polymers, so a significant amount of work was required to develop the process. The first fabrication process I

developed was an all-polymer and metal process based on work by Thaysen *et al.* [102]. I will discuss this process in detail below. I later switched to a silicon nitride membrane-based fabrication process which resulted in higher yields and better cell culture than the all-polymer process.

Both processes require fabricating a long trench-shaped cell chamber, roughly 600-800 microns long and 110 microns wide, that is spanned by the force sensing beams and a bridge to hold the cell being studied in close proximity to the beams. The beams are fabricated from two layers of polymer, each ~100 nm thick, that sandwich the gold PZR strain gauge, thus keeping the PZR insulated from the surrounding liquid and symmetric – decoupled – with respect to out-of-plane deflections. There are two additional metal layers in each process: the “pad” layer which sits on the top surface of the force sensing beams and the cell bridge to define a region where the cell will attach and the “conductor” layer which is a thick layer of metal that connects the PZR strain gauge out to pogo-pin contact pads.

Both processes are built around the same basic chip architecture. Each chip contains four cell chambers with one cell bridge and two force sensors per chamber, for a total of eight force sensors per chip. There are 40 electrical connections for contacting the eight force sensors on each chip, which takes up a fair amount of real-estate. Additional room must be left for the microfluidics, resulting in moderately large chips: 18mm x 18mm for both processes. Both processes are fabricated on the wafer scale, 3-inch for the all-polymer process and 4-inch for the nitride membrane process, with nine 18mm chips per wafer for a total of 72 force sensors per wafer.

Force sensors have been fabricated from four different types of polymer. I have fabricated for sensors from two different SU-8 formulations and from polyimide. Renaud Richard, a graduate student who worked with me for a brief time, fabricated force sensors from Parylene. A brief introduction to each of these polymers follows and a comparison of the basic polymer characteristics is included in Table 4.

3.3.1.1 SU-8

SU-8 is an epoxy based, negative photoresist first invented by IBM in the late 1980s [110, 111]. It is spin deposited from a cyclo-pentanone solution, soft-baked to remove the cyclo-pentanone, UV exposed to drive the cross-linking of the epoxy monomers, post-exposure baked to speed the cross-linking reaction, developed in propylene-glycol-methyl-ethyl-acetate to remove the uncross-linked material and finally hard-baked to complete the reaction. SU-8 was developed for MEMS materials and is quite easy to fabricate structures from layers ranging in thickness of 100nm up to 100 μ m with [112-114]. There are a number of drawbacks to SU-8, principally the baking and cross-linking processes generate high internal stresses within the polymer [115, 116]. Additionally, SU-8 monomers and solvent are not biocompatible and must be fully removed from the SU-8 for biology applications. However, with sufficient hard baking one can sufficiently drive the solvent and monomers from SU-8 structures [117, 118].

There are two SU-8 formulations in common use, the 2000 series and the 3000 series. The 3000 series was developed to reduce the internal stress and Young's modulus by mixing in an inert polymer that essentially dilutes the cross-linking. I began my work using the 2000 series, which is well characterized, but have switched in the last two years to the 3000 series to take advantage of the reduced Young's modulus and internal stress. I get very good fabrication results with the 3000 series.

3.3.1.2 Polyimide

Polyimide is a polymer of imides that is spin deposited. Polyimides are used in many applications including Kapton heaters and flexible circuit materials, as stress buffers and passivation layers over semiconductor circuitry. Like SU-8 polyimide is spin deposited; unlike SU-8, polyimide is thermally cured and has a very high glass transition temperature, >400C [119, 120]. The principle difficulty that I have had at this point with polyimide is the presence of contaminant particulates that result in uneven

layer thickness; a simple filtration process should fix this problem. Assuming the filtration process can be fixed, polyimide may be a preferable material SU-8 because its higher glass transition temperature should allow higher drive voltages which scale linearly with the transducer responsivity equation (10).

3.3.1.3 Parylene

Parylene is a poly-para-xylene based polymer that is unique among polymers because it is deposited by low pressure chemical vapor deposition (LPCVD) in a three-step process: a high temperature vaporization of the solid dimer, a vacuum driven pyrolysis of the dimer into stable monomers and polymerization onto the target substrate at room temperature [114]. Parylene coatings have very low permeability to moisture and gases and are generally inert and biocompatible. Due to the LPCVD the coatings are conformal, “stress free” and solvent free [114, 121]. All of these are excellent characteristics for polymer based NEMS devices. The principle problem with Parylene is controlling the thickness of very thin (100nm) depositions. The deposition tool which the Roukes Group owns is poorly engineered, with large surface areas, a long vacuum track for executing the multi-step LPCVD deposition and no end-point detection or control. As a result the Parylene deposition distribution throughout the chamber, and thus final deposition thickness, drifts significantly from run to run on the 100nm scale. This makes consistent fabrication of 100nm thick layers an unacceptably low yield process.

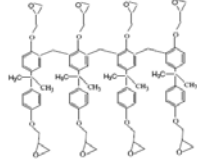
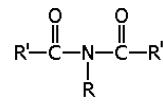

	SU-8 2000	SU-8 3000	polyimide	Parlyene
Young's modulus	4.4 GPa	2.0 GPa	3.2 GPa	3.2 GPa
internal Stress	~10 MPa	~1 MPa	~10 MPa	"stress free"
Poisson ratio	0.22	0.22	0.34	0.4
thermal conductivity	0.2 W/mK	0.2 W/mK	0.12 W/mK	0.08 W/mK
glass transition temp	55C	55C	400C	85C
deposition method	spin	spin	spin	LPCVD
advantages	fabrication	fabrication, Young's mod	thermal	bio compat., low stress
disadvantages	stress, bio incompat.	stress, bio incompat.	particulates, fabrication	thickness control
monomer structure				

Table 4. Key characteristics of the four polymers which have been used to successfully fabricate NEMS force sensors for SCPFM.

3.3.2 The all-polymer process

The core idea of the all-polymer process is that all of the device structure – the chip with trench, the polymer beams and all three metal layers – is built on a silicon wafer that serves merely as a carrier wafer during fabrication. Late in the process the polymer chip is released from the carrier by etching away a sacrificial chrome layer. This is based upon Thaysen's process for building AFM cantilevers from SU-8 [102]. The reason I chose this process is that it requires no plasma etching. At the time the process development began, the Roukes Group's etch capabilities were limited to a home built ECR etch tool that can only handle small pieces of silicon (<2cm square) and is optimized for relatively short, gentle, typically isotropic etches of silicon compounds. The ECR etch tool is not compatible with the wafer scale fabrication necessary to build devices that are large enough to enable microfluidic fanout nor to build devices in sufficient quantity to be disposable. So, I developed the all-polymer process which requires no plasma etch steps.

The all-polymer fabrication process is diagramed in Figure 11 and detailed instructions are given in Appendix 2. I start with 3-inch wafers, typically working in batches of 4. The first step is an electron beam evaporation to deposit the sacrificial metal layer: a thin layer ($\sim 20\text{\AA}$) of titanium for adhesion, a thicker layer ($\sim 500\text{\AA}$) of gold to improve wetting and accelerate the release etch and a thicker layer ($\sim 500\text{\AA}$) of chrome that is etched during the release step (Figure 11b). In the second step, the gold alignment marks are patterned by photo lithography and deposited using electron beam evaporation and liftoff (Figure 11c). It is important to achieve high quality alignment marks to ensure good alignment between the piezoresistive strain gauge and beams edges; my photo lithography processes are optimized to routinely achieve sub-micron resolution. In the third step, the bottom of the polymer beam is spin deposited and written directly using electron beam lithography in the Quanta ESEM (Figure 11d). SU-8 is used because it is sensitive to electron beam lithography; the Quanta ESEM is used because the low acceleration voltages result in sharper feature sizes with SU-8 which is actually very sensitive to electrons. Electron beam patterned SU-8 can achieve resolution of approximately 200nm, which is not particularly good for electron beam lithography processes. The source of this limit is two-fold: SU-8 is extremely sensitive to electrons (a $2\text{-}4\mu\text{C}/\text{cm}^2$ dose is typical) so even trace backscattered electrons will excite and cross-link the material. Furthermore, SU-8 is not directly cross-linked by the electron beam energy, rather the energy is absorbed by an acid initiator which then drives the cross-linking process; unfortunately, this initiator is a small molecule that can diffuse before reacting, thus further limiting resolution [113]. In step four, the piezoresistive strain gauge is patterned using electron beam lithography on Poly MethylMethAcrylate (PMMA), deposited using electron beam evaporation and liftoff (Figure 11e). An organic titanate (AP300) is spun beneath the PMMA to enable adhesion between the beam bottom and a thin layer of titanium; approximately 500\AA of gold is patterned on top of the titanium to define the actual piezoresistor. In the fifth step, the beam top is deposited and defined in the same manner as the beam bottom in step three (Figure 11f). In step six, the metal pads which define the cell adhesion area are patterned in the same manner as the piezoresistor in step four (Figure 11g). In the

seventh step, the conductor metal that fans out to pogo-pins contact pads is deposited (Figure 11h). The conductor metal is thick, $\sim 1\mu\text{m}$; in order to withstand the flexing of the polymer chip after it is released, the metal is patterned using a tri-layer photo lithography process and deposited with electron beam evaporation in phases to prevent over heating and stress which cause adhesion failure. The polymer chip body with trench is patterned in a two-step process (Figure 11i). In step eight, a thin ($\sim 2\mu\text{m}$) layer of SU-8 is deposited and patterned using photo lithography. This SU-8 layer is cross-linked to a moderate degree – full soft bake exposure and post-exposure bake but no hard bake – in order to ensure adhesion to the metal layers below. In step nine, a thick ($\sim 80\mu\text{m}$) layer of SU-8 is deposited and patterned using photo lithography, and this layer is minimally cross-linked – long time but low temp with ramping is used for all three bake steps – in order to keep the internal stress in the layer to a minimum. If fully cross-linked, this layer will actually rip itself apart during the release step and without careful optimization the stress will be sufficient to tear the force sensing beams apart (Figure 12). In step ten the polymer chips are released from the carrier wafer using a gentle, aqueous chrome etch and are dried using a critical point drier (CPD) (Figure 11j). In step eleven, the dried chips are attached to a glass cover slip that has been coated with a thin layer of poly dimethyl-siloxane (PDMS) (Figure 11k). The PDMS serves a dual purpose: it adheres the polymer chip to the glass and it is gas permeable which is important for removing air bubbles from the trench region around the beams. Finally, the multilayer microfluidics chip, discussed in detail in section 3.4, is attached to the backside of the chip (Figure 11l and Figure 13).

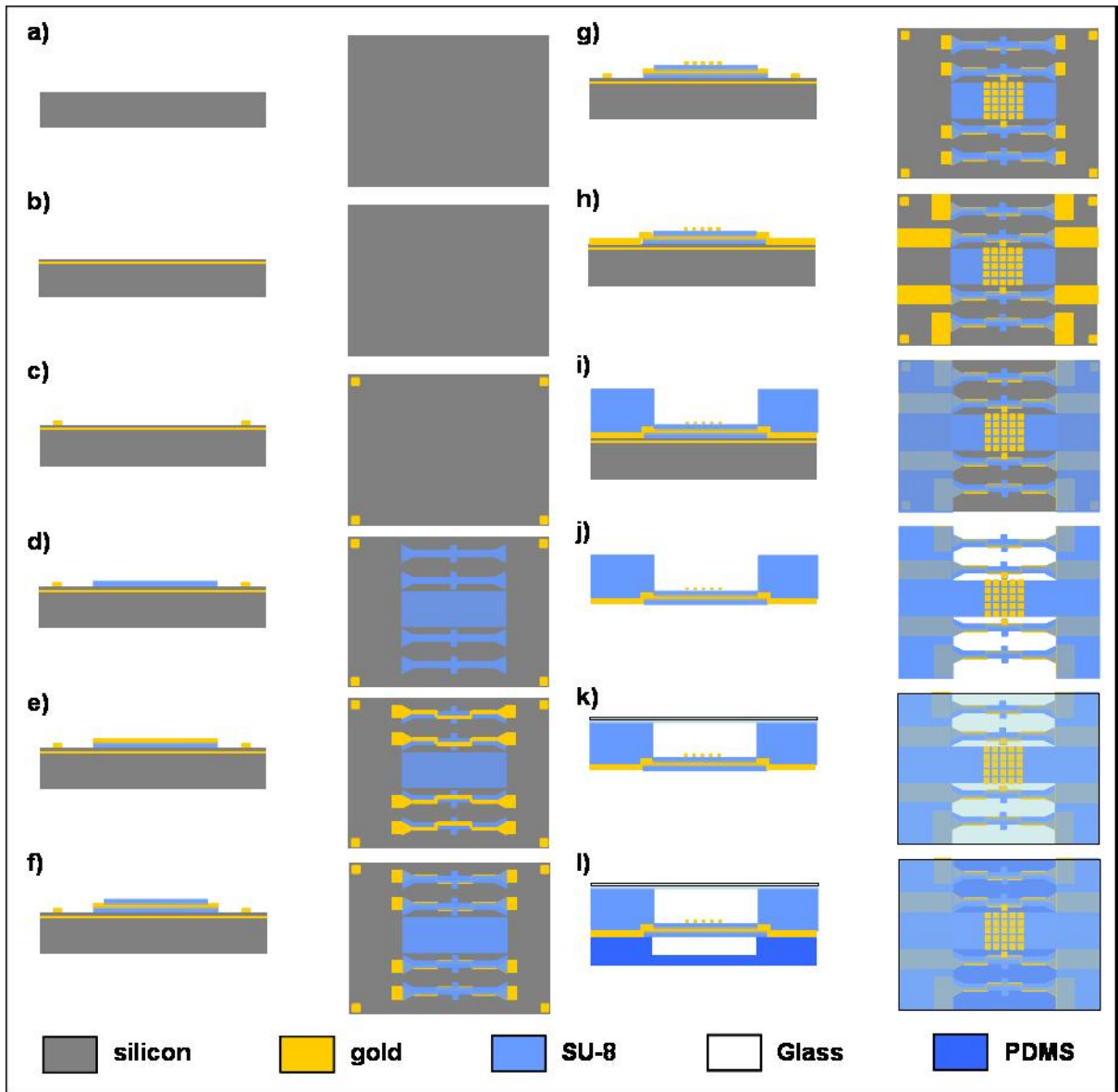


Figure 11. All-polymer fabrication process step-by-step in cross section and top view. a) silicon wafer. b) sacrificial gold/chrome layer. c) gold alignment marks. d) beam bottom. e) gold piezoresistor. f) beam top. g) gold pad layer. h) gold conductor. i) chip body with trench. j) etch sacrificial layer to release from wafer and suspend beams. k) seal frontside and create optical window with PDMS coated glass coverslip. l) seal backside with multilayer microfluidics chip.

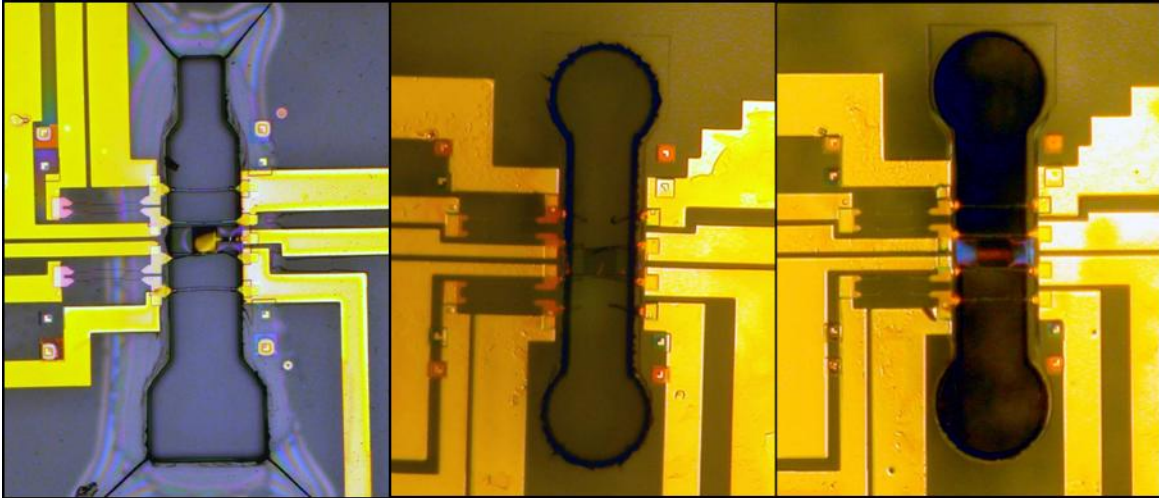


Figure 12. Stress and cracking in the polymer chip body. At left, early design suffered from extensive cracking. At center, rounded corners eliminate cracks, but stress still breaks the beams. At right, when the process is optimized the beams survive.

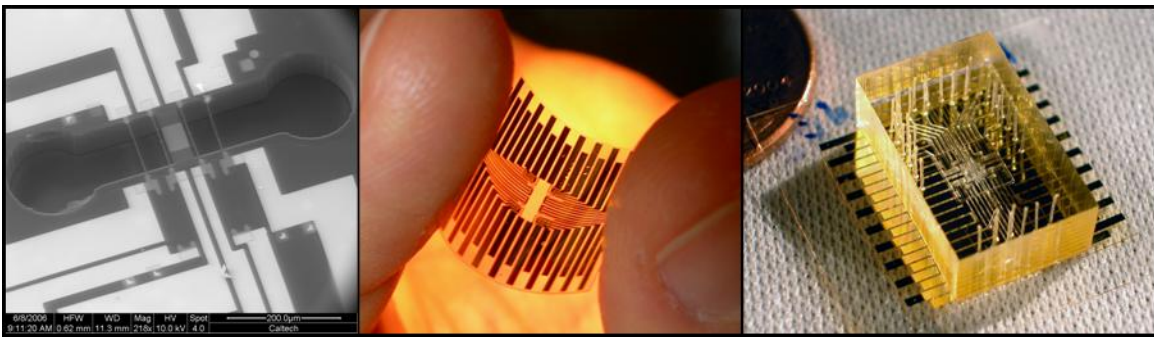


Figure 13. Completed all polymer chips. At left, an SEM micrograph. Center, a chip held between thumb and forefinger before mounting on a PDMS coated cover slip. At right, a microfluidics encapsulated device, note the penny in the upper left corner for scale.

This fabrication process is quite difficult. SU-8 patterning by electron beam lithography is a rather novel process and is not well refined. Controlling the stress within the thick SU-8 layer which makes up the chip body and defines the trench is very difficult and critical (Figure 12). There are four polymer layers and three metal layers in the chip, so each layer must be well optimized to achieve moderate yields. Nevertheless, I have succeeded in fabricating whole wafers of these all polymer force sensors with moderate yields of $\sim 50\%$ (Figure 13).

There is, however, a critical problem with this fabrication process that surfaced when I encapsulated the devices in microfluidics and introduced cells. In order to achieve low stress in the SU-8 that makes up the chip body, the baking and exposure are minimized; as a result solvent, photo-initiator and unpolymerized SU-8 remain in this layer. Due to the large SU-8 surface-to-fluid-volume ratio in the cell chamber, $0.02\mu\text{m}^{-1}$, one or more of these compounds is able to leach out and poison the cells in the trench. If the chips are over-cured, the solvent, photo-initiator and unpolymerized SU-8 are removed or reduced to an extent that the cells will live for short times (~ 24 hours) but the stress in the layer damages the force sensors. I spent a fair amount of time trying to optimize the fabrication process in search of a sweet spot where the SU-8 is cross-linked sufficiently to enable cell culture but not so far as to tear the force sensors apart. Unfortunately, I found a dead zone instead: enough stress developed to break the force sensors but the cells were still dead (Figure 14). Efforts were also made to remove the solvent, initiator and unpolymerized SU-8 by a dialysis process before the CPD, various media exchange and rinse protocols were tested to remove the contaminants both before and during cell culture and Pluronic 68 was tested in hopes of forming micelles around the contaminants, but nothing worked.

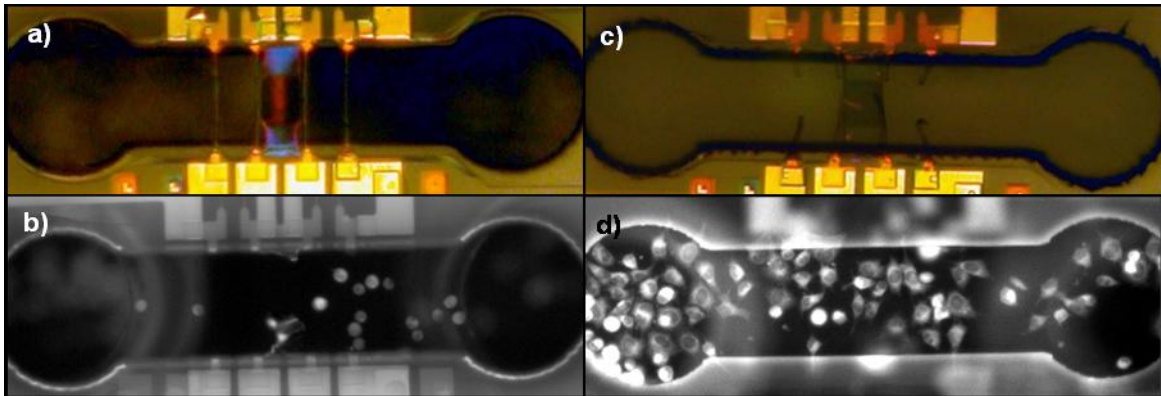


Figure 14. Failed efforts to culture cells in low stress all polymer devices. Images a) and b) show low stress devices with good force sensors (a) but dead cells (b). Images c) and d) show slightly higher stress devices with spread cells (d) but broken beams (c).

3.3.3 SiN membrane process

Fortunately, by this time the Roukes group had acquired a new etch tool: an 8" compatible bench top micro Reactive Ion Etch (micro-RIE), thus enabling wafer scale plasma etching of both silicon compounds and polymers. Silicon nitride membranes have long been used in MEMS fabrication beginning with x-ray masks [122, 123], pressure sensors [124] and AFM tips [125]. The principle difference in my work, besides the smaller scale, is that I am fabricating polymer NEMS devices on top of a nitride membrane and then removing the membrane from beneath the NEMS devices, to suspend them. An alternative view of the process is to observe that the polymer NEMS devices are fabricated on a silicon substrate and suspended using a through wafer etch; the nitride membrane simply serves as an etch stop for the through wafer etch.

The nitride membrane process has a number of important advantages over the all-polymer process. Principally, the trench that surrounds the cell chamber is made of silicon, not low stress SU-8, and thus will not leach poison into the cell chamber. There is still polymer, typically SU-8, in close proximity to the cells – the beams and cell bridge – however, this polymer has been fully cross-linked and hard baked, so the SU-8 is fully cross-linked and all solvent, photo initiator and un-polymerized SU-8 have been removed. Furthermore, the surface-to-volume and volume-to-volume ratios of SU-8 to culture media have shifted radically. The switch from the all-polymer devices to the nitride membrane process reduced the SU-8 to fluid volume-to-volume ratio by more than eight order of magnitude and the SU-8 surface to fluid volume ratio by nearly three orders of magnitude (Table 5). An additional advantage is that the substrate is not flexible; this reduces stress on the beams which increases sensitivity and reduces the odds of breaking the beams due to stress or mishandling of the devices, thus raising yields.

	All-Polymer	Nitride membrane
SU-8-volume-to-fluid-volume	4×10^4	1×10^{-5}
SU-8-surface-to-fluid-volume	$0.02/\mu\text{m}$	$4 \times 10^{-5}/\mu\text{m}$

Table 5. Comparison of SU-8 and fluid ratios for the all-polymer and nitride membrane fabrication processes.

The micro-RIE enabled additional improvements to the fabrication process beyond the switch to the nitride membrane process. Instead of defining the polymer force sensors by direct writing the SU-8 with the Quanta ESEM, I can now deposit and cure a thin layer of any polymer (both SU-8 formulations, Parylene and polyimide have all been used successfully), pattern a metal etch mask on top of the polymer using electron beam lithography on PMMA, etch the polymer using an oxygen plasma in the micro-RIE and remove the metal etch mask. This has many advantages. First, only one writing step is needed to pattern both polymer layers of the beams instead of two. Second, the Leica EBPG 5+ electron beam writing tool can be used to pattern the PMMA which results in significantly improved alignment between the piezoresistive wire and the edge of the beam – see plots in section 3.2.6 – and enables significantly smaller beam-ledge gaps – $1\mu\text{m}$ is routine on the EBPG, $4\mu\text{m}$ was the standard on the Quanta. Third, the oxygen etch in the micro-RIE results in much cleaner sidewalls on the beams. Fourth, wafer scale writing with the EBPG is significantly faster and more robust than the Quanta; this is due to the higher beam currents that the EBPG can generate without compromising spot size and the radically faster alignment routines that the EBPG uses. When optimized, the Quanta requires 2.5 hours to pattern one wafer whereas the EBPG can write the same pattern with improved alignment in less than 5 minutes.

There are two disadvantages to the nitride membrane process. The chips are opaque, which makes it difficult to monitor the microfluidics when operating in the microscope mounted sample holder and incubator. This problem is partially dealt with by opening four strategically placed windows during the through wafer etch to observe the microfluidics through the chip. The second problem is that the KOH through wafer etch leaves a large and odd shaped chamber around the beams; the cell chamber volume increases from 5.7nL with the all-polymer devices to 150nL with the nitride membrane process. This

chamber is difficult to rinse both because of its size and its shape – the KOH etch leaves hard-to-reach corners. This adversely affects my ability to precisely perturb the cells with microfluidics.

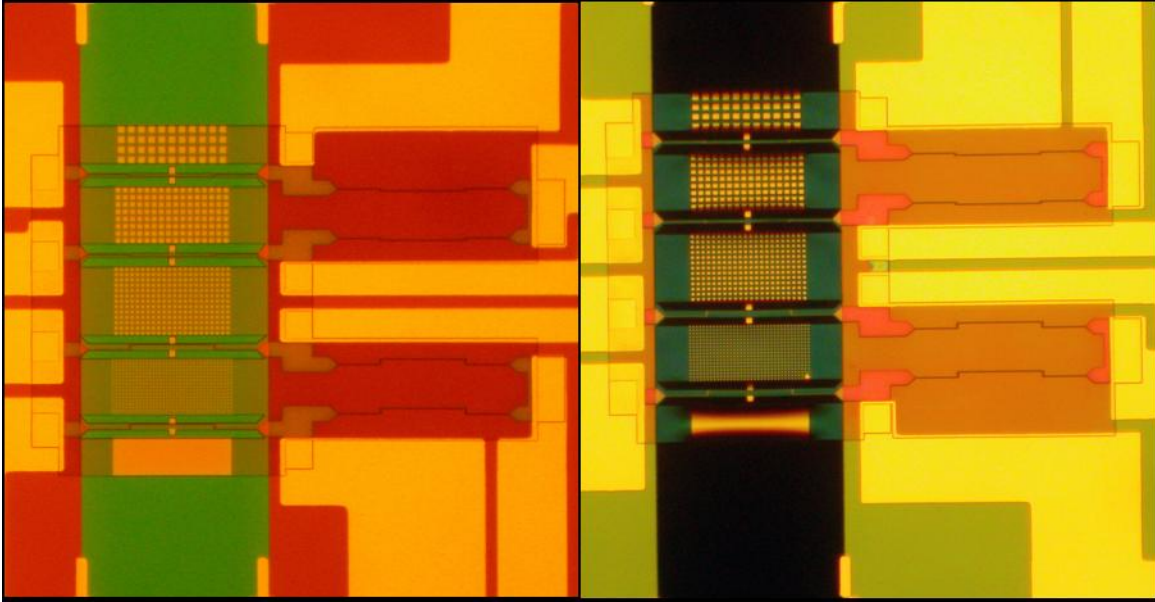


Figure 15. Nitride membrane based force sensors before (left) and after (right) the hybrid etch process which selectively removes the nitride membrane without damaging the polymer beams.

The critical new step in the nitride process was developing an etch that would remove the silicon nitride membrane from below the polymer beams without damaging the beams. I developed a hybrid etch process that works very well (Figure 15). After the membrane has been defined beneath the polymer devices using backside alignment and a KOH etch through the wafer, a $\text{CF}_4\text{-O}_2$ plasma is used to etch almost all of the way through the nitride membrane. The $\text{CF}_4\text{-O}_2$ plasma, or any plasma etch for that matter, will etch through the polymer beams much faster than through the silicon nitride, or any crystalline material. The micro-RIE is a relatively unstable tool without endpoint detection, so a series of short etches with visual checks are used to ensure the etch does not over-shoot; the thickness can be monitored by the membrane color and the presence of wrinkles – white, wrinkled membranes are ready for the hydrofluoric etch. The final layer of nitride, which I estimate to be 10's of nanometers thick, is removed using an 80C 0.1% hydrofluoric acid etch. Hydrofluoric acid does not etch polymers and when

dilute and heated, preferentially etches silicon nitride over silicon dioxide [126] by the mechanism shown in Figure 16. This is a critical step.

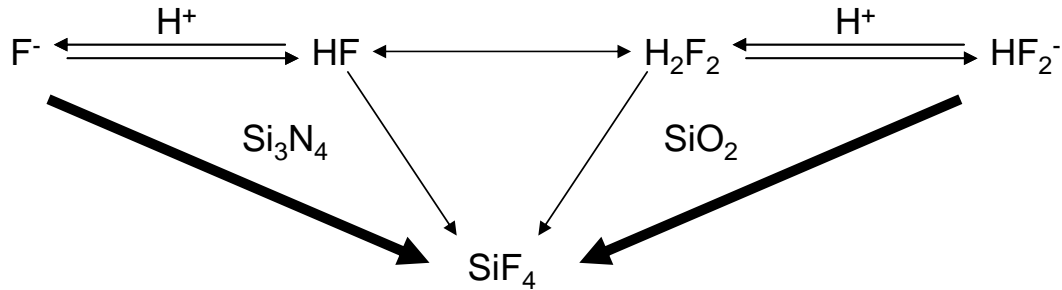


Figure 16. Reaction kinetics of HF with Si₃N₄ and SiO₂. HF dimers etch SiO₂ and HF monomers etch Si₃N₄. Heating dilute HF shifts the equilibrium to the left from HF dimers to HF monomers, thus accelerating the Si₃N₄ etch and decelerating the SiO₂ etch. Figure adapted from Knotter and Denteneer [126].

I have successfully fabricated whole wafers of polymer NEMS force sensors with the silicon nitride process with routine yields greater than 70%. For a typical 3 wafer run, with 9 die per wafer and 8 force sensors per die, this results in approximately 150 force sensors spread out on 27 chips each with an average of 6 force sensors per chip. Devices fabricated at this scale are disposable: a single 4 week fabrication run yields a 6 month supply of chips, assuming each chip is used for 1 week and thrown away. Alternatively, a half time staff member could supply 3 SCPFM tools with sufficient devices to run continuously.

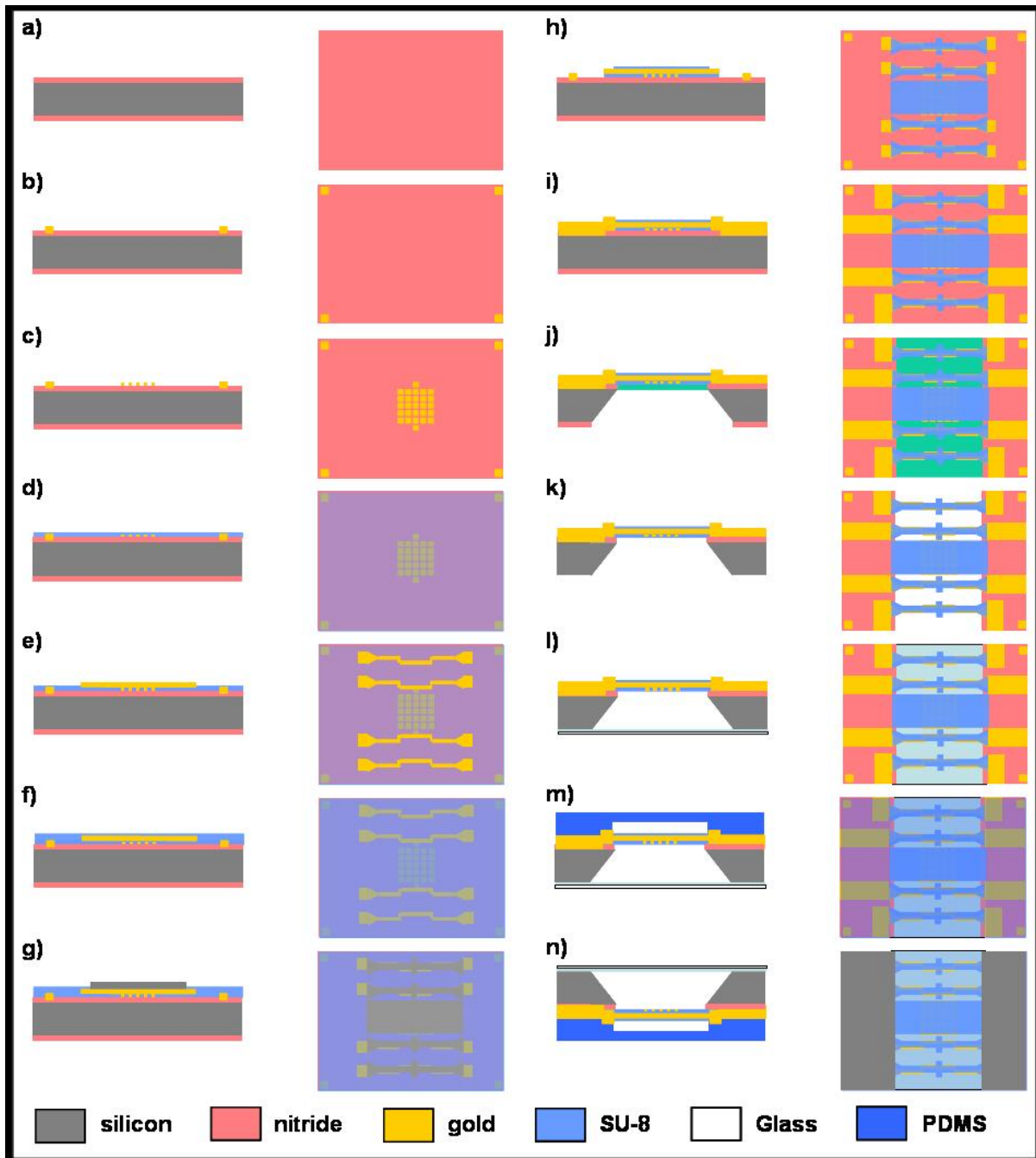


Figure 17. Silicon nitride fabrication process step-by-step in cross section and top view. a) nitride coated wafer. b) gold alignment marks. c) gold pad layer. d) first polymer layer, will become beam top. e) gold piezoresistor. f) second polymer layer, will become beam bottom. g) metal etch mask. h) post-etch beams and cell bridge are defined. i) gold conductor. j) nitride membrane is formed by plasma etch through backside nitride and wet etch through silicon wafer. k) nitride membrane removed with selective hybrid plasma & wet etch process. l) seal backside and create optical window with PDMS coated glass coverslip. m) seal topside with multilayer microfluidics chip. n) invert chip for actual use, note the side of gold pad layer that was deposited down on the original nitride surface is now face up for cell attachment.

The silicon nitride membrane process starts with a 4-inch wafer with 300nm of commercially grown LPCVD silicon nitride ($\sim 150\text{MPa}$ internal stress), see Appendix 3 for detailed process instructions. In the first step, gold alignment marks are patterned using photo lithography and deposited using electron beam evaporation and liftoff (Figure 17b). In the second step, the gold pad layer, which defines cell attachment points, is patterned by electron beam lithography and deposited using electron beam evaporation and liftoff (Figure 17c). It is important to realize that when the silicon nitride is removed, the side of the pad and beam that is toward the nitride will become the top of the beam where the cells will attach (Figure 17n). Thus, the adhesion layer beneath the gold pads must be chosen so that it will be removed by the hot HF release etch; I have had success with both titanium and the organic compound mercapto-propyl-trimethoxy-silane (MPTS) [127]. In the third step, the first polymer layer is blanket deposited to form a continuous layer across the wafer (Figure 17d). The blanket deposition process depends on the polymer being deposited; SU-8 is spin deposited, soft baked, flood exposed, baked again, developed and hard baked; polyimide is spin deposited and hard baked; Parylene is vapor deposited. In the fourth step, the gold piezoresistor is patterned with electron beam lithography and deposited with electron beam evaporation and liftoff (Figure 17e). AP300 and chrome are used to guarantee strong adhesion between the 500\AA thick gold wire and the polymer layer. In the fifth step, a second polymer layer is deposited (Figure 17f). In the sixth step, the two polymer layers are patterned to define the beams and cell bridge (Figure 17g). A titanium etch mask is patterned using electron beam lithography and deposited using electron beam evaporation and liftoff. The polymer is etched using an oxygen plasma, which quickly etches the polymer but does not etch the titanium etch mask nor the underlying silicon nitride. The etch mask is removed using a short buffered HF etch (Figure 17h). In the seventh step, the 500nm thick gold conductor metal is patterned using photo lithography with a bi-layer resist process and deposited using electron beam evaporation and liftoff (Figure 17i). A brief $\text{CF}_4\text{-O}_2$ plasma immediately before loading into the evaporator and a chrome adhesion layer are necessary for good adhesion between the gold and silicon nitride. In the eighth step, windows are opened in the nitride on the backside of the wafer using photo lithography with backside alignment to pattern the windows and a

CF₄-O₂ plasma to etch through the nitride. A potassium hydroxide (KOH) solution is used to etch through the silicon wafer thus opening silicon nitride membranes beneath the polymer devices, in the ninth step (Figure 17j). During the KOH etch the wafer is held in a special holder in order to protect the polymer devices which will be damaged if exposed to the KOH. The tenth step is the hybrid release etch which I described earlier: first a CF₄-O₂ plasma is used to carefully thin the nitride membrane down to a couple 10's of nanometers, then a dilute (0.1%), hot (80C) HF etch is used to selectively remove the remaining nitride and pad adhesion layer without damaging the polymer devices or gold metal layers (Figure 15 and Figure 17k). After the release etch, the wafers are dried using a critical point drier. Once dry, the wafers are diced and attached to PDMS coated glass cover slips to seal the backside of the device while enabling air bubble removal through the PDMS and high resolution microscopy through the glass (Figure 17l). Microfluidics are attached on the device side of the wafer to completely encapsulate the NEMS force sensors (Figure 17m and Figure 18).

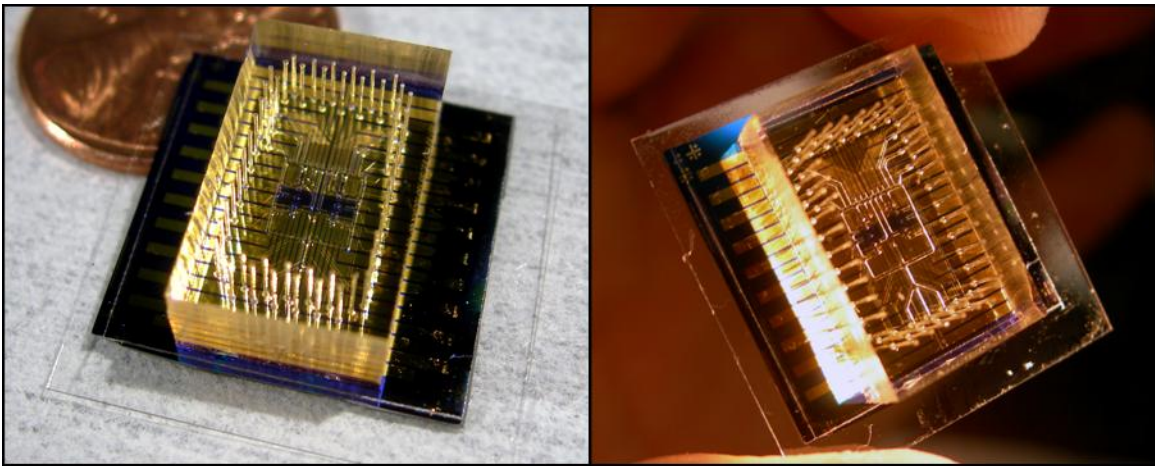


Figure 18. Microfluidics encapsulated NEMS force sensor chips.

I have had the most success fabricating force sensors at high yields using SU-8 3000 series, the lower Young's modulus SU-8 formulation, Figure 8 and Figure 19. I have also fabricated force sensors using polyimide; however, I have had problems with particulates in the polyimide films causing defects. A simple filtration process should fix this (I filter the SU-8 as well) and is worth pursuing. Renaud Richard

fabricated beams from Parylene using my silicon nitride process. Parylene is an appealing material in part because it is biocompatible but also because the vapor deposition method should result in very low internal stress. Unfortunately, it is very difficult to control the thickness of the Parylene layers on the nanometer scale using the equipment available to us. I have focused on SU-8 because of the ease of fabrication and low Young's modulus of the 3000 series, but further work with the polyimide and Parylene is worth pursuing.

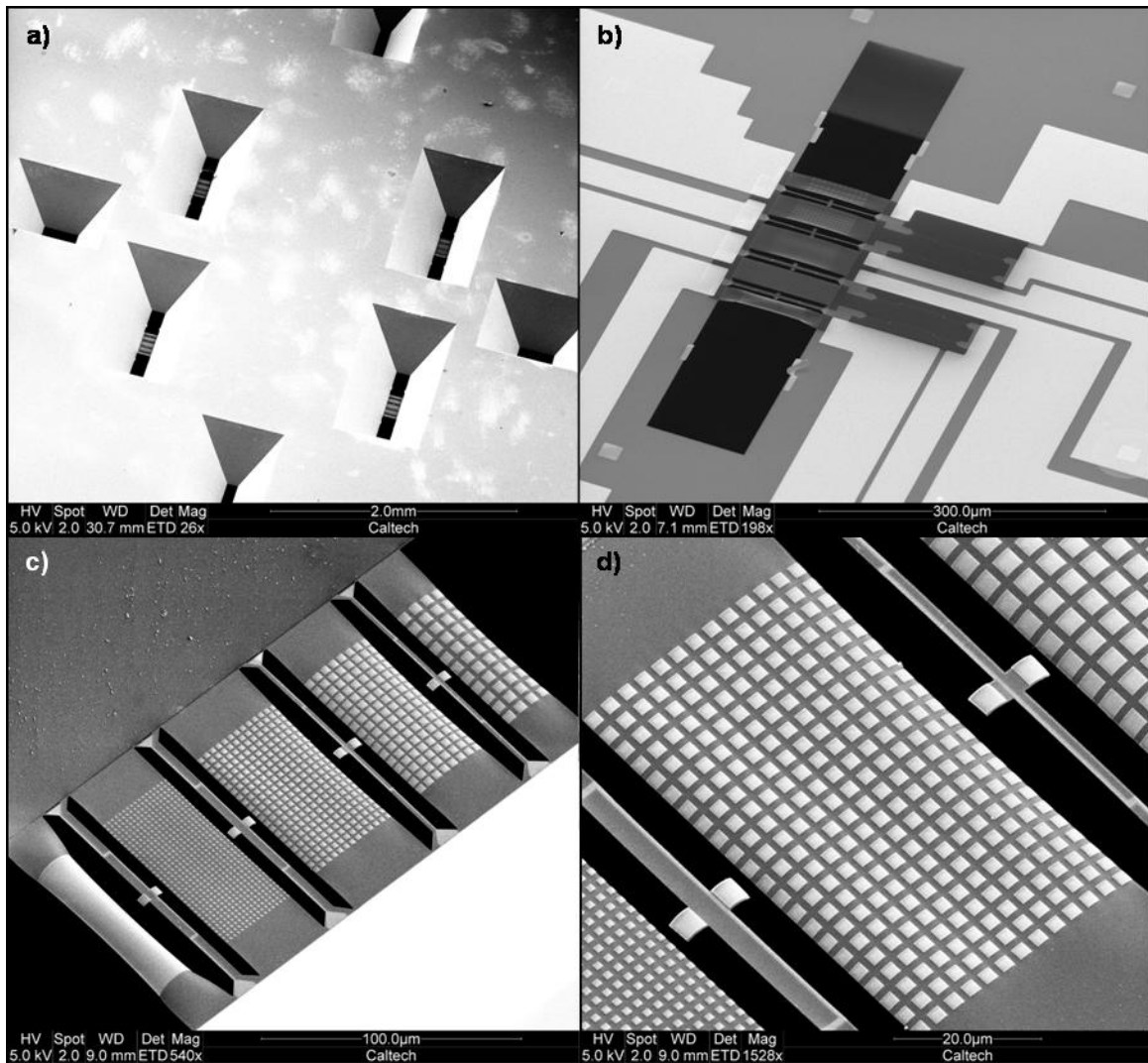


Figure 19. SEM micrographs of finished force sensors at successive magnifications. Image a) shows four KOH etched cell chambers with force sensors at the bottom and four KOH etched viewing ports for monitoring the microfluidics. Image B) shows a single trench and pair of force sensors from the front of the wafer. Images c) and d) show the devices from cell attachment side. These particular devices were fabricated in part to test various pad geometries for reducing curling of the cell bridge.

I have calibrated the transducer responsivity, equation 10, of the force sensors for a number of beams by applying known forces with a glass microneedle that is attached to a piezoelectric actuator; see Figure 21. I first measure the glass microneedle's spring constant with an AFM. Unfortunately, there is a wide spread in the measured spring constant for a given glass microneedle. I suspect that this is because the glass microneedles are not actually round and roll slightly during the calibration process. Regardless, the uncertainty in the microneedle spring constant is high and this uncertainty leads to a large uncertainty in my calibrated transducer responsivity. Within the uncertainty, the transducer responsivity calibrations agree with the finite element simulations. The calibration process is rather cumbersome, so given the agreement between the microneedle measurements and the finite element simulations, I use the finite element simulations to estimate the transducer responsivity for most beams.

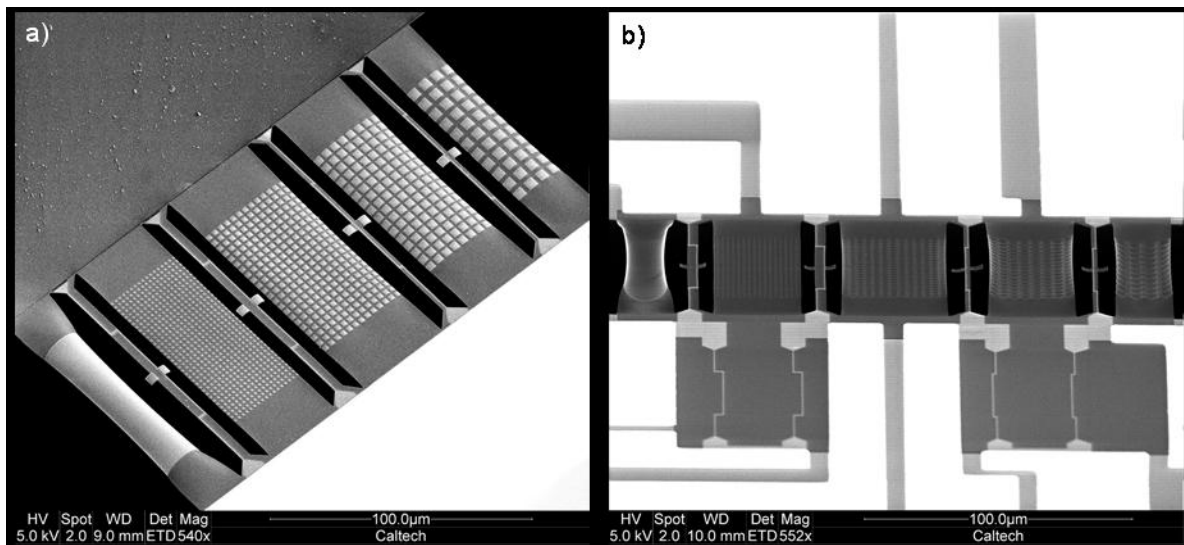


Figure 20. Two scanning electron micrographs of cell bridges patterned with arrays of different sized cell pads from the top (a) and bottom (b). The curling of the cell bridge with continuous gold (far left) and larger pads (far right) is clear. The pad arrays from the left to right are 1) continuous, 2) $1\mu\text{m}$ pad, $2\mu\text{m}$ pitch, 3) $2\mu\text{m}$ pad, $3.15\mu\text{m}$ pitch, 4) $3\mu\text{m}$ pad, $4.25\mu\text{m}$ pitch, 5) $4\mu\text{m}$ pad, $6\mu\text{m}$ pitch.

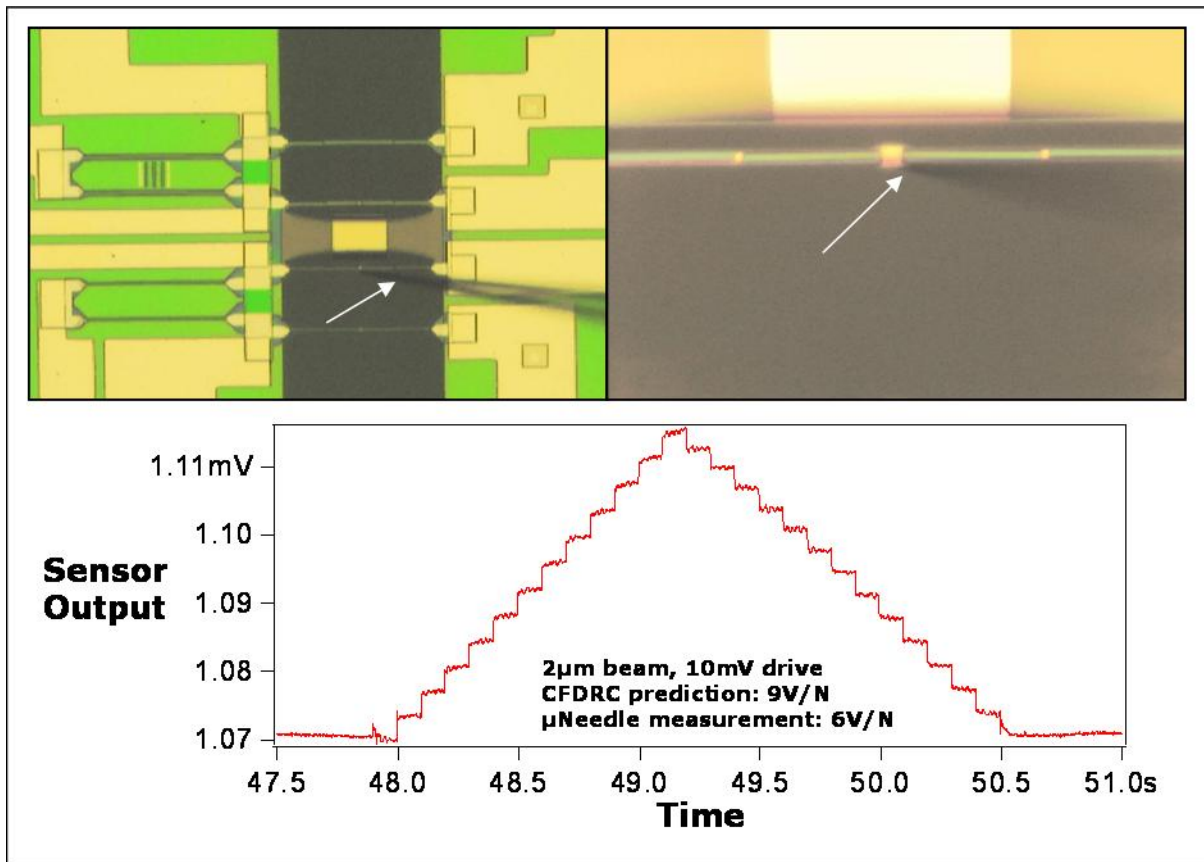


Figure 21. Microneedle calibration of NEMS force sensor. Images at top show a microneedle in contact with a $2\mu\text{m}$ beam. The needle is hard to make out because it is coming from above the focal plane; it is the fuzzy black point entering from the right side each image. The measurements are in good agreement with theory given the uncertainty in the microneedle's spring constant.

3.4 Microfluidics

I use a four layer PDMS microfluidics process adapted from work by Carl Hansen in the Quake Group [128]. Quake microfluidics technology has been well documented [32, 33], but I will recap briefly. Polydimethyl-siloxane (PDMS) is a two-part silicone based elastomer: a base and a curing agent whose components undergo a hydrosylation reaction upon cross-linking. The base consists of dimethylsiloxane oligamers with vinyl-terminated end groups, platinum catalyst, and silica filler. The curing agent consists of a cross-linking agent (dimethylmethylhydrogen siloxane) and an inhibitor (tetramethyl tetravinyl cyclotetrasiloxane) [129]. When the two parts are mixed, cross-linking occurs when the vinyl and silicon

hydride groups undergo a hydrosilylation reaction to form a Si-C bond. The cross-linking reaction occurs at room temperature but can be accelerated by heating; we typically bake at 80C which is compatible with polystyrene Petri dishes. The microfluidics channels and valves are fabricated by molding multiple layers of PDMS over photo lithographically fabricated molds. Alternating layers of PDMS are fabricated having either excess curing agent or excess base agent, partially curing each piece, bringing the two pieces together and then curing the complete assembly. This ability to stack and cure together layers of PDMS is critical to enabling complex microfluidics. A second critical characteristic of PDMS is that it is gas permeable, particularly so for oxygen, nitrogen and carbon dioxide which have diffusivities through PDMS of $34 \times 10^6 \text{cm}^2/\text{s}$, $34 \times 10^6 \text{cm}^2/\text{s}$ and $22 \times 10^6 \text{cm}^2/\text{s}$ respectively [130]; this is necessary for removing air bubbles from fluid channels and for keeping cells alive with fresh oxygen and carbon dioxide within PDMS channels.

The PDMS formulation which I use, RTV-615 from Momentive Materials (formerly GE Silicones), will “fully” cure when the base and curing agent are mixed at a 10:1 ratio and given sufficient time for the reactions to complete (seven days at room temperature, 36 hours at 80C). Another common formulation of PDMS is Corning’s Sylgard 184, which is also based upon a 10:1 base to curing agent ratio. RTV 615 performs better with respect to the layer bonding necessary for fabricating multilayer microfluidics, whereas Sylgard is chemically more stable and consistent from batch to batch. The FDA has approved PDMS as a food handling material [131] and some groups have succeeded in culturing cells in simply cured PDMS for long periods of time. However, there are also reports indicating that PDMS can interfere with cell culture. The Whitesides group has managed to extract roughly 5% by weight of un-cross-linked PDMS oligomers from fully cured PDMS [132]. The Beebe group notes stabilized PDMS surfaces after baking for two weeks at 100C [133]. Other groups have reported improved cell culture on PDMS after treating the PDMS with boiling water – the heat and water vapor help drive the hydrosilylation cross-linking reaction to further completion [134] – or after treating the PDMS to extensive solvent based extraction procedures that remove the un-cross-linked oligomers [135, 136]. In

further support of these conclusions, the Hansen group has observed cell culture results that vary from batch to batch of RTV 615 [137]. I expect that complications from uncross-linked PDMS oligomers will be more severe in multilayer microfluidics because the layers that make up the cell chambers are mixed with excess quantities of the base material. To my embarrassment, these issues have only recently come to my attention when it became clear to me that out-gassing from fully cured PDMS was corrupting my surface chemistry protocols, which I will discuss in section 3.5. I also suspect that the uncross-linked oligomers are poisoning my tissue culture. At the time of writing, I have not been able to check this hypothesis, but it is at the top of my to do list once this thesis writing business is finished.

My microfluidics process is moderately complex and includes a fair amount of functionality (Figure 22 and Appendices 4 and 5). The top layer in the chip is the “incubator layer.” It includes a set of inter-digitated dead end lines that span the entire area of the chip, are filled with water and kept under pressure to ensure that the PDMS is saturated with water vapor and the chip will not suffer from osmolality shifts due to evaporation, which can be a significant problem even in humidified incubators [138]. The incubator layer also includes a through line that snakes between the inter-digitated dead end lines; this line can be used to flow gas through the chip. In particular, I have tested flowing CO₂ mixed air through the chip. The incubator layer mold is fabricated using SU-8 with a single lithography step. The second layer is the “flow layer.” It includes vertical hole punches that connect flow channels on the chip with external tubing for both the 12 inlet and the 3 outlet lines (outlets can clog, hence the redundancy). The 12 inlet lines are divided between 6 large diameter lines ($\sim 6000\mu\text{m}^2$ cross sectional area) for flowing cells and fast flowing fluids and 6 small diameter and large fluidic resistance lines ($\sim 140\mu\text{m}^2$ cross sectional area) for slow flowing fluids past cells without subjecting the cells to shear forces nor the force sensors to mechanical forces; see Table 6. The flow layer includes a pattern of flow lines that individually access each of the four device chambers on the chip through vertical vias. Four lithography steps are required to fabricate the flow molds: one metal alignment mark layer, 1 SU-8 layer to define the high resistance flow lines, 1 AZ50 layer to define the large diameter channels and valve regions and another SU-8 layer to

define the vertical via regions. The third PDMS layer is the “control layer” which defines thin PDMS membranes that are deflected upward to form the valves that control flow through the flow layer. The control layer also has vertical hole punches that connect to external computer controlled pneumatic lines and vertical vias that pass the flow channels down toward the device below. The control layer mold also requires four lithography layers: one metal alignment mark layer, an SU-8 layer to connect the hole punches to the valves, another SU-8 layer to define the valve membranes and a third SU-8 layer to define the vertical connections between the flow layer and the device. The fourth PDMS layer is the “base layer” which seals the bottom of the high pressure control lines and attaches to the NEMS chip. The base layer includes vertical flow channels that connect to the flow layer through the control layer and horizontal channels over which the NEMS devices are suspended. The base layer molds require three photo lithography steps: a metal alignment mark layer, an SU-8 layer to define the horizontal channels and a second SU-8 layer to define the vertical channels.

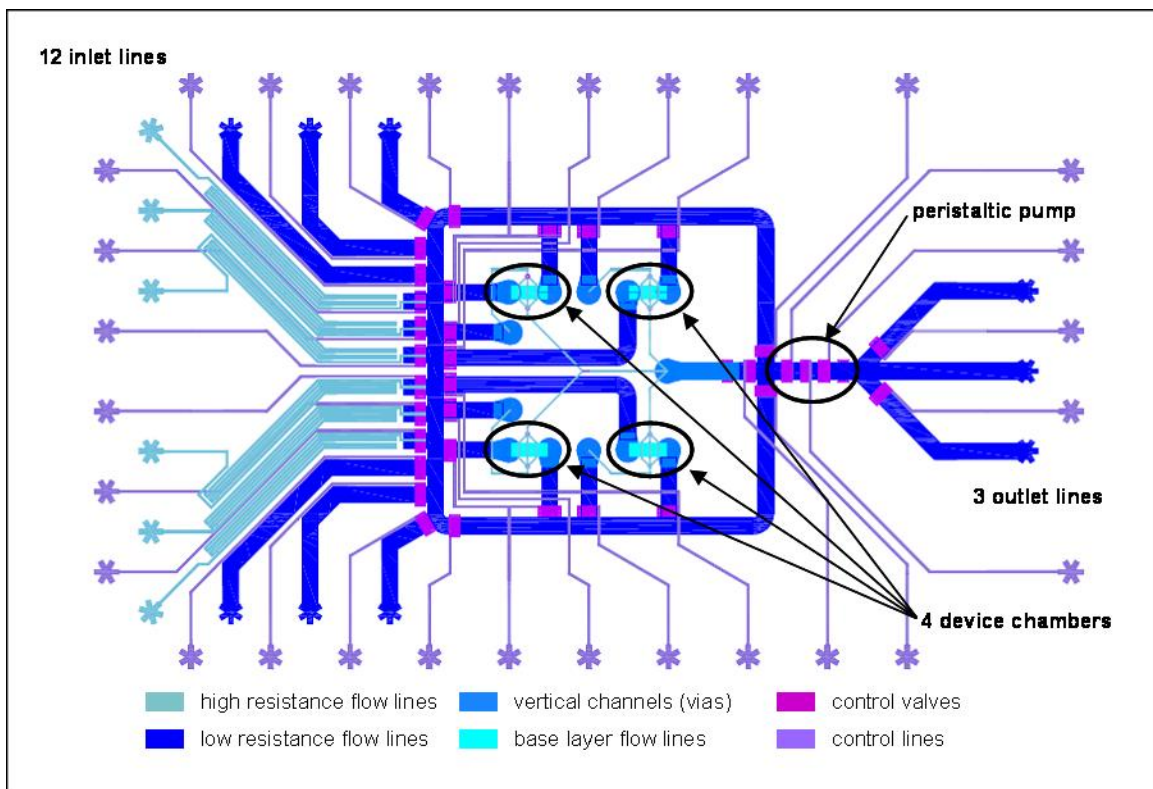


Figure 22. Diagram of multilayer microfluidics chip. Chip includes 12 inlet lines, 6 low resistance lines for loading cells and fast flow fluids and 6 high resistance lines for passing reagents over cells with minimal

sheer forces. 3 outlet lines provide redundancy against clogs. There is a peristaltic pump for precise manipulations of small volumes. Each of the 4 device chambers can be individually accessed and bypass channels exist for rinsing. Incubator layer is omitted for clarity.

The design which I presently use includes these 15 fluid input/output lines and 40 computer controlled pneumatic lines to drive the valves packed into a 160mm² footprint. There is a significant amount of complexity in this microfluidics design, but I fabricate microfluidics chips at very high yields (>90%) and they enable significant functionality. The microfluidics themselves are critical for confining the available acoustic modes within the fluid chamber to high frequencies that do not interfere with my measurement process [28]. The microfluidics are also critical for delivering cells directly to the force sensors; this is a departure from the typical array nature of most biology experiments. Microfluidics are further necessary to enable precise pharmacological perturbation of the cell when it is on the force sensor. With the microfluidics I can precisely control the media flowing past the cell. My microfluidics are computer controlled through the same Igor graphical user interface (GUI) that I wrote to control the image acquisition, force data acquisition and data analysis. In addition to basic valve actuation, the GUI includes a user-friendly interface for easily creating custom sequences and fluidic programs for automating surface chemistry protocols, tissue culture protocols, cleaning protocols, etc. This is useful for standardizing both tissue culture and cell perturbation protocols as well as optimizing time to increase throughput (e.g., cleaning and surface chemistry protocols can be run unattended at night).

The channel size and volumetric flow velocity determine a number of key parameters within the microfluidic channels. The large flow channels are critical for loading cells without clogging and further enable high flow rates for quick rinsing. However, the high flow rates apply strong shear forces to the cells and mechanically perturb the force sensors. The small diameter channels address this issue. The peristaltic pump can be used with either type of flow channel when controlled manipulations of small volumes are necessary. Table 6 lists the fluidic resistance, volumetric and linear flow velocities at 2 PSI, shear force at surface, Reynolds number and Péclet number for a cell and a protein in the cell chamber [139]. Shear forces from fluid flow have been shown to mediate cell shape, function and gene expression

in numerous studies [51, 140, 141]. The slow flow channels were designed to reduce the shear forces in the cell chamber well below the levels typically used to drive cell reorganization on the eight hour time scale (~ 10 dyn/cm²). The Reynolds number is the ratio of inertial forces to viscous forces; as with most microfluidics systems, the dynamics in the cell chamber are in the zero Reynolds number limit where viscous forces dominate [142]. The Péclet number is the ratio of flow driven transport to diffusion driven transport and thus is dependent upon the molecular diffusivity of the particle or reagent in question [143]. In both flow regimes flow driven transport dominates, thus concentration gradients will persist within the cell chamber for long periods of time after a new reagent is introduced. Unfortunately, this means it is very difficult to know the exact local concentration of reagent that is driving a specific response in a cell.

	Fast Flow	Slow Flow
Volumetric flow rate	1 $\mu\text{L/s}$	2 nL/s
Shear force	10 dyn/cm ²	0.02 dyn/cm ²
Reynolds #	3×10^{-6}	1×10^{-8}
Péclet # (Cytochalasin)	3000	6
Péclet # (Fibronectin)	4×10^4	80

Table 6. Key fluid flow parameters inside the cell chamber during fast and slow flow.

3.5 Surface control

Controlling the surfaces of the NEMS devices and the microfluidics channels is critical. Within microfluidics channels the surface to volume ratios are very large – $0.08 \mu\text{m}^{-1}$ in the channels compared with $\sim 5 \times 10^{-4} \mu\text{m}^{-1}$ in a T-25 tissue culture plate – proteins and cells can stick to the surfaces creating cell cultures in unwanted places and potentially depleting media of critical proteins [144]. To prevent nonspecific binding of proteins and cells, I treat the channels with a solution of 1% Pluronic F127 in PBS. Pluronic are a class of nonionic tri-block copolymers composed of a central hydrophobic chain of

polyoxypropylene (poly(propylene oxide)) flanked by two hydrophilic chains of polyoxyethylene (poly(ethylene oxide)) [145]. The hydrophobic polyoxypropylene sticks to the hydrophobic PDMS channels and the hydrophilic polyoxyethylene end groups are presented into the channel and prevent nonspecific binding of cells and proteins [31, 146]. Pluronics is easy to implement and works very well preventing cell attachment in the PDMS channels.

Controlling the surfaces of the NEMS devices is more complex because there must be specific regions where the cells do attach and others where they do not attach. This is critically important for controlling and standardizing the interaction between the cell and the force sensor. Controlling – specifically standardizing – cell-surface interactions has been critical to obtaining regular and statistical data in a number of studies of cell-surface interactions [2, 147-151]. The method that I have chosen to use is inspired by work by John Tan during his time in the Chen group [146]. The basic idea is that the regions where cells are supposed to attach are made hydrophilic using a self-assembled monolayer (SAM), then the remaining hydrophobic regions can be passivated by treating the cell chamber with Pluronics which will stick to the hydrophobic areas but not the hydrophilic areas. Finally, cell attachment to the hydrophilic regions can be further encouraged by treating the cell chamber with a fibronectin (FN) solution; the fibronectin will stick only to the hydrophilic areas because the Pluronics will block attachment elsewhere. Fibronectin is a high-molecular weight ECM glycoprotein that binds to trans-membrane integrins with a well characterized Arginine-Glycine-Aspartic Acid (RGD) sequence [77, 78, 83, 152, 153].

I create differentiation between the cell adhesion and cell blocking regions by patterning gold pads on the cell adhesion regions, which contrasts with surfaces making up the cell blocking regions: principally polymer NEMS but also PDMS and silicon oxide. The gold makes an excellent surface for specifically attaching SAMs using the common thiol chemistry, as long as the gold can be kept clean. This approach contrasts with the stamping method which is the “gold standard” used most commonly in cell surface

studies. The stamping method will not work for my application for a number of reasons. First, the stamp would have to be very carefully aligned to the NEMS devices. I believe 1 micron alignment would be necessary yet difficult to achieve, whereas typical cell-surface studies can be done anywhere on a glass cover slip or elastomer surface; this is due to the same serial/specific location/contact issue that come up again and again when comparing NEMS to optical biology. Second, the stamp must come into physical contact with the NEMS device with a wet (sticky!) surface. I haven't tested this, but I expect that it would likely damage the NEMS devices. Third, the NEMS surfaces that would have to be stamped are at the bottom of a 400 μm deep trench through the silicon wafer, so the stamp would have to be at the end of a very long ($\sim 500\mu\text{m}$), high aspect ratio ($\sim 10:1$) tip. For these reasons, I continue to work with the gold surfaces.

I have tested and refined my surface chemistry protocol using test wafers. I spin deposit and cure a blanket layer of polymer, typically SU-8, but I have verified similar results with Parylene and polyimide, onto a silicon wafer and lithographically pattern gold pads on top of the polymer surface, principally using photo lithography but I have done some electron beam lithography tests. The gold surfaces are treated with either titanium or MPTS to mimic the adhesion layer used in the NEMS fabrication process, then the wafers are treated with the same hot, dilute HF release etch and dried in a critical point drier. I then dice the wafers into small pieces ($\sim 4\text{mm}$ on a side) and place them in 24 well plates and run matrix experiments to test reagent, time, and concentration.

I find that a large range of chemicals and concentrations work in the 24 well plates. Carboxylic acid terminated SAMs work best, but hydroxyl groups also work and poorly assembled (short time) polyethylene-glycol (PEG) terminated SAMs even work. The SAMs can be deposited from either solvent (typically ethanol) or aqueous solution using recipes developed by Christie Canaria of the Fraser group [154]. A wide range of deposition times work for the acid and hydroxyl terminated SAMs but PEG SAMs must be deposited for less than 20 minutes. A wide range of Pluronic 127 concentrations,

0.1% up to 1% by weight in PBS, work well with 20-80 minutes deposition times. A similar range of FN concentrations, 5-50 $\mu\text{g}/\text{mL}$ in PBS, work well with 20 minutes to 4 hour deposition times. I monitor the surface changes by measuring the contact angle and test the results by seeding cells onto the surfaces for 2-3 hours, rinsing to perturb nonspecifically bound cells, fixing and imaging. Representative results are shown in Figure 23.



Figure 23. Surface chemistry petri dish experiments, test pieces with polymer (dark) and gold surfaces (yellow/orange). Image a) shows results of a typical fibronectin only test: cells are spread everywhere. Image b) is from a typical Pluronic only test: almost no cells present and none are spread. Images c) & d) show results from complete surface chemistry process (SAM, Pluronic and fibronectin): cells are well spread on the gold and absent from the polymer.

I have tested some smaller pad substrates as well (Figure 24). This is motivated by the switch to pad arrays in order to prevent curling of the cell bridge (Figure 20). Cells are happiest with small gaps, 1

micron or smaller, between the pads; pad size itself is less critical. I have settled on $1\mu\text{m}$ pads at a $2\mu\text{m}$ pitch because the smaller pads reduce curling in the cell bridge (Figure 20)

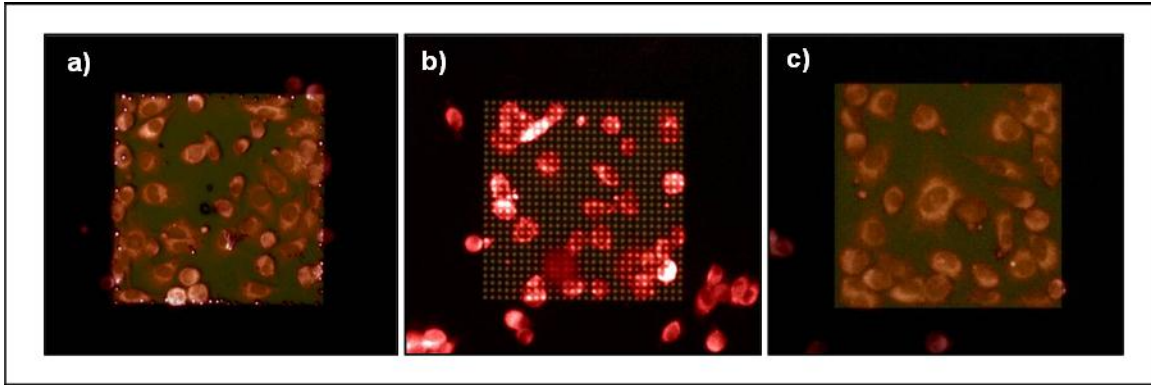


Figure 24. Cell spread on pad array surface chemistry and cell spreading tests. Polymer and gold surfaces with full SAM, Pluronics and FN surface chemistry. Image a) is a continuous gold surface, cells are well spread. Image b) is an array of $3\mu\text{m}$ gold pads on a $6\mu\text{m}$ pitch (copying the geometry used by the Chen group's mPADs [2]), the cells are not well spread. Image c) is an array of $1\mu\text{m}$ gold pads on a $2\mu\text{m}$ pitch, the cells are well spread.

Unfortunately, transferring the surface chemistry process to microfluidics encapsulated devices creates problems. Initial results failed completely – cells were blocked everywhere. This is particularly bad because it ruins the device for good. A further complication is that my current device design has only four cell chambers per chip, so only four conditions can be compared at once and even then without a redundancy check, this makes it all but impossible to run the kind of matrix experiments that I ran in the 24 well plates to develop the process to begin with. However, by following the contact angle through the process, I have identified PDMS out gassing during the adhesion bake as the source of the problem (Table 7). When baked at 55C PDMS out gasses something that is blocking the gold surface to SAM deposition. I have experimented with alternative curing strategies, using UV and room temperature curing epoxies. The results are an improvement, but not sufficiently good: even at room temperature the surfaces are dirtied (Figure 25). I suspect that given the large surface to volume ratios within the packaged NEMS devices, even at room temperature the PDMS is out gassing enough contaminants to degrade the surface chemistry process.

PDMS bake temperature	Contact angle before bake	Contact angle after bake	Contact angle after SAM deposition
Control	84°	84°	26°
20°C	84°	90°	29°
55°C	84°	100°	57°
80°C	84°	103°	100°

Table 7. Contact angle tests illustrate PDMS out gassing contaminates gold surfaces. In the data shown above, gold surfaces are held in close proximity to thin layers of “fully” cured RTV 615 and baked for 24 hours to test for contamination of the gold by PDMS. The slight increase in contact angle after the bake (center column) indicates a contaminant may have been deposited. The last column indicates success (green) or failure (red and blue) to make the gold surface hydrophilic by depositing a COOH-Thiol SAM. The gold surfaces exposed to elevated bake temperatures and thus elevated PDMS out gassing are clearly contaminated.

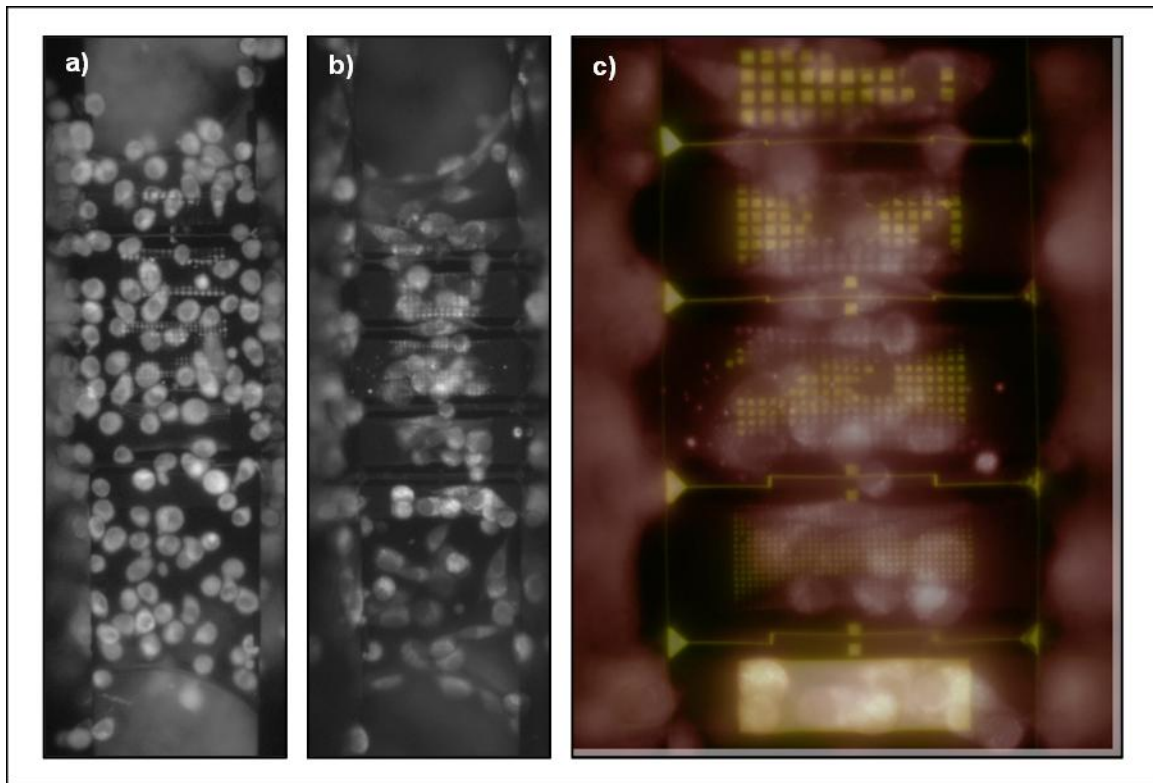


Figure 25. Best surface chemistry results in a microfluidics encapsulated device to date. The PDMS microfluidics was attached without a bake step to minimize out gassing from the PDMS. The results are a noticeable but insufficient improvement from baked devices. Image a) shows the cells 10 minutes after loading, before spreading. Images b) & c) show the cells two hours after loading; cells have clearly migrated from the polymer regions to the gold regions; however, the cells are still attached to many polymer regions. Greater selectivity is needed to be standardize the cell-force sensor interface.

As I mentioned previously in section 3.4, even fully cured PDMS contains a significant quantity of unpolymerized monomers which can be removed by solvent dilution/extraction processes [132, 136]. It is likely that these monomers are the source of the contamination that is blocking the gold surface from the SAM assembly. Tests to verify this and to confirm that PDMS cleaning by either a diethyl ether or xylenes extraction process will fix my surface chemistry problems are underway at the time of writing.

Electrocleaning of the gold is also a possibility. Early in my career at Caltech, Christie Canaria and I developed SAM deposition techniques for gold pads in microfluidics. We found that it was necessary to electrically clean the gold surfaces before SAMs would assemble; see results in Figure 26. At the time we assumed that the contamination on the gold pads was just from ambient dirt, etc. but in light of the data in Table 7, I suspect it also included a lot of PDMS contamination. The problem with applying this method to my system is electrically contacting all of the pads. Running a wire to each pad on the ledge would increase some stress and curling within the ledge, but would be difficult to implement. Contacting the pad on the beam is more difficult. A second wire to directly contact the pad will stiffen the beam, which will reduce sensitivity. However, the pad is nominally capacitively coupled to the PZR ($\sim 1 \times 10^{-16}$ F). I think, but am not certain, that this would work with the electro cleaning. The pad could be connected directly to the PZR wire, but this would require an additional electron beam lithography and etch step.

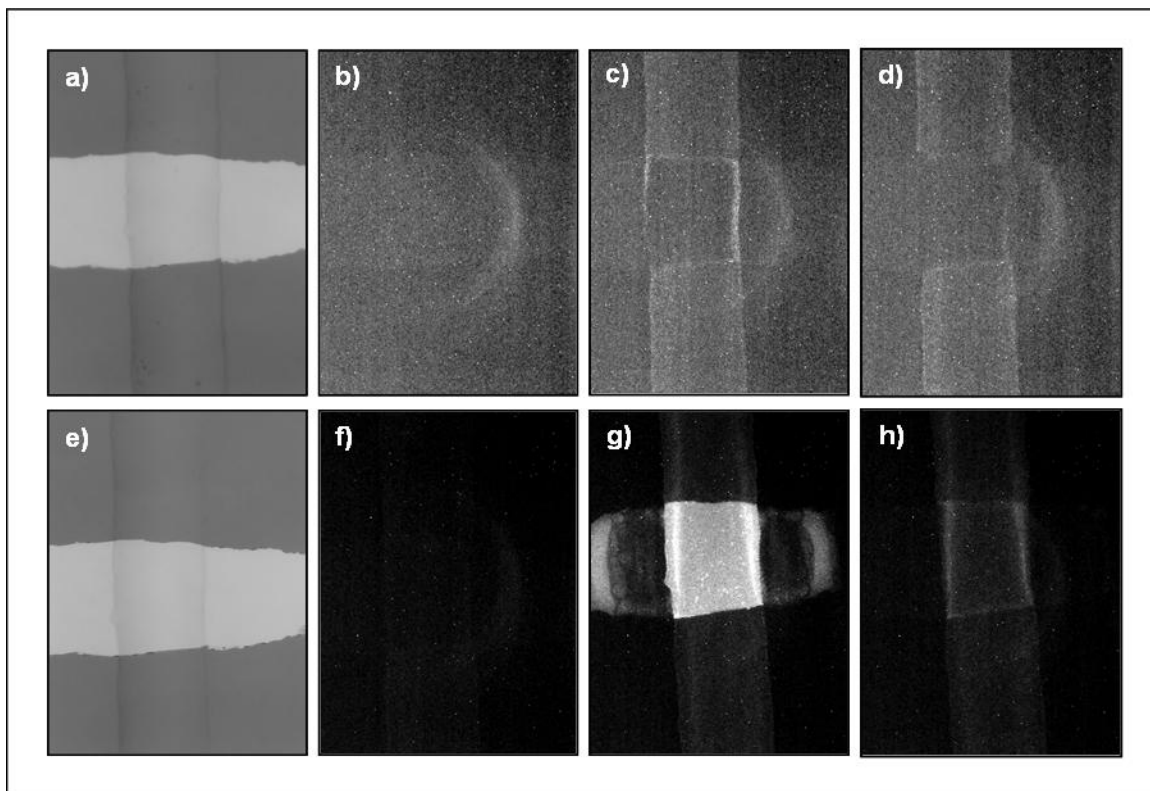


Figure 26. Electro cleaning and SAM assembly on gold electrodes in microfluidics chips. Image sequence a-d) shows the first attempt to place a fluorescently labeled SAM on the gold electrode: image a) is a bright field image showing the electrode and microfluidic channel, images b-d) are fluorescent images taken before SAM deposition (b), after SAM deposition showing little to no SAM has been deposited (c) and after electro cleaning the electrode (d). Image sequence e-h) show the second attempt to deposit a SAM on the same electrode: image e) is the bright field image showing the electrode and microfluidic channel, images f-h) are fluorescent images taken before SAM deposition (f), after SAM deposition showing bright fluorescent signal indicating SAM has been deposited (g) and after electro cleaning the electrode (d). The electro clean that occurs at the end of the first sequence is necessary for the successful SAM deposition shown in the second sequence.

Could I replace the PDMS with a different material? There are good alternatives for making simple passive channels such as Parylene and Ordyl [155], but there are not good alternatives for making complex microfluidics with valves. The Tai group has a method for making Parylene valves, but the fabrication process is not practical [156, 157] and the gas impermeability of Parylene significantly complicates cell culture in Parylene channels. Although there are groups that have achieved on chip cell culture in simple (valveless) microfluidics, complex microfluidics enable a number of functions that are critical for SCPFM and NEMS tools for biology in general: addressing multiple devices, cell positioning over devices, and pharmacological perturbation. For these reasons, I am not willing to give up on PDMS

as a microfluidics material; instead I will focus on solving the surface chemistry problem within PDMS based microfluidics.

3.6 Sample holder & incubator

I have built and designed a microscope-mounted-incubator-and-sample-holder, the “sample holder” for short, that brings all of the disparate technologies involved together with the NEMS chip (Figure 27). The sample holder is made of brass to provide electrical shielding and a large heat capacity to buffer against temperature fluctuations. Incubator capabilities are added to the sample holder through temperature and CO₂ sensors that feedback to a LiveCell control unit which circulates heated, CO₂ conditioned air through the sample holder. The sample holder has 40 electrical feed-throughs that connect to circuit boards with integrated pre-amplifiers built around Texas Instrument’s INA103 instrumentation amplifier. The circuit boards connect to the NEMS chip via pogo-pins held in a Plexiglas plate. There are 60 microfluidic line feed-throughs into the sample holder and a window where the NEMS chip sits. The sample holder mounts on an upright microscope thus enabling fluorescence microscopy, simultaneous fluidic operations, and high resolution force measurement with the NEMS chips in an incubator.

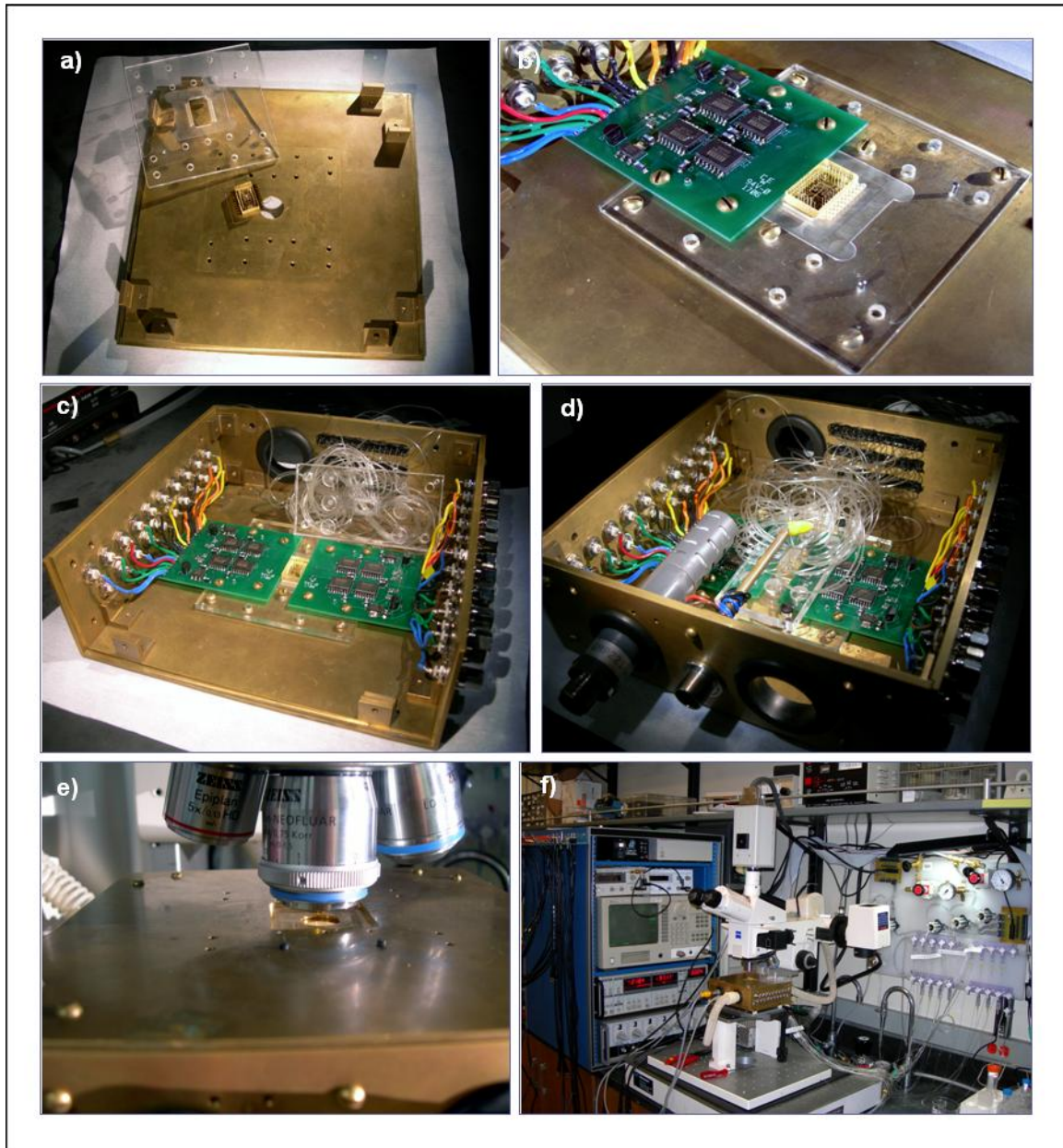


Figure 27. Images showing assembly of microscope mounted incubator and sample holder. Including pogo-pin contacts (a), integrated pre-amplifiers (b), microfluidic tubing feedthrough and strain relief (c), temperature and CO₂ sensors (d), window for optical access (e) and the complete system on the microscope with electronics and microfluidics control board (f).

3.6 Tissue culture in microfluidics

Despite the incubation capabilities of the sample holder – cells grow very well in T-25 plates within the sample holder – I have not succeeded in successfully culturing cells, even robust lines like Chinese

Hampster Ovary cells (CHO) and NIH-3T3 fibroblasts, within microfluidics chips in the sample holder. When seeded in conditioned media, cells will spread and appear happy for 6-12 hours, but they do not divide, and after 12 hours or so, they will have stopped moving, lost most shape and lost membrane integrity. Other research groups have solved this problem and successfully cultured cell in microfluidics chips on microscopes, so I should be able to solve this problem.

Here I briefly outline some of the groups that have cultured mammalian cells in microfluidics. The Quake group has a particularly impressive fully-automated microscope mounted microfluidic cell culture system containing 96 individually addressable cell culture chambers, a chaotic mixer and a peristaltic pump for precise fluid manipulations [31]. Of particular note, the Quake group has successfully cultured many cell types indefinitely, including delicate stem cell lines, in RTV 615 PDMS without solvent extraction [158], which would seem to strongly imply the solvent extraction is not necessary. However, growth curves that the Quake group has published are a bit weaker than is expected. The Quake group exchanges media with controlled, periodic injections of fresh media into the cell culture chambers. It seems likely that the Quake group is exchanging media at a higher than optimal rate, from a growth factor perspective, in order to sufficiently remove unpolymerized PDMS. The Quake group also reports significant variations from chamber to chamber on their chips [158]; this could be stochastic variations that are endemic to biology or could be due to PDMS contamination. The Thorsen group also uses periodic media exchanges to culture BALB/3T3, HeLa and bovine endothelial cells in Sylgard chambers [159]. The Ozinsky group has cultured macrophages indefinitely in solvent extracted RTV 615 PDMS using continuous parallel flow media exchange [136]. The Lee group, Whitesides group and Jayaraman group all use direct continuous flow to culture mammalian cells in microfluidics [160-162]. The Tseng group has successfully cultured NIH-3T3, B16 and HeLa cells for up to 8 days in Sylgard 184 PDMS using a recirculation reservoir design [163, 164]. The Jeon and Beebe groups have cultured cells, including oligodendrocytes, in passive Sylgard chips [165, 166]. Each of these groups has arrived at successful cell culture in microfluidics chips in different, sometimes conflicting ways using systems that

are not only divergent and difficult to compare, but also not fully understood by their users. As such, a great deal of black magic still exists in this nascent field. However, there is a general support for the conclusion that RTV 615 PDMS, particularly without solvent extraction, is not optimal.

One significant problem with my current system is that each chip has only four cell chambers, so I can only run four experiments at a single time under identical incubator conditions. This is a logistical difficulty because it takes a full day to set up a chip, and I believe it is best to let the chip equilibrate temp and CO₂ overnight. More importantly, it is insufficient to deal with basic fluctuations and variations in biology. By point of reference, the Quake group has a microfluidics chip which they use for cell biology studies with 96 cell chambers. When running an experiment the Quake group keeps at least eight different chambers at each set of experimental conditions in order to combat the variations that they see from chamber to chamber. In contrast, I have only four chambers to work with in the first place. This makes it very difficult for me to do the large matrix experiments necessary to test and debug the many different conditions that might affect both cell culture and surface chemistry protocols within my chip.

Nevertheless, I have done my best to test and control for a wide variety of possible problems which I will briefly outline here.

3.6.1 Temperature

Optimal growth for most mammalian cells occurs at 37C; however, robust cell lines such as NIH-3T3's will still grow over a range from 34C up to about 39C. The LiveCell control unit provides temperature sensing and feedback to my sample holder. I have further calibrated the temperature within the microfluidics chip by embedding a thermocouple within the PDMS chip, within about 1mm of the cell chambers, in order to monitor the temperature. Within the accuracy of the thermocouple, 1C, the LiveCell unit is able to hold the microfluidics chip within my sample holder at a very stable 37C.

3.6.2 Carbon dioxide

Carbon dioxide conditioned air is critical for mammalian cell growth. 5% CO₂ is typical, but the range can be anywhere from 2-10% depending on the cell type and media. CO₂ buffers the media against the excess build up of carbonic acid, a by-product of cell metabolism [167]. The LiveCell control unit provides CO₂ sensing and feedback to keep the atmosphere within the chamber at the specified CO₂ concentration; I typically work at 5%, but have tested 2% and 8%. The percentages are measured within the sample holder and not the cell chambers within the microfluidics. However, CO₂ diffuses quite quickly through PDMS [130], so I believe it is safe to assume that the CO₂ concentration will equilibrate through the microfluidics chip. At the suggestion of the Quake group, the flow lines are pressurized using 5% CO₂ to ensure that the flowing of liquids does not deplete the microfluidics chip of CO₂. I have tested buffering against pH drift by growing cells in 25mM HEPES, rather than the 10mM in my regular growth media, and a HEPES free formulation. I have also tested flowing 2%, 5% and 10% CO₂ through the incubator layer of the microfluidics chip in order to ensure CO₂ is present close to the cell chambers. None of these efforts cause a significant improvement or degradation in cell culture. Though, I haven't thermally tested 0% CO₂.

3.6.3 Feeding/media exchange

It is critical that cells periodically receive fresh media both to bring fresh nutrients to the cells and, more importantly, to remove the cell's waste, otherwise the cells will essentially choke on their own excrement [168]. Some research groups use continuous slow flow to exchange media, others periodically displace some of the media in the chamber. I have tried both techniques by using slow flow lines, fast flow lines and the peristaltic pump to regulate media flow in various ways. It is definitely possible to significantly degrade cell culture by flowing too quickly; this is possibly due to shear forces perturbing the cells or due

to the too fast removal of growth factors necessary to keep the cells happy. However, various slow flow settings have not shown an appreciable improvement from no flow.

3.6.4 Materials

Typical mammalian tissue culture is done in polystyrene culture dishes. The groups that have successfully cultured cells in microscope mounted microfluidics chips use chips that are entirely PDMS. My NEMS chips, in contrast, contain a host of different materials that potentially complicate the tissue culture. In addition to PDMS, the chips contain silicon, silicon nitride, gold, chrome and of course the polymer used to make the NEMS devices: SU-8, Parylene or polyimide. As I mentioned earlier the low stress SU-8 in the all polymer design clearly poisoned the cells very quickly; all of the tissue culture experiments that I am discussing in this section were done with the nitride membrane chips that have no low stress SU-8 and very little polymer in general – the volume-to-volume ratio of polymer to fluid in the cell chamber has been reduced 8 orders of magnitude from the all-polymer process (see discussion in section 3.3.3).

First, it is very easy for me to run negative controls by leaving the NEMS chip out and simply mounting the microfluidics on a glass cover slip. This does not fix or improve my cell culture results. I have also run controls using chips without any processing except the KOH etch and membrane removal – i.e., chips without gold, chrome or polymer – and chips without the polymer but with gold and chrome. Neither of these controls result in improved tissue culture. Lastly, I have tested the compatibility of the cells with SU-8, Parylene and polyimide by spinning the polymers onto glass cover slips and growing cells on the cover slips in the incubator. Cells grow very well on all of the polymers in the conventional incubator despite the fact that the surface to volume ratios in these tests are $\sim 10\times$ greater than on the NEMS chips.

3.6.5 Cell chamber shape

Due to the KOH etch, the NEMS devices have odd shaped cell chambers. This is potentially bad because the upper corners will be difficult to rinse. I have test chips that replace the large trapezoidal KOH chamber with a simple rectangular chamber ($30\mu\text{m} \times 130\mu\text{m}$ cross section) without noting any difference in cell culture.

3.6.6 Conditioned media

I find that seeding cells in conditioned media is critical for getting initial cell spreading within the microfluidics chips. Dependence on conditioned media is generally indicative of unhealthy tissue culture conditions; the growth factors present in the conditioned media give the cells an adrenaline-like boost. After the initial seeding of the cell, feeding the cells with conditioned versus fresh media does not appear to make a difference.

I condition the media by seeding cells into a T-75 plate; when the plate has reached $\sim 50\%$ confluence, I change the media, and after 24 hours I remove the media, filter through a $0.45\mu\text{m}$ filter to remove any floating cells, aliquot into 1mL vials and freeze at -20C . To use the conditioned media, I defrost a single 1mL aliquot and dilute it in 2mL of fresh media.

3.6.7 Fluorescence microscopy

I am constrained to using fluorescence microscopy to monitor the state of the cells in the NEMS chip because my system is built around an upright microscope that only has a reflected light source. There are two sources of potential damage from the UV light. First is direct damage to molecules in the cell from

the UV light, particularly DNA. The second is the creation of oxygen radicals in the media; for example, HEPES buffer can convert to hydrogen peroxide when exposed to UV light [169]. The typical growth media that I use has 10mM HEPES buffer; however, I have tested media with 25mM and 0mM HEPES buffer and again observe no noticeable difference.

Typically, I stain the cells with Cell Tracker Red (Invitrogen) before loading them into the NEMS chip, but I have also tested fibroblasts with a GFP-Actin transfection and find no noticeable difference. I have a sensitive charge-coupled-device (CCD) camera (Hamamatsu Orca) with a shutter that I use to periodically check on the cells. I am thus able to limit the cell's exposure to UV light to less than 1 second per 2 hours. This is pretty minimal and I don't believe that it should be sufficient to damage the cells.

3.6.7 Tissue culture summary

In summary, I am relatively confident that I have addressed the incubation, fluid handling and media exchange needs, reduced the fluorescence exposure to harmless levels and eliminated all material issues except for PDMS. This is in large part due to a stubborn denial on my part that PDMS could be the problem and supported by a general belief in the field that PDMS is "perfectly biocompatible" [114, 170]. At this point, I have clear data that PDMS is the source of contamination that is fouling my gold surfaces and interfering with the surface chemistry (Table 7). Combined with experiences from various other groups that implicate PDMS as a source of contamination in cell culture, it seems likely to me that PDMS is contaminating my tissue culture. Efforts to test cell culture in solvent extracted PDMS are presently underway (better late than never). I am quite optimistic that solvent extraction cleaning of the PDMS will solve both my surface chemistry problems and my tissue culture problems.

Additionally, I clearly need chips with more chambers so that I can run more complex matrix experiments, thus testing and controlling more variables at once. A new design is in process that will place 16 cell chambers and 32 force sensors on a single chip. I expect these devices to be ready roughly April 2009.

I believe that it would be prudent to take a step back and first duplicate the simpler tissue culture results from other labs. Toward this end, I am supervising a second year graduate student, Paula Popescu, who is working to mimic the Quake group's tissue culture setup using a slightly simplified chip and a manual inverted microscope.

3.7 Recap & future directions

In summary, I have successfully developed a NEMS based tool for measuring forces exerted by adherent cells. The force sensors have near molecular level force sensitivity, Figure 8 and Figure 19: 30pN force resolution at 10ms time resolution and five decades of dynamic range in both force and time, thus enabling near molecular level monitoring of whole cell responses to chemical or mechanical stimuli: force measurements into the 100's of nNs and time measurements that persist for hours. I have developed robust, high yield wafer scale fabrication methods for these devices. My current design presents two force sensors to a given cell and four cell chambers per chip, for a total of eight sensors per chip. I run a 4-inch process with nine chips per wafer and typically three wafers per fabrication run. Typical yields are 75% and the fabrication process takes approximately one month from start to a full batch of microfluidics encapsulated chips. At 75% yield, a one month fabrication run will yield 27 chips with an average of six force sensors per chip, a more than six month supply of chips.

I have developed, built and debugged a workstation and suite of supporting technologies for operating the NEMS force sensors. Included in this workstation is a microscope mounted incubator for tissue

culture, high resolution fluorescence microscopy for monitoring the cells under study, automated microfluidics, and readout electronics. All of which are controlled through a user friendly GUI implemented in Igor that enables automation of all control processes.

There are still critical unresolved issues. Standardizing the cell-force-sensor interaction through surface chemistry and healthy tissue culture within the NEMS chip have not yet been demonstrated. I believe that these two problems, particularly the surface chemistry, are the last remaining hurdles before routine data acquisition will be possible with this tool. I believe that contamination from un-polymerized PDMS monomers is the source of the difficulties that I have had with both these processes and I am optimistic that solvent extraction processes will address this issue. Tests toward that end are underway.

There are additional tool advancements that will be coming online in the next few months. We have received a new microscope from Zeiss that will add transmitted light with oblique optics to the existing reflected fluorescent imaging and a motorized stage and computer controlled imaging. The computer controlled microscope will enable me to scale up the number of cell chambers per chip that I can utilize at once. Toward that end, I have finished a mask set for a new chip design that will place 16 cell chambers and 32 force sensors onto a single 30mm square chip and will be fabricated on 6-inch wafers with 12 chips and 384 force sensors per wafer. I have designed and bread-board tested a decoder circuit for accessing all 32 force sensors and the 160 electrical contacts they require. The new chip design and microscope will require a new sample holder and incubator design that is in progress and will utilize a new LiveCell control unit with added humidity control and improved CO₂ and temperature control. I am optimistic that these workstation improvements coupled with solvent extracted PDMS will make systematic studies of molecular level mechanical responses to mechanical and chemical stimuli in single cells routine.

Chapter 4. Proof of principle

4.1 Basic idea

I have successfully used SCPFM to measure force dynamics from single cells. Figure 28 shows force versus time data from a lamellipodia of an NIH-3T3 fibroblast, shown in the inset of Figure 28, as it is perturbed with Cytochalasin D (CD) and allowed to recover in growth media. The gross structure of the force recovery shown in Figure 28 shows the behavior expected based upon measurements by the Chen group using their mPADs [2]. However, SCPFM acquires data at significantly higher force and time resolution – 200pN and 100ms in this particular measurement – thus opening wide swaths of previously inaccessible molecular-mechanical processes to study at the single cell level.

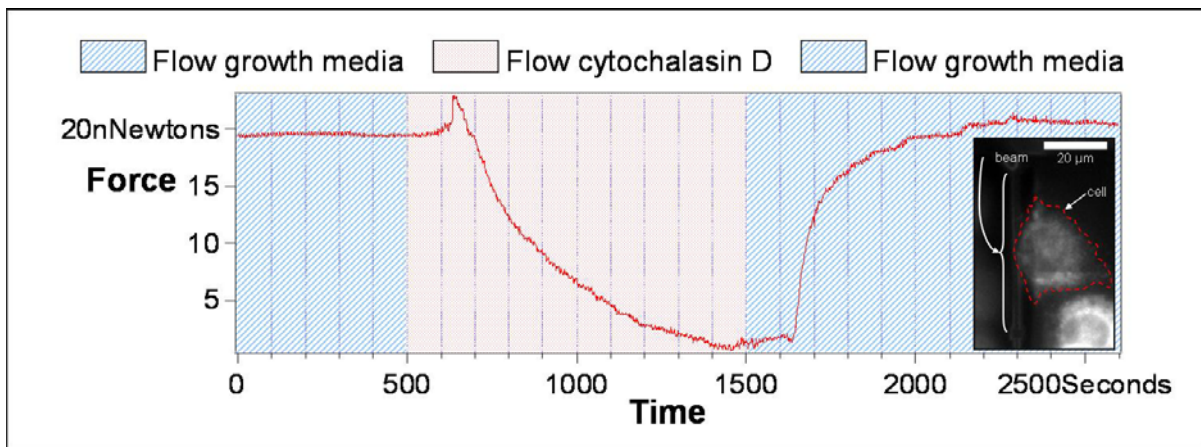


Figure 28. NEMS-enabled single-cell force measurements with unprecedented temporal and force resolution. The plot above shows force versus time data from a contracting and relaxing lamellipodia as the cell, shown inset, is perturbed with Cytochalasin D and allowed to recover in growth media. The force data was acquired with a force resolution of 200pN and a time resolution of 100ms – 25x and 300x, respectively, better than prior state of the art [2].

There are a number of important practical things to note about the data shown in Figure 28. First, all of the surfaces in the cell chamber have been treated with fibronectin to encourage cell spreading and adhesion; there is no Pluronic present and no effort to control the cell's location nor the cell-beam interaction through surface chemistry beyond encouraging general adhesion with the fibronectin. As a

result, there are cells attached all over the cell chamber (not shown) and the particular cell that is attached to the beam, shown in the inset of Figure 28, is not attached to the beam at the center point of the beam, which is its most sensitive spot. Instead, the cell is attached at the zig-zag in the piezoresistor that marks the $\frac{1}{4}$ point along the beam. This is fortunate because it allows me to precisely know the cell attachment point so that I can estimate the transducer responsivity; however, that responsivity is significantly lower than if the cell had grabbed the beam at the mid-point. The transducer responsivity in this data is 37.5 V/N from a 0.5V drive voltage and a 100ms integration time giving a force resolution of 200pN; whereas, had the cell grabbed at the center of the beam, the responsivity would be 190 V/N and the force resolution would be 40pN for the same drive voltage and integration time. Second, the spring constant is quite high due to the off-center pull: 15 N/m; whereas, at the center of the beam the spring constant would be 0.9N/m. 15 N/m is very stiff, a 1nN will result in less than a 1Å displacement, one should not think of a stationary cell deflecting the beam, rather the beam and cell are in tension and the gel nature of the cell plays a significant role in the dynamics [171]. Third, in the data shown the cells are treated to a continuous slow flow that alternates between conditioned media (see section 3.6.6) and a solution of nominally 1 μ M CD in Dulbecco's Modified Eagle Media (DMEM). However, that CD solution had been in storage at 4C for an extended period of time (on the order of ten months) and had likely degraded somewhat. This hypothesis is supported by tests that I have done with various concentrations of CD that show a larger cytoskeleton reorganization at 1 μ M than is evident in this data. Unfortunately, it is impossible to be certain what the actual concentration of CD used in these experiments was. Fourth, I was able to cycle this particular cell with the media-CD-media sequence four consecutive times before exhaustion set in; the cell did not die until I left it overnight (I didn't realize that quality data would turn out to be so hard to come by). The cleanest of the four cycles is shown in Figure 28; however, the data shown is very much representative of the other three cycles. The differences that exist are easily explained by variations in the microfluidics manipulations such as exposing the cell to stagnant media or CD for periods.

4.2 Cytochalasin

Cytochalasin D (CD) was used for the proof of principle experiments, shown in Figure 28, because it is a fast acting and commonly used cell force disruptor. However, CD's mechanism of action is multimodal and, despite many years of study, not fully characterized, which complicates understanding the data. At low concentrations CD appears to disrupt connections between stress fibers and focal adhesions without dismantling the stress fibers [172]; however, the mechanism by which CD interacts with the stress fibers is complicated. The initial picture, laid out nearly 30 years ago, hypothesizes that CD caps actin filaments and detaches them from focal adhesions [173-177]. This model is still in common use [178] despite having been shown to be overly simplistic [179-182]. Specifically, CD does reduce actin filament extension *in vitro*, but not to the irreversible degree hypothesized in early models [183]. Furthermore, CD has been shown to disrupt cortical actin, rather than actin filaments [172], and disconnect the actin meshwork from the leading edge of the cell [184, 185]. *In vitro* studies of high concentrations of CD add more complications to the picture. At high concentrations CD effectively sequesters monomeric actin by hydrolyzing GTP-actin through a multi-step process [180], which ultimately results in dismantling the stress fibers. Additionally, CD induces new sites of actin aggregation that selectively associate with several important regulatory proteins [186]. CD is an effective force disruptor for producing dramatic proof-of-principle force changes in a cell, but it is a poor choice for generating data that is easily understood at the molecular level.

4.3 Comparison with mPADs

The gross structure of the force recovery shown in Figure 28 is of the same magnitude and time scale as similar contraction data obtained by the Chen group using their mPADs [2] shown in Figure 29. The force resolution of the mPADs used in those studies is about 5nN, and the data shown in Figure 29 is an average over measurements on 18 different cells. It is worth noting that in order to get data that could be

compared and averaged, the Chen group had to force the cells into a stable shape. It is very encouraging to see such similar qualitative and quantitative behavior between the two systems.

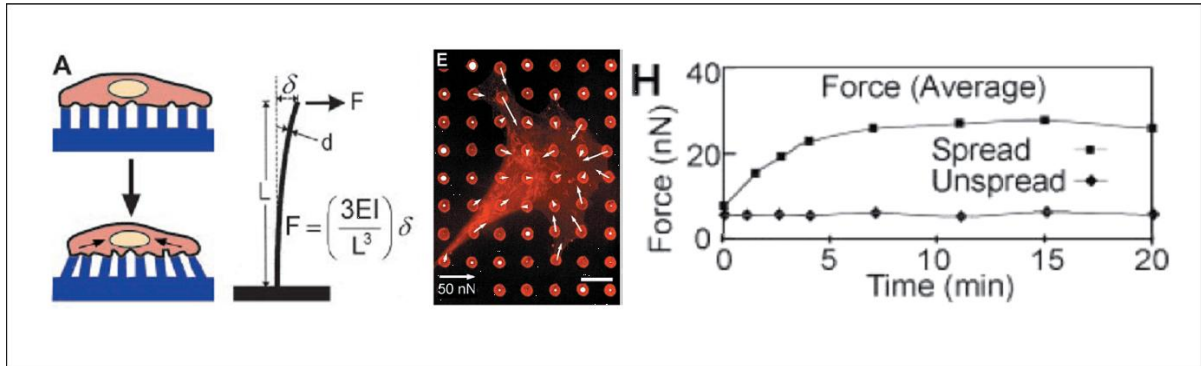


Figure 29. Three figures taken from reference [2] depicting the Chen group's microfabricated post array detectors (mPADs). At left is a diagram showing how cells deflect PDMS posts. The deflections are observed with a microscope, results shown at center. Force resolution is ~ 5 nN, limited by the ability of the cell to deflect one of the posts beyond the diffraction limit, and time resolution is ~ 30 s, limited by the cell's ability to generate a 5 nN force. The force versus time plot shown at right is an average over 18 cells which reduces the signal-to-noise ratio sufficiently to enable comparisons with my SCPFM data shown in Figure 28.

4.4 Fine structure

Within the data shown in Figure 28 there are three excellent examples of previously inaccessible molecular-mechanical processes that illustrate the immense potential of SCPFM to significantly enhance resolution of cell biology at the single cell level. Figure 30 shows an initial contraction upon exposure to CD followed by the expected force drop. Figure 31 shows small force oscillations, roughly 400 pN peak-to-peak, with frequency that is monotonically dependent on the force being exerted by the lamellipodia. Additionally, large, stable, quantized force steps of order 1 nN are manifested when a cell's cytoskeleton is perturbed with CD and allowed to recover in growth media, shown in Figure 32.

4.4.1 Fine structure I: initial spasm

CD is well known as a potent force disrupter, which is clearly shown in Figure 28. However, upon initial exposure to CD, I observe the cell contract quite suddenly before the expected force drop occurs. This spasm is reminiscent of the rapid rearward flow of cortical actin upon Cytochalasin B (CB) and CD exposure in spreading neuronal growth cones, first observed with DIC imaging 20 years ago by Forscher and Smith [187]. Figure 30 compares Forscher and Smith's image data and my force data, both show contraction upon exposure to CD.

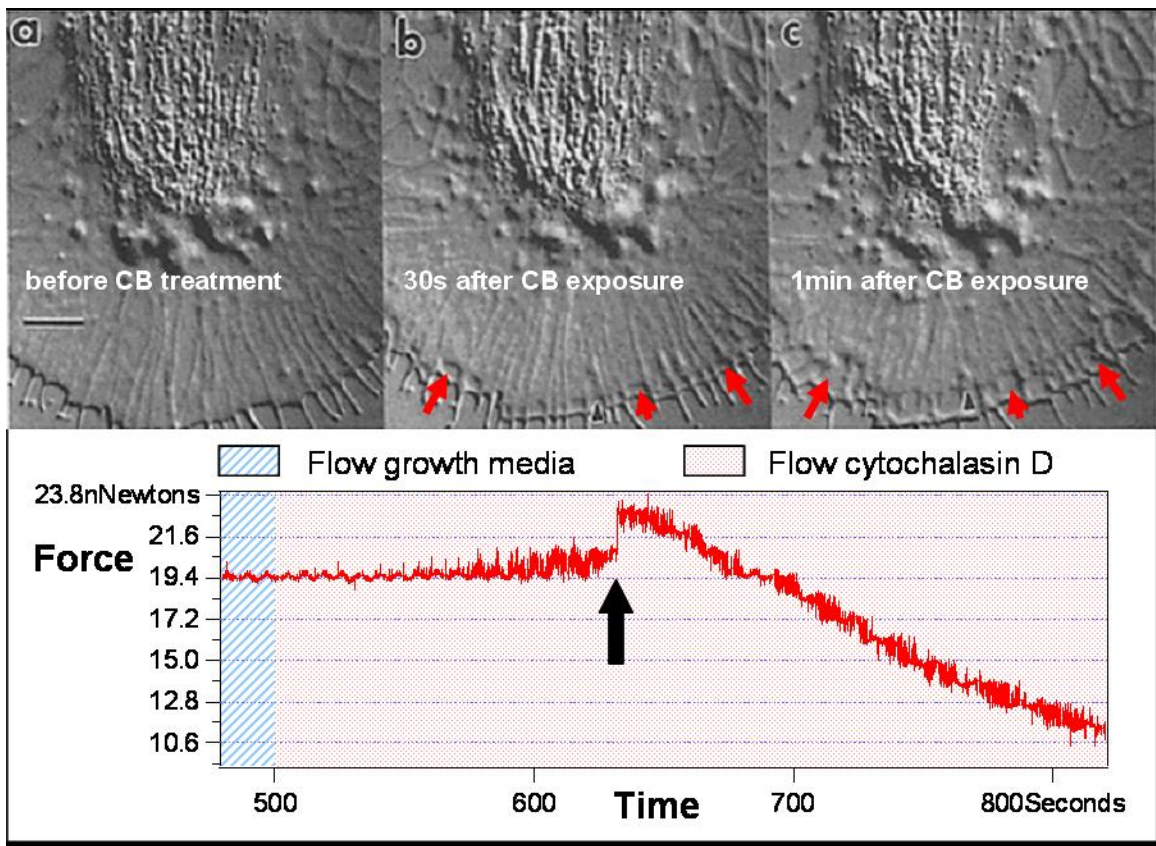


Figure 30. Forscher & Smith observed immediate, rapid retraction of f-actin from peripheral margin of lamella in spreading neuronal growth cones upon exposure to Cytochalasin B and D, images a – c at top. I observe a similar contraction upon initial exposure to Cytochalasin D, shown in force vs time plot at ~630s, the longer time delay in the plot is due to the time it takes for the CD solution to travel down the flow channel to the cell.

It has long been established that rearward flow of cortical actin exerts outward forces on the leading edge of lamellipodium [43, 188]. The molecular mechanisms have been studied in significant detail in spreading neuronal growth cones [189, 190], traveling epithelial cells [92, 97, 98, 191], fibroblasts [192] and keratocytes [193]. In all cases myosin contraction at the inner edge of the cortical actin and actin polymerization at the leading edge have been shown to drive the rearward flow, though the action of the two mechanisms is only weakly coupled. The Waterman group show quite clearly that CD stops the actin polymerization at the leading edge while myosin contraction continues to pull the cortical actin rearward [191]. It seems possible that the combination of the halt in polymerization driven outward force on the leading edge of the cell and the continued myosin contraction combine to produce the dramatic force increase seen in Figure 30.

4.4.2 Fine structure II: small oscillations

Throughout the data shown in Figure 28 there are quasi-periodic oscillations $\sim 400\text{pN}$ peak-to-peak with a $\sim 8\text{s}$ period (Figure 31). The oscillations persist throughout the stable force regions, the CD induced force decay and the force recovery. Interestingly, the frequency of the oscillations depends linearly on the force applied by the cell to the force sensor. The lower plot in Figure 31 shows a linear fit to the frequency as a function of force. The frequency versus force data was obtained by simply breaking the force versus time data into 200s intervals and Fourier transforming each interval to extract the dominant frequency. A wavelet analysis is merited to quantify these quasi-periodic oscillations in a more rigorous manner.

At one level of abstraction, this is not surprising – strings under tension vibrate at higher frequencies. However, we do not expect the cell-beam system to be inherently oscillatory. The water, not to mention the gel nature of the cell, will damp any thermal oscillations in the beam well below the level that can be measured [28, 194, 195]. The very long period ($\sim 8\text{s}$) rules out acoustic modes within the cell chamber

[28] and rules out any expected electrical interference. Furthermore, the oscillations were not observed on this particular beam and cell the day after this data was recorded, when the cell's membrane had become permeable and the cell had lost its spread shape. Nor have they been observed on any other beams.

There is, however, precedence for oscillatory behavior in the leading edge of spreading cells driven by polymerization dynamics of cortical actin. Both the Sheetz group and the Waterman group observed oscillatory behavior in spreading cells using DIC, TIRF [91, 92] and quantitative fluorescence speckle microscopy [98, 191, 196]. Unlike the oscillations I observe, both groups observe slightly longer periods (20-60s) with asymmetric duty cycles. However, in agreement with my observations, both groups did observe that exposure to cytochalasins (CB in the case of the Sheetz group and CD in the case of the Waterman group) increased the period. The Waterman group focuses on the very weak coupling yet cooperative action between the different cytoskeleton domains. The Sheetz group argues that the oscillatory behavior is due to alteration between actin polymerization extending the lamellipodium and myosin II contraction pulling the freshly polymerized actin rearward. These results are supported by Small's identification of two populations of actin filaments which alternately drive pushing and pausing at spreading cell fronts [197]. It seems plausible that the Sheetz model would describe my data and the weak coupling highlighted by the Waterman group could explain why the oscillations persist despite the other large cytoskeleton disruptions that are occurring. To test these ideas, I would like to perturb cells with more specific cytoskeleton perturbing reagents than CD in order to better decouple effects like myosin contractility and actin polymerization. I will discuss these proposed experiments in greater detail in Chapter 5.

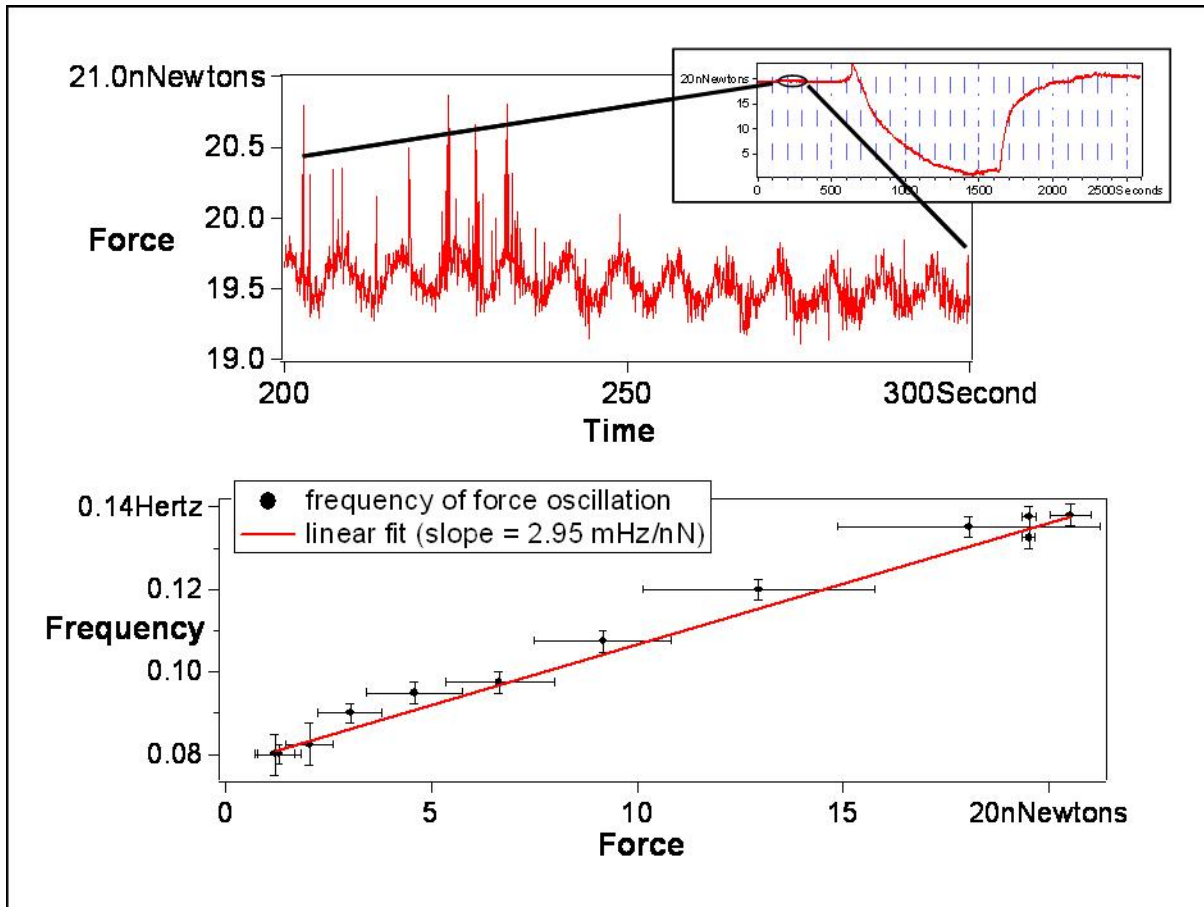


Figure 31. Quasi-periodic force oscillations ~ 400 pN p-p with a period ~ 8 s, shown at top. The force oscillation frequency depends linearly on the force applied to the NEMS force sensor by the cell, shown at bottom. The data at bottom was obtained by breaking the data shown at inset into 200 s intervals and Fourier transforming each interval to extract the dominant frequency, the solid line is a linear fit to the data. The frequency recovers with the force; one of the 3 data points at 20 nN is from after the force has recovered.

4.4.3 Fine structure III: steps

The third interesting example in the fine structure data from Figure 28 is the manifestation of ~ 1 nN force steps during both the CD induced force drops and the ensuing force recovery after CD removal. Representative steps from both a relaxation and contraction are shown in Figure 32. The steps in Figure 32 are highlighted with horizontal gridlines; it should be noted that the gridlines on both the relaxation and contraction are at the same force levels (the 10.5 nN line is on both plots). That is, the force steps are

aligned between relaxation and contraction to a shocking degree. There is sufficient drift in the measurement that the force steps from different cycles are not well aligned. The step size, however, is quite constant between cycles. A histogram of 119 steps from three relaxation-contraction cycles is shown in Figure 35. The mean step size is 1.0nN with a standard deviation of 0.2nN.

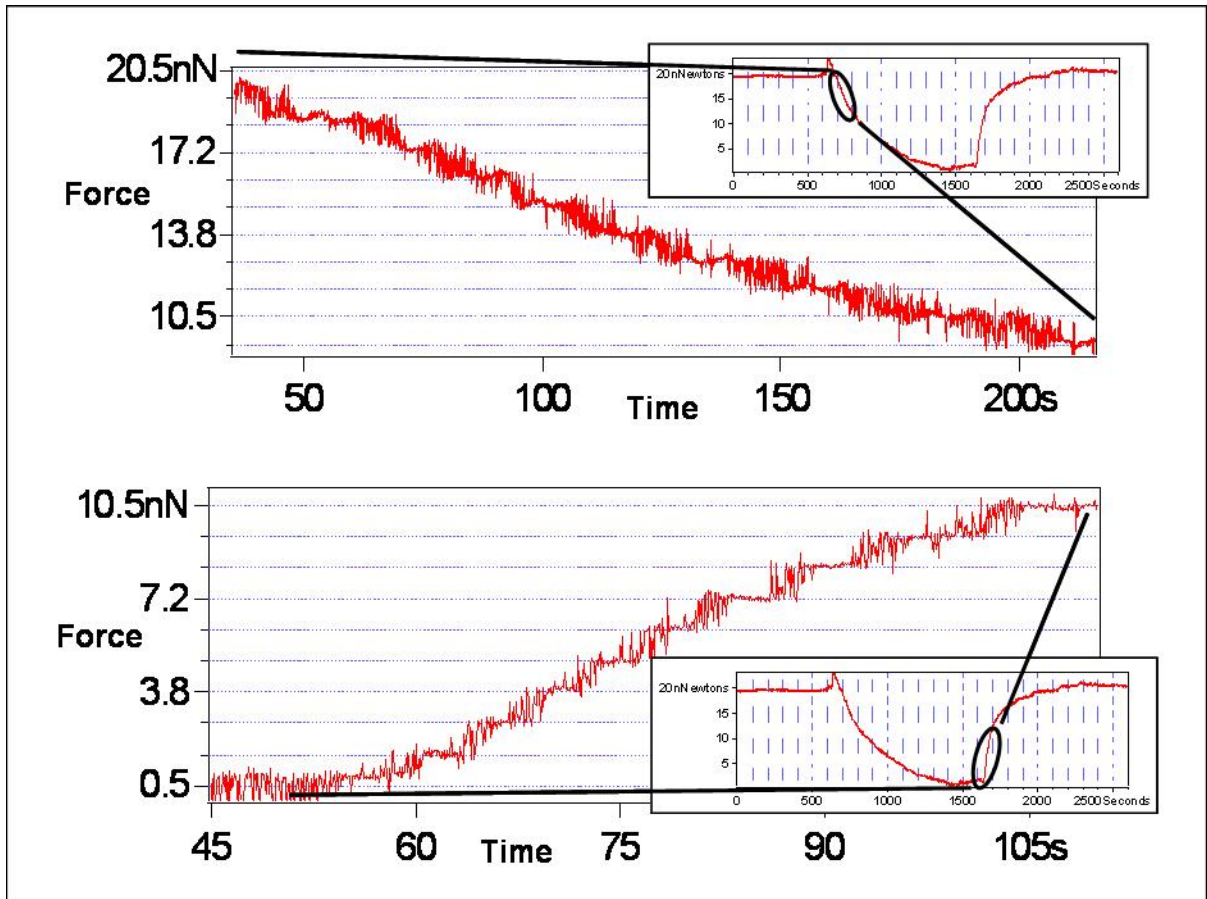


Figure 32. Quantized force steps of order 1nN are visible during Cytochalasin D induced force relaxation. The same quantized force steps (gridline spacing & offset is unchanged between plots) are manifested during the post-Cytochalasin D force recovery.

The noise like transition regions between the quiescent plateaus are noteworthy. First of all, recall that the force noise from the electronics in this data is approximately 200pN; this level that can be seen as the very quiet, almost flat regions at some of the steps. The noise-like transitions represent real changes in the force exerted on the beam by cell. One of the force relaxations contained a few steps with sudden

transitions between the quiescent plateaus; details are shown in Figure 33. Two of these three sudden transitions were followed by steps backward, the only steps backward that I observed.

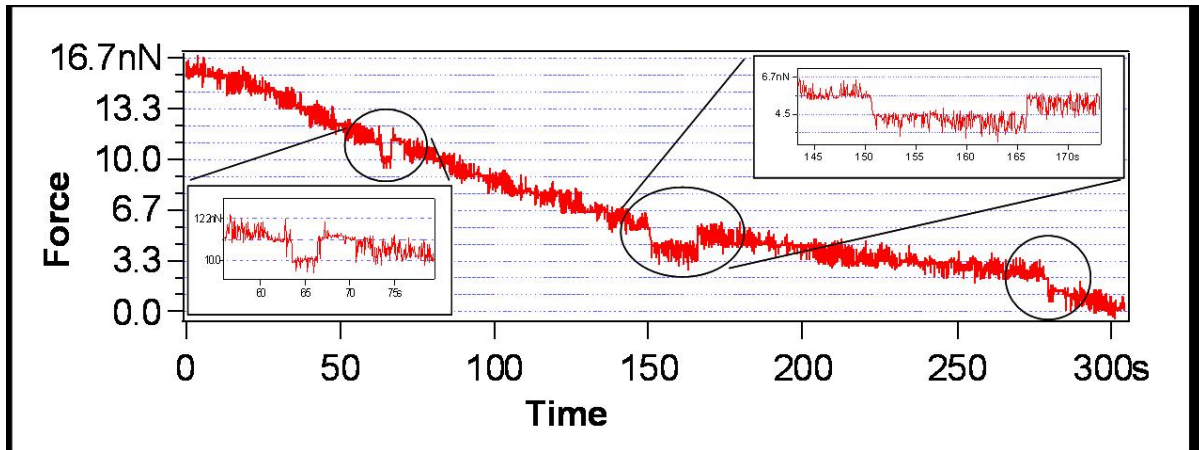


Figure 33. Not all steps have noise like transition periods and more often than not, steps with sudden transitions are followed by steps backward, also without transition periods.

I have written a step fitting algorithm so that I can extract statistical and dynamic quantitative data from the relaxation and contraction cycles. The algorithm is implemented in Igor, the same software package that I use for experiment control and data acquisition, and is inspired by a step fitting algorithm for tracking microtubule dynamics [198]. It is easy to create an algorithm that fits n steps to a data set. So in order to determine the correct number of steps, N , the algorithm creates fits for a range of different n 's as specified by the user. Comparing the chi-squared for each of these fits singles out the best fit, which I confirm visually. This fixes the number of steps at N and the size of each step. The results of this initial fit are shown by the black line in Figure 34. This initial fit determines the levels of each step – the “step size” shown in Figure 34 – but not the dynamics of the step transitions. A second fitting process fits a more complex step profile, shown in blue in Figure 34, to the quiescent plateaus and the noise like transitions that make up each step. In addition to the histogram data mentioned previously, Figure 35 contains a representative plot of the step rate as a function of force during a contraction. The step rate increases linearly until approximately 5-7nN of force have been generated and then decreases exponentially until approximately 20nN of force have been generated. In contrast, the step rate decreases

linearly during the relaxation processes; see Appendix 6 for complete contraction and relaxation dynamics data. Beyond the specifics of these steps, Figure 35 is illustrative of the kind of statistical and dynamic data which SCPFM is capable of obtaining.

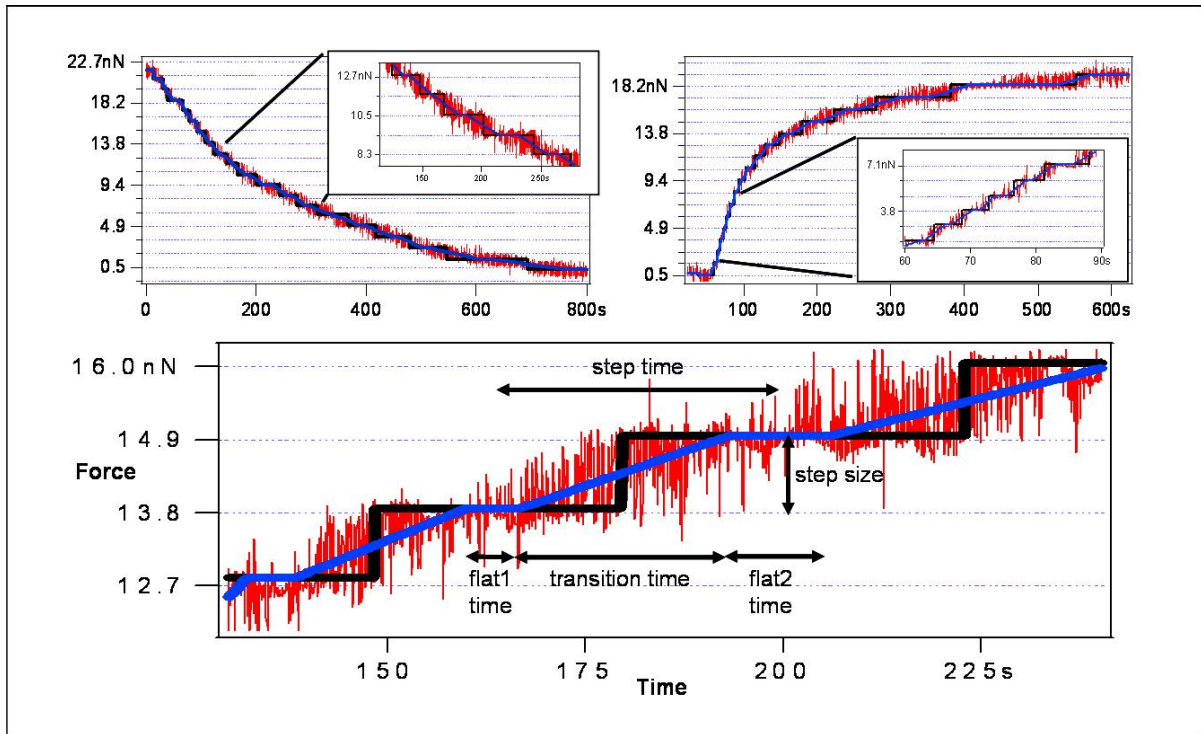


Figure 34. Anatomy of a step. The step fitting algorithm runs in two phases: an initial fit that looks only for steps and attempts to determine the number of steps in a given data set. The results of an initial fit are shown above in black, the initial fit determines the step time and step size for each step, as marked above. The secondary fit starts with the output from the initial fit and replaces the step transition with a linear fit to through the transition zone, thus breaking each step into flat1, the transition and flat2, as marked above. Plots at top show data (red), initial (black) and secondary (blue) fits for a relaxation (left) and a contraction (right); insets show greater detail.



Figure 35. Examples of the statistical and dynamic data which can be obtained with SCPFM. Above left is a histogram of step sizes from 3 Cytochalasin D induced relaxation and contraction cycles on a single cell.

Above right is a plot of the step rate as a function of force during a contraction showing a linear acceleration regime and an exponential deceleration. See Appendix 8 for complete contraction and relaxation dynamics data.

Actin-myosin generated step forces have been measured from single filopodia extending from macrophages [7]. Stress fibers, which carry the large contractile forces in cells, are parallel bundles of the same actin-myosin filaments that drive filopodia extension. The contractile force in stress fibers is generated by myosin motors stepping along opposing actin filaments [43]. Thus, it is conceivable that actin stress fibers could generate large step forces if the many myosin motors in a stress fiber make coordinated steps. 200-500 myosins would be needed to generate $\sim 1\text{nN}$ force steps [82, 199, 200]. It is actually expected that nearby myosin motors within a given stress fiber would be coordinated because uncoordinated motion would require adjacent motors to buckle the actin filaments [201, 202]. So, it seems plausible to me that a stress fiber undergoing controlled relaxation and contraction could create the steps shown in Figure 32.

Despite my claim to plausibility, there are some clear problems with this hypothesis. First, typical images of cells where the stress fibers have been fluorescently labeled show many stress fibers radiating out from a single focal adhesion. While I can argue for coordinated myosin steps within a stress fiber, it is much harder to conjure an explanation for coordinated myosin steps between multiple stress fibers. Secondly, how CD would induce such a regular and reversible myosin stepping is not clear to me. Despite CD's complicated and promiscuous behavior, I have encountered no references to CD interacting with myosin, in fact quite the opposite [92, 196]. The reversible nature of the force drop suggests very strongly that the CD exposure is not causing large scale reorganization or collapse of the cytoskeleton, such as disassembly of the stress fibers. Instead, it seems likely that the CD is meddling with the connections between the stress fibers and the focal adhesions.

Focal adhesions are immensely complex and it may be possible that the CD-focal adhesion-stress fiber interaction somehow triggers reversible myosin relaxation steps in the stress fibers [49, 93, 149, 203-207], but, that seems a stretch to me and certainly fails Occam's razor. Instead, fluorescent images of many stress fibers radiating out from a single focal adhesion suggest an alternate model: each stress fiber applies a fixed force to the focal adhesion, the parallel forces add and deflect the force sensing beam, which is a linear spring. When the CD disconnects a stress fiber from the focal adhesion, the total force will drop by the amount of force generated by that stress fiber, resulting in steps. If, each stress fiber carries nearly the same force, the steps sizes will be equal in size, as seen in my data, but, this model is flawed too: it does not explain the steps in the force recovery so well, nor do the fluorescent images of stress fibers suggest large numbers of nearly identical stress fiber radiating out from a focal adhesion. Perhaps there is a force limiting aspect to stress fiber assembly that distributes the force roughly evenly. I could go on and on with these guesses...

Extensive efforts have been made to model actin-myosin dynamics and force generation in muscle contraction [208-210] and more modest efforts have gone toward modeling cooperative motion of molecular motors [211-213]. Adapting some of these modeling efforts to my system and comparing the results with the dynamics of the force relaxation and contraction steps, such as the data in Figure 35, would likely help validate or disprove these hypotheses. Additional data would also be helpful, specifically force data that includes fluorescent images of stained stress fibers and more specific cytoskeleton perturbing reagents. Goals, which I discuss in Chapter 5.

4.5 Problems repeating measurements

The data shown above constitutes an excellent demonstration of the principle and potential of SCPFM. I have measured the force exerted by a single lamellipodia of an adherent cell, disrupted the force using CD, a known cell force disruptor, and observed the force recovery upon removal of the CD. The coarse

structure of the data agrees well with existing, coarse force data measured optically. The fine structure of the data is rich in detail and processes that have previously been inaccessible to force measurements. I am able to correlate the fine structure processes with behaviors observed optically in adherent cells, lending support to the relevance of the data obtained with SCPFM.

However, I have been unable to repeat these measurements. There are numerous complications related to the complexity of the tool and measurement process that somewhat hinder my ability to attempt to repeat that measurement as frequently as desirable, but, I believe that the principle problem is standardizing the cell-beam interaction. I have only been able to attach cells to beams when treating the entire cell chamber to fibronectin, so I have no control over where and how the cell attaches to the force sensor. The data shown in Figure 28 is the only data I have from a cell that is attached to the beam with the edge of a single lamellipodia. I have numerous data sets from cells that are attached to much larger areas of the beam with large or multiple lamellipodia, or even wrapped around the beam. The data from these sets is very difficult to interpret, and I am unable to reproduce the basic relaxation, contraction sequence shown in Figure 28.

I am not alone in finding that controlling cell-surface interactions is necessary to obtaining repeatable data. Controlling – specifically standardizing – cell-surface interactions has been critical to obtaining regular and statistical data in a number of studies of cell-surface interactions [2, 147-151]. I believe that successfully transferring my surface chemistry strategy from working Petri dish protocols to my microfluidics encapsulated NEMS force sensors will yield repeatable and understandable data on a regular basis. I have strong evidence that the problem with transferring the surface chemistry to the NEMS chips is due to PDMS out-gassing in Table 7. I further have evidence from numerous other research groups that solvent extraction treatments of the PDMS, perhaps in conjunction with a switch from RTV 615 to Sylgard 184, will solve the PDMS out-gassing problem [129, 132-137].

Controlling surface chemistry on the microfluidics encapsulated NEMS force sensors is necessary to obtaining repeatable data with SCPFM. Robust cell culture, while perhaps not strictly necessary, will further increase measurement yield. My ability to culture cells in the NEMS devices is limited. Cells live long enough to run a day's work of experiments: load cells, allow cells to spread and attach to the force sensor and then spend a couple of hours observing the force response to pharmacological perturbations before the cell dies. However, robust long term cell culture will yield a number of significant improvements. First, the odds of a cell successfully attaching to the force sensor will increase because the cell will have much more time to explore its surroundings, find the beam and attach before beginning to die. Robust, healthy cells will be able to withstand repeated exposure to the cytotoxins which disrupt the cytoskeleton, so a given cell will yield greater data. Finally, data obtained from sick or dying cells is of clearly questionable biological relevance compared with data from healthy cells. I am optimistic that the same PDMS sourced contaminants that are interfering with my surface chemistry protocols are poisoning the cell culture in the microfluidics encapsulated NEMS devices.

Beyond these improvements to my existing system and device architecture, there are two key shortcomings to SCPFM with my current device architecture: 1) sensor density is sparse at a max of two force sensors per cell and 2) I cannot use the devices to actively apply forces to the cells – they can only balance the forces applied by the cell. The Roukes Group is actively pursuing CMOS integrated NEMS and CMOS and NEMS compatible piezoelectric materials that will likely offer long-term solutions to both of these problems.

Chapter 5. Next steps

5.1 Next generation SCPFM

I have achieved promising proof-of-principle data and believe that contamination from unpolymerized PDMS is the principle barrier preventing repeatable data acquisition. Nevertheless, there are numerous improvements that can be made to the existing system in addition to addressing PDMS contamination. First, increasing the density of force sensors and cell chambers per chip will increase throughput by reducing the setup time per force sensor and will enable simultaneous testing a larger range of conditions per chip that will accelerate debugging and optimizing the system. An automated microscope will be necessary to take full advantage of the increased sensor density so that stepping between cell chambers and imaging can be done in a timely and standardized manner. A microscope capable of observing the cell with both transmitted and reflected light is also critical, so that the cells can be observed with optical wavelengths that will not harm the cell, as fluorescent excitation does. I am optimistic that these workstation improvements, coupled with solvent extracted PDMS, will make systematic studies of molecular level mechanical responses to mechanical and chemical stimuli in single cells routine.

5.1.1 Polymer NEMS with off-chip multiplexing

We† recently received a new fully automated microscope (Zeiss Axio Examiner) that will add transmitted light with oblique optics to the existing reflected fluorescent imaging capabilities. The computer controlled microscope will enable us to scale up the number of cell chambers per chip that we can utilize at once. Toward that end, I have finished a mask set for a new chip design that will place 16 cell chambers and 32 force sensors onto a single 30mm square chip and will be fabricated on 6-inch wafers with 12 chips and 384 force sensors per wafer. I have designed and bread-board tested a decoder circuit

† Going forward graduate student Paula Popescu and staff member Jessica Arlett will be working with me, so I am shifting verb tenses.

that will be integrated onto the circuit board within the microscope-mounted-incubator-and-sample-holder for accessing all 32 force sensors and the 160 electrical contacts they require. The new chip design and microscope will require a new sample holder and incubator design that is in progress and will utilize a new LiveCell control unit with added humidity control and improved CO₂ and temperature control.

5.1.2 LETI silicon NEMS with on-chip multiplexing

We can achieve some increase in density by adding the off-chip decoder circuitry; however, the sensor density is still severely limited by fan-out and electrical contact pad areas. The long term solution to the sensor density problem is to integrate multiplexing, driving and sensing hardware onto the same chip as the force sensors. Complete system integration of this type has been achieved with MEMS pressure sensors [214-216]. NEMS system integration has not been achieved yet and brings a significant set of challenges which the Roukes group is working hard to address. Since June 2006, the Roukes group has spearheaded a partnership between Caltech's Kavli Nanoscience Institute (KNI) and the CEA/LETI – Minatec in Grenoble, France, with the goal of transforming nanotechnology-based prototypes into robust, complex sensing systems. Key technologies that will be developed through this collaboration are the integration of driving, multiplexing and sensing circuitry with piezoresistive and piezoelectric NEMS devices. Jessica Arlett is leading the effort to merge SCPFM with the CMOS compatible NEMS technology. Significant process and technical development remain to be done, but ultimately this partnership will yield the significantly greater sensor density as well as piezoelectric NEMS capable of mechanically prodding and tugging on the cells while measuring the cell's response. These integrated NEMS are the long term solution for SCPFM; however, in the near term cell force data acquisition will still be led by the polymer NEMS technology described in Chapters 3 and 4.

5.2 First experiments

I am hopeful that the PDMS extraction strategies outlined in Chapter 3 will resolve the outstanding surface chemistry and tissue culture issues. The new chip design with 16 cell chambers and 32 force sensors per chip will significantly reduce the setup time per sensor and increase the odds of a cell-beam interaction. The new microscope with both reflected and transmitted light capabilities will significantly enhance our ability to monitor and track the state of the cells under study. The ability to fully automate the microscope stage and imaging capabilities will let us make full use of all 16 cell chambers on the new chips, thus significantly improving measurement throughput. I believe that these advances together create a clear and realistic roadmap to routine, daily generation of quality cell-force data by the summer of 2009. With that timeline in mind, I propose two generally complimentary experimental efforts to undertake: first, a systematic effort to build a library of molecular-mechanical force signatures of various common cytoskeleton reactions, and second, an effort to stimulate and observe compliance sensing and response in adherent cell by simultaneously presenting two force sensors with different compliances to the cell.

5.2.1 Pharmacological perturbations: building a library of molecular-mechanical force signatures of basic cytoskeleton reactions, or fishing with drugs

Over the past 45 years a library of cytoskeleton perturbing reagents has been slowly identified and characterized [217, 218]. I propose to use this library of cytoskeleton perturbing reagents to systematically explore and characterize the molecular-mechanical force signatures of basic cytoskeleton reactions such as actin filament polymerization and de-polymerization. I take inspiration from the Fernandez group's ability to identify proteins by the folding-unfolding dynamics using high resolution force spectroscopy [219-221] and from the unique events in my existing data, such as the force

dependent oscillations (Figure 31) and regular force steps (Figure 32). Building this library will serve two principle purposes. First, the library will be an integral part of the larger goal of developing SCPFM into a tool that can reliably extract physiological information from a cell through the molecular-mechanical force signatures of known cytoskeleton events. Second, building the library is basically an open ended fishing expedition that will almost certainly stumble across many interesting and unexpected phenomena, such as the force steps that I have already observed.

5.2.1.1 Actin-myosin

The logical starting point, both from a fundamental cell force generation perspective and from the proof-of-principle data that I already have, is to probe actin polymerization and de-polymerization. Latrunculin A [222] is a much better candidate for inducing controlled actin de-polymerization and thus force relaxation than Cytochalasin D. Latrunculin A sequesters actin monomers in a reversible 1-1 binding reaction [223] that shifts the actin monomer-filament equilibrium [61] toward monomers, thereby inducing filament disassembly. The complimentary experiment, actin polymerization or filament stabilization, is trickier than inducing de-polymerization because cells regulate actin polymerization in large part by controlling the nucleation of actin filaments. Actin stabilizing agents encourage nucleation, thereby overriding the cell's regulatory mechanism, resulting in uncontrolled actin aggregates [224]. However, low dose (30-50nM) and short term (2 hours) exposure to Jasplakinolide has been shown to inhibit filament disassembly in fibroblasts without inducing unregulated actin aggregation [225]. Two hours is more than sufficient time to run numerous experiments with SCPFM; thus, we plan to use Latrunculin A to induce actin de-polymerization and Jasplakinolide to stimulate actin stabilization and polymerization, while taking care to avoid longer exposure that would complicate results.

Myosin II motor proteins cross-link actin filaments within stress fibers and drive stress fiber contraction by converting the chemical energy released by ATP hydrolysis into mechanical work. This is the same

mechanism that drives muscle contraction; as a result, it has been studied extensively and is well characterized [226]. Perturbing myosin activity is relatively simpler than perturbing actin dynamics because one is not competing with equilibrium dynamics. Blebbistatin is a well characterized, cell permeable reagent that blocks myosin II force generation. Blebbistatin binds to a cleft in myosin that prevents ejection of the used ADP molecule after the power stroke and release from the actin filament, thereby deactivating the myosin molecule and holding it detached from the actin filament [227, 228]. Calyculin A is a cell permeable reagent that stimulates myosin II activity through a slightly more complex, though well characterized mechanism. Myosin II activity is regulated in part by phosphorylation of the myosin head groups (myosin light chains). Activity is increased by phosphorylation performed by Ca^{2+} , Calmodulin and Myosin Light Chain Kinase (MLCK) working in concert, and activity is decreased by dephosphorylation performed by a variety of protein phosphatases (PP1, PP2A, PP2B are some of the most common). Calyculin A blocks the action of protein phosphatases, particularly PP1 and PP2A, which takes away a cell's ability to slow myosin activity [229]. We will use Blebbistatin and Calyculin A to characterize the molecular-mechanical force signatures of myosin deactivation and activation respectively.

5.2.1.2 Microtubules

Microtubules play a critical organizational and mechanical role in mitosis [43]. Though numerous questions remain regarding mitosis regulation, many microtubule perturbing reagents have been identified and characterized in the search for chemotherapeutics that disrupt mitosis [57, 218]. Microtubules perform other functions within a cell beyond their role in mitosis. In particular, there is evidence that they regulate focal adhesion disassembly and perhaps assembly [59, 60, 230]. In its current geometry and device density, SCPFM is not well suited to observe mitosis, but it is very well suited to study focal adhesion regulation and subsequent force regulation, which we will probe using the same strategy to be used with actin and myosin: controlled and specific pharmacological perturbations.

Similar to actin perturbing reagents, microtubule perturbing reagents can generally be broken into two categories: microtubule stabilizers and microtubule disruptors. However, both classes have concentration dependent effects to which close attention must be paid. Paclitaxel (Taxol) is the most extensively studied of the large taxane class of microtubule stabilizers [231, 232], which are used to treat ovarian, breast, lung, prostate and brain cancers. At low concentrations (<10nM) paclitaxel stabilizes microtubules without stimulating new polymerization; whereas, at high concentrations (~100nM) paclitaxel will drive microtubule polymerization. Laulimalide is a newer microtubule stabilizer that binds to a different site on the microtubules which has not been fully characterized [233]; it may prove fruitful to compare paclitaxel and laulimalide because of their different binding sites. There are two well studied classes of microtubule disruptors: vinca alkaloid and colchicine related compounds. Both suppress microtubule dynamics at low concentrations, like paclitaxel, but depolymerize microtubules at high concentrations. The vinca alkaloids, which are used to treat Hodgkin's disease, Leukaemia, lymphomas, bladder, lung, breast and other cancers, cap the ends of microtubules at low concentrations and bind to and destabilize tubulin dimers at higher concentrations which drives depolymerization [218]. It is believed that colchicines bind to soluble dimers which destabilize microtubules when they are incorporated [218]. These drugs give us a number of tools to observe how microtubules regulate focal adhesions by driving and suppressing dynamics as well as disrupting microtubule ends, which are believed to interact with focal adhesions. A third approach for perturbing microtubule dynamics is Isopropyl N-3-chlorophenyl carbamate (CIPC), a compound which prevents microtubules from connecting to microtubule organizing centers [234]; we may experiment with this avenue of perturbation as well.

5.2.1.3 ECM and integrins

Another critical area to investigate is the focal adhesion to ECM contact and its role in regulating focal adhesions. Focal adhesions are linked to the ECM by transmembrane integrins [43]. Proper nucleation and activation of integrin clusters is necessary for focal adhesion formation [66, 94, 235]. The same

approach of controlled and specific pharmacological perturbations can be used with integrins: RGD peptides compete with the ECM for integrin binding [236], EDTA and Versene chelate and sequester Ca^{2+} which is a necessary mediator of the integrin-ECM bond, and trypsin is a serine protease which digests the extra-cellular portion of the integrins [167].

5.2.1.4 Upstream regulation

The goal of using SCPFM to monitor cell physiology through cell mechanics relies on the fact that there are a considerable number of signaling proteins which interact with the cytoskeleton. Once we have obtained the molecular-mechanical force signatures for the basic actin and microtubule reactions we can investigate how interfering with signaling proteins upstream from the cytoskeleton drives those reactions. The Rho family of GTPases, particularly Rho, Rac and Cdc42, were the first example of small molecular “switches” that regulate cytoskeleton behavior when they were shown to regulate stress fibers, focal adhesions and membrane ruffles [237, 238]. The Rho family of GTPases has been studied extensively in the past 15 years and remain the focal nodes of complex signaling networks that play a major role a diverse range cellular processes from determining cell morphology and movement, to cell division, gene regulation and phagocytosis [239, 240].

Many molecules have been identified in the various upstream, downstream and cross-talk pathways involving Rho GTPases [241]. I outline here a couple of highlights that are good places to start with SCPFM. Lysophosphatidic acid is interesting because it stimulates Rho activity and thus myosin contraction through surface receptors rather than diffusing into the cell itself [242-244]. Adjusting the activities of two down stream targets of Rho: Rho-kinase and mDia, by transfection, adjusts the density and thickness of stress fibers, though adjusting the activity of Rho itself is insufficient to tune the stress fiber thickness [245]. It would be particularly interesting to see how stress fiber thickness affects the force step size and dynamics discussed in Chapter 4. Following the strategy that I have outlined for

actin-myosin and microtubule perturbation, a number of small molecule toxins have been identified that perturb the Rho pathways: C3, an exotransferase produced by *Clostridium botulinum*, inhibits nucleotide exchange thus deactivating Rho and the cytotoxic-necrotizing factor produced by several pathogenic strains of *E. coli* activates Rho [246]. Some other examples of commonly used signaling proteins that interact with the Rho pathways include: Calyculin A, which I have already discussed as a stimulant of myosin activity; Y-27632, a synthetic pyridine derivative that inhibits myosin activity by blocking the Rho-ROCK pathway [247]; and N-WASP, a small molecule target of Cdc42 which drives actin gel polymerization [248].

5.2.2 Mechanical perturbations: molecular mechanisms of mechanotransduction

The second experimental effort that I propose is to investigate the mechanisms which drive mechanical feedback in cell regulation. Cells use mechanical feedback to maintain adhesion, tension and cell shape [196, 249, 250]. Substrate compliance plays a significant role in stem cell differentiation: cells on stiff substrates differentiate toward bone cells whereas cells on soft substrates differentiate toward nerve cells [45]. Fibroblast motility also depends on substrate compliance, an effect termed durotaxis [46]. ECM compliance sensing has further been shown to play a significant role in regulating tissue development [47] and basic models have been proposed [48]. All of these processes are driven and regulated by feedback between cellular force application and compliance sensing. SCPFM is well suited to study this because it can simultaneously present multiple compliances to a cell and measure the cell's force response to each compliance individually. We will focus our efforts on the specific phenomenon of ECM compliance sensing, decision making and force generation response which drives durotaxis as a model system for studying the mechanisms which drive mechanical feedback in cell regulation.

5.2.2.1 Mechanical stimulation

We are able to present two force sensors to a single cell in a configuration where the force sensors have different widths, thus different spring constants, which present to the cell as different ECM compliances. Figure 19 shows 2 μ m and 4 μ m wide beams adjacent to a single cell pad area. This mimics the durotaxis phenomenon first observed by Wang and Dembo [46]: we expect the cell will sense the compliance difference between the beams and decide to pull hard on the stiff force sensor and not on the soft force sensor. We will be able to observe the forces exerted by the cell during the compliance sensing, decision making and responding force generation phases continuously and at high resolution. Table 8 lists effective spring constants for Wang and Dembo's traction force microscopy substrates, Chen's mPADs [251] and our NEMS force sensors, and shows that our sensors span the relative compliance ranges to stimulate ECM compliance sensing and response. Our NEMS force sensors are well suited to stimulate and measure high resolution force-time records of ECM compliance sensing and response events. The principle hurdle to this experiment is the low stochastic probability of a cell grabbing not just one, but both beams. I am hopeful that optimizing surface chemistry and device geometry will increase the frequency of these events and direct the cell to respond to the compliance of the beams.

My understanding of how cells interact mechanically with their environment is driven by Bischofs and Scharz's simple observation that the typical response of a cell to mechanical input is a preference for large effective stiffness [252]. This observation that cells pull harder on stiffer substrates successfully explains a large body of experimental data: Cells plated on stiffer substrates show greater spreading and larger focal adhesions [64]. Fibroblasts on elastic substrates orient in the direction of greater tensile strain [253] and travel to regions of greater stiffness [46]. Various observations of the behavior of cells grown in three-dimensional hydrogels, such as collagen, also support the preference for greater stiffness hypotheses [254-256].

Bischofs and Schwartz quantify their observation with the claim that calculating the amount of work a cell must do to deform the substrate around it in various ways is an appropriate measure of the kind of information that the cell can extract from its environment. They assume the cytoskeleton is anchored at multiple points on the cell in such a way that force balance is ensured (the cell does not travel), thus, only pairs of pinching forces, technically known as anisotropic force contraction dipoles, P , are considered. The mathematically simplest case requires that the points on the substrate where the pinching forces are applied be mechanically uncoupled and that the deformations are small enough to remain linear with respect to the applied force, in which case the work done by the cell in deforming the substrate is derived from Hook's law:

$$\Delta W = -\frac{1}{2} K \Delta^2, \quad (17)$$

where, K is the spring constant and Δ is the displacement of the substrate. This is the situation for the Chen group's mPADs [2] and for the NEMS force sensors used by SCPFM.

In contrast, most work done studying cell adhesion, locomotion and force transduction has been on continuous elastic substrates where the different components of the displacement field are coupled, which makes the mathematics significantly more difficult. Bischofs and Schwartz use Green functions to solve for the work done by the cell in a few common substrate geometries. For an infinite, homogenous substrate the work depends on the relevant force contraction dipoles, P_{ij} , and the strain tensor:

$$\Delta W = -\frac{1}{2} P_{ij} u_{ij}. \quad (18)$$

This equation should be roughly applicable to much of Wang and Dembo's work; however, their papers only include the calculated traction force data (force dipoles), not the measured strain data [3, 4, 46, 257]. From their calculations for common substrate geometries, Bischofs and Schwartz deduce the following general scaling relation which should be useful for qualitative analysis of more general geometries:

$$\Delta W \sim \left(\frac{P^2}{El^3} \right) f(\nu, \theta_i), \quad (19)$$

where, the length l is either a distance, such as between the cell and a boundary, or the sample size, E is the Young's modulus and f is a nontrivial function of the Poisson ratio and the angles between the individual force dipoles.

An alternative approximation that is applicable to Wang and Dembo's work is to treat a single point source displacing the surface. Bruinsma calculates the displacement from a single point source [258]:

$$\Delta X(\vec{r}) = \frac{(1+\nu)}{\pi E} \int d\vec{\rho} \frac{\sigma_0(\vec{\rho})}{|\vec{r}-\vec{\rho}|} \left\{ (1-\nu) + \nu \frac{(x-\rho_x)^2}{|\vec{r}-\vec{\rho}|^2} \right\}. \quad (20)$$

Equation (20) is clearly undefined for the displacement of the surface at the actual point source ($\vec{r} - \vec{\rho} = \mathbf{0}$); however, Bruinsma applies asymptotic methods to the integral in equation (4) and to first order the displacement is:

$$\Delta X \approx \left(\frac{1}{Ea} \right) F, \quad (21)$$

where, a is a characteristic dimension of the area over which the force is applied – *e.g.*, the diameter of a focal adhesion – and F is the traction force exerted by the focal adhesion. Equation (21) is a formulation of Hook's law that can be applied to the displacement of a point on a semi-infinite substrate such as those used by Wang and Dembo. Table 8 contains quantitative comparisons between the compliances presented to cells by the mPADS, traction force microscopy and SCPFM obtained using equations (17), (19) and (21).

Method	Device	Spring Constant	Hard/Soft
Traction Force Microscopy	Soft substrate	~100 mN/m	~3
	Hard substrate	~300 mN/m	
mPADs	15 μ m pillar	12 mN/m	2.8
	11 μ m pillar	32 mN/m	
Single-Cell-Pico-Force-Microscopy	1 μ m wide beam	50 mN/m	6.7 6
	2 μ m wide beam	350 mN/m	
	4 μ m wide beam	2.6 N/m	

Table 8. Comparison of spring constants from compliance sensing and response observations. Traction force microscopy is the technique where durotaxis was first observed. 15 μ m long mPADs were not stiff enough to generate contraction, whereas 11 μ m mPADs were. The last row indicates that NEMS force sensors for SCPFM that have been fabricated span a sufficiently large range to stimulate compliance sensing and response. SCPFM acquires force data at 10x better force resolution, 100x better time resolution and equivalent dynamic range as traction force microscopy and mPADs.

5.2.2.2 Mechanotransduction and response

Bischofs and Schwartz's insight makes no statement regarding how the cell senses the stiffness of the matrix around it or how the cell decides which focal adhesions to pull on and which to abandon. Ingber favors a passive process, whereby it is more efficient for the cell to build contacts to stiffer regions than to softer regions – the cell builds contacts to both, but the stiffer regions develop faster and soon dominate [34, 35], an idea supported by characteristics of non-linear biological gels [259] and complex force responses measured with mPADs [87]. Ingber appears to avoid the issue, but it seems to me that such a passive mechanism would still require an off switch, which could be passive as well, in order to prevent the soft contacts from eventually catching up with the stiff contacts. Both Geiger and Small suggest that microtubules could be involved in stopping the buildup of force [50, 230].

An alternative mechanosensor and decision making mechanism based upon an active molecular switch has been put forward by Geiger [204]. In Geiger's scheme a mechanically sensitive molecule located in the focal adhesion plaque would encourage focal adhesion maturation into a focal complex when activated by the compression, which is larger on stiffer substrates, at the front edge of the focal adhesion.

Following Geiger's general lead Bruinsma presents a detailed statistical mechanics model of integrins working as substrate stiffness sensors to control the conversion of an initial adhesion to a focal complex. Bruinsma's model assumes an ECM bound integrin molecule and an actin filament traveling at a constant rate. The integrin and actin molecules stochastically bind and unbind in a weak – “passive” – bond, thus defining a mechanical diffusion time during which the integrin and actin are weakly bound. The constant motion of the actin filament results in a ramped force applied to the integrin and through the integrin to the ECM. The total force is determined by the force loading rate of the traveling actin and the mechanical diffusion time. The key issue, however, is how the force is distributed between the integrin and the ECM. If the ECM is particularly compliant, the integrin molecule will be able to move with the actin filament, thus transferring most of the force to the ECM. However, if the ECM is particularly stiff, the integrin will be unable to move far and a much greater proportion of the force will be applied across the integrin. The greater level of force will switch the integrin's conformation into a strong – “active” – bond with the actin that does not break apart after the mechanical diffusion time and enables the creation of a focal adhesion at the site of the active integrin-actin bond. This process is akin to a fisherman setting a hook. This model is supported by structural studies showing that integrins can exist in two distinct conformations [67-69]; however, vinculin [70, 71], talin [73], pp60src [74] and fibronectin [49, 75-78] – all present in focal adhesions – have also been observed in two conformations.

These theoretical efforts have launched a search for the molecular switch, or more likely switches, that mediate mechanotransduction. Tyrosine phosphorylation of focal adhesion proteins has been a focal point of the search so far [260]. The Geiger group has identified tyrosine phosphorylation of paxillin as a

critical regulator of focal adhesion formation. Integrin activation has been shown to lead to tyrosine phosphorylation of paxillin, thus creating a possible link to a force switch. More compelling, from the mechanotransduction perspective, is the Sheetz group's work with p130Cas. First they noted tyrosine phosphorylation of p130Cas is involved in force activation of the Rho GTPase Rap1 [261]. Recently, they observed marked enhancement of phosphorylation of p130Cas in a mechanically extended state and, using an antibody specific to the extended p130Cas, correlated the mechanically extended state with regions of spreading cells where higher forces are expected [52]. Much work remains to be done to understand the full role of p130Cas in mechanotransduction and the likelihood of other mechanotransduction mechanisms in focal adhesion regulation [262].

High resolution force-time records of ECM compliance sensing and response events will provide useful information; for instance, the magnitude of the forces needed to drive a decision event will indicate the rough number of molecular switches involved or the rate of force generation will yield information about how forces are regulated. I believe that we can also determine the identity of the molecules driving the force events in a data trace using the library of known molecular-mechanical force signatures that I propose building.

5.3 Long term vision

The cytoskeleton is extensively coupled, mechanically and chemically, to all organelles within a cell and many, if not all, signaling networks within a cell [54]. Given such coupling it is expected that many subtle changes within a cell will be reflected in subtle changes in cellular mechanics and force dynamics. High resolution force monitoring of cell mechanics with SCPFM has significant potential for studying and monitoring many aspects of a cell's physiology because of the extensive coupling between the cytoskeleton and the rest of the cell. It also has potential to advance the discovery and development of pharmaceuticals. Real-time cytoskeleton monitoring, with molecular or near-molecular sensitivity,

enabled by SCPFM, could be used for high-content phenotypic screening of pharmaceuticals with far greater sensitivity than existing technologies [263], which should have a dramatic impact by helping detect subtle side effects early in the drug discovery process. In addition to broad screening techniques, SCPFM may aid in the development and refinement of specific treatments for diseases that are related to cytoskeleton regulation such as treating cancer by preventing metastasis or cell division – e.g., refining taxol related compounds – as well as cardiovascular disease and others [264].

5.3.1 High-density, high-throughput pharmaceutical screening

High Content Screening (HCS) and High Throughput Screening (HTS) are closely related methods of scientific experimentation widely used in drug discovery. Both rely on using screening assays against large libraries of compounds [263]. HTS refers to the automation required to perform millions of experiments in parallel, while HCS refers to the complexity of the assay, particularly assays that are defined spatially and temporally in the context of the structural and functional integrity of each individual cell within an array of cells [265]. Existing HTS/HCS systems are large, robotic and expensive. Microfluidics is a promising technology for further streamlining, automating and reducing reagent consumption within HTS/HCS and numerous efforts have begun in this direction [266, 267]. Fluorescence imaging is the standard for data extraction used in almost all HTS/HCS systems [268-270].

Mechanical response is used as an assay in drug discovery through tissue constructs which monitor the contraction of large populations of cells [271, 272]. There are, however, numerous key differences between using tissue constructs and NEMS force sensors for phenotypic screening. Tissue constructs operate on large populations of cells. This presents an advantage in that a single experiment is already working with a statistically significant population of cells; however, the result is a low resolution, coarsely averaged response. Subtle effects, especially negative side effects, may be missed. Another drawback of tissue constructs is that they are slow to form and grow: three days to a week are typically needed to

prepare cells for a screening test. Tissue constructs are also quite large compared to NEMS force sensors; as such they require relatively large quantities of reagents (mili-Liters versus nano-Liters) and are not amenable to large scale integration/automation nor to simultaneous fluorescent microscopy, and thus are not useful for HTS/HCS. SCPFM, however, can be automated, integrated with microfluidics and applied in large arrays, and thus offers a promising route to extract richer data than existing HTS/HCS systems [273].

The basic application of NEMS force sensors to phenotypic screening goes as follows: first, cells are allowed to adhere to the force sensor and a baseline measurement of cellular force is obtained. Then cells are exposed to one or more potential pharmaceutical reagents, introduced in a carefully controlled manner using the integrated micro-fluidics, and the effects of the reagent/s on the force exerted by the cell is monitored. Since the cytoskeleton couples to so many aspects of a cell's physiology, the force provides a broad but highly sensitive measure of affect by the reagent/s. Fluorescent microscopy can be performed in parallel, thus SCPFM can be compatible and complimentary to existing screening methods. The principle advantage of NEMS force sensors for phenotypic screening is the high sensitivity to perturbations of the cellular cytoskeleton. This means that NEMS force sensors will be sensitive to subtle effects of potential pharmaceutical reagents that other screening methods will miss. This offers the potential to detect subtle side effects before costly clinical trials as well as the potential to detect subtle activity that is desired in potential pharmaceuticals.

Appendix 1: Beam deflection derivation

For a long rod, $L \gg w, t$, with moment of inertia I , Young's modulus E , that is bent in a small deflection by a force per length F_L in the y direction and stretched by a force G in the x direction the deflection of the neutral centerline of the rod in the y direction is determined by the equation of equilibrium:

$$IE \frac{d^4}{dx^4} \Delta Y(x) - G \frac{d^2}{dx^2} \Delta Y(x) + F_L = 0. \quad (\text{A3-1})$$

When the applied force is a point force, it is easier to work with the shearing force F_{sh} , and integration of equation (A3-1) achieves this:

$$IE \frac{d^3}{dx^3} \Delta Y(x) - G \frac{d}{dx} \Delta Y(x) + F_{sh} = 0. \quad (\text{A3-2})$$

The first case I will treat is a doubly clamped beam with no tension and a point force F applied at the midpoint. So, I solve equation (A3-2) with $T = 0$ and $f = F/2$ over the range $0 \leq x \leq L/2$ because the beam's deflection will be symmetric around $x = L/2$. The boundary conditions are $\Delta Y(x=0) = \Delta Y(x=L/2) = 0$. Thus, equation (A3-2) reduces to

$$\frac{d^3}{dx^3} \Delta Y(x) = -\frac{F}{2EI}. \quad (\text{A3-3})$$

I integrate equation (A3-3) twice to get

$$\frac{d}{dx} \Delta Y(x) = -\frac{F}{4EI} x^2 + ax + b, \quad (\text{A3-4})$$

then apply boundary conditions $\Delta Y(x=0) = \Delta Y(x=L/2) = 0$ to determine a and b :

$$\frac{d}{dx} \Delta Y(x) = F \frac{Lx - 2x^2}{8EI}. \quad (\text{A3-5})$$

A final integration and the last boundary condition, $\Delta Y(x=0) = 0$, yields the solution:

$$\Delta Y(x) = F \frac{x^2(3L - 4x)}{48EI}. \quad (\text{A3-6})$$

The second case is a doubly clamped beam with tension from a force G and a point force F applied at the midpoint. The conditions are identical to the first case except $G \neq 0$. Equation (A3-2) becomes

$$IE \frac{d^3}{dx^3} \Delta Y(x) - G \frac{d}{dx} \Delta Y(x) = -\frac{F}{2}. \quad (\text{A3-7})$$

By inspection, the first derivative must be of the form

$$\frac{d}{dx} \Delta Y(x) = \frac{F}{2G} + a \text{Cosh}(kx) + b \text{Sinh}(kx), \quad (\text{A3-8})$$

$$k^2 = \frac{G}{EI}.$$

I integrate equation (A3-8) to get

$$\Delta Y(x) = \frac{F}{2G} x + \frac{a}{k} \text{Sinh}(kx) + \frac{b}{k} \text{Cosh}(kx) + c. \quad (\text{A3-9})$$

Next apply boundary conditions $\Delta Y(x=0) = \Delta Y'(x=0) = \Delta Y'(x=L/2) = 0$ to determine a , b and c and thus the solution for the deflection of the center line is

$$\Delta Y(x) = \frac{F}{2G} \left(x - \frac{1}{k} \text{Sinh}(kx) + \frac{\text{Cosh}\left(\frac{kL}{2}\right) - 1}{k \text{Sinh}\left(\frac{kL}{2}\right)} (\text{Cosh}(kx) - 1) \right). \quad (\text{A3-10})$$

Appendix 2: All-polymer fabrication process details

- I. Sacrificial Cr/Au/Cr layer
 - a. 3" test grade wafer, single side polished
 - b. ebeam evaporator, $P < 2 \times 10^{-6}$ T
 - i. 10Å Ti
 - ii. 500Å Au (tantalum crucible)
 - iii. 500Å Cr
- II. Alignment Marks I: Photo lithography
 - a. Photo lithography
 - i. 180C 5 min
 - ii. Spin Az5124e
 1. 300/20/84
 2. 5000/60/10k
 - iii. Bake 95C 5 min
 - iv. Expose MA6 2s "Alignment 03" vacuum-contact mode
 - v. Bake 115C 2 min
 - vi. Expose MJB-3 80s flood
 - vii. Develop MIF 327 60s
 - viii. Stop h2o
 - ix. Dry N2
 - b. EBeam evaporate, $P < 2 \times 10^{-6}$ T
 - i. 25Å (on TM) Cr
 - ii. 2000Å (on TM) Au
 - c. Liftoff
 - i. ACE @ 65C ~ 10min
 - ii. Rinse ACE
 - d. Clean
 - i. ACE w/US 3 min
 - ii. IPA ~ 2 min
 - iii. Met ~ 1 min
 - iv. Dry N2
 - v. UVOC @ 100C 10min
- III. Su8 Layer 1: Beam Bottom
 - a. UVOC @ 65C 5 min
 - b. Spin Su8-2000.2
 1. 300/20/84
 2. 2000/60/10k
 - ii. Bake 95C 1 min
 - c. Expose MA6 (hard contact) 180s "Su8 Beams 2 – Su8 Beam Layer 3"
 - d. Quanta beamwrite
 - i. "Su8B4_0905_BB.RF6" (alignment mark set 1)
 - ii. HT=10KV, ss=2.0 (20-40pA), mag=350
 - iii. Dose = 5 μ C/cm²
 - iv. Target beam thickness: 200nm
 - e. Rest 60 minutes before developing
 - f. Develop Su8 developer 60s
 - i. Rinse ACE
 - ii. Rinse IPA
 - iii. Stop IPA
 - iv. Rinse MET
 - v. Dry N2

- g. Hardbake
 - i. 180C ~1hour
- IV. Metallization I: Piezoresistive Strain-Gauge
 - a. Spin AP300
 - i. 300/20/84
 - ii. 4000/60/252
 - b. Spin PMMA
 - i. Spin 495 A5
 - 1. 300/20/84
 - 2. 4000/60/10k
 - ii. Bake 180C 1 min
 - iii. Spin 950 A2
 - 1. 300/20/84
 - 2. 4000/60/10k
 - iv. Bake 180C 5 min
 - c. Quanta beamwrite
 - i. "Su8B4_0905_PZR.RF6" (alignment mark set 1)
 - ii. HT=30KV, ss=4.0 (400-600 pA), mag=350
 - iii. Dose = 550 $\mu\text{C}/\text{cm}^2$
 - d. Develop 3:1 IPA:MIBK 60s
 - i. Rinse IPA
 - ii. Dry N2
 - e. Ebeam Evaporate ($P_{\text{BASE}} < 2 \times 10^{-6}$ T)
 - i. 10 \AA Ti
 - ii. 300 \AA Au
 - iii. cool ~5 minutes before venting chamber
 - iv. target metal thickness: 30nm
 - f. Liftoff in TCE at RT
 - i. Soak overnight
 - ii. Agitate w/pipette to push metal away from sample
 - iii. Fresh TCE @ 65C 10 min
 - iv. Rinse ACE
 - g. Clean
 - i. ACE 3 min (in ultrasound)
 - ii. IPA 1 min
 - iii. Met 1 min
 - iv. N2 dry
 - h. Remove AP300
 - i. 10% BOE, ~5-8s
 - ii. Gently rinse with H2O
 - iii. N2 dry
- V. Su8 Layer 3: Beam Top
 - a. UVOC @ 65C 2 min
 - b. Spin Su8-2000.2
 - 1. 300/20/84
 - 2. 2000/60/10k
 - ii. Bake 95C 1 min
 - c. Quanta beamwrite
 - i. "Su8B4_0905_BT.RF6" (alignment mark set 2)
 - ii. HT=10KV, ss=2.0 (20-40 pA), mag=350
 - iii. Dose = 7 $\mu\text{C}/\text{cm}^2$
 - iv. Target beam thickness: 400nm total

- d. Rest 60 min
 - e. Develop Su8 developer 60s
 - i. Rinse ACE
 - ii. Rinse IPA
 - iii. Stop IPA
 - iv. Rinse MET
 - v. Dry N2
 - vi. Hard Bake: 180C ~1 hr
- VI. Metallization II: Cell Lamellipodium Pad
- a. Spin AP300
 - i. 300/20/84
 - ii. 4000/60/252
 - b. Spin PMMA
 - i. Spin 495 A5
 - 1. 300/20/84
 - 2. 4000/60/10k
 - ii. Bake 180C 1 min
 - iii. Spin 950 A2
 - 1. 300/20/84
 - 2. 4000/60/10k
 - iv. Bake 180C 5 min
 - c. Quanta beamwrite
 - i. "Su8B4_0822_PAD.RF6" (alignment mark set 2)
 - ii. HT=30KV, ss=4.0 (400-600 pA), mag=350
 - iii. Dose = 700 $\mu\text{C}/\text{cm}^2$
 - d. Develop 3:1 IPA:MIBK 60s
 - i. Rinse IPA
 - ii. Dry N2
 - e. Ebeam Evaporate ($P_{\text{BASE}} < 2 \times 10^{-6}$ T)
 - i. 10 Å Ti
 - ii. 300Å Au
 - iii. cool ~5 minutes before venting chamber
 - iv. target metal thickness: 30nm
 - f. Liftoff in TCE at RT
 - i. Soak overnight
 - ii. Agitate w/pipette to push metal away from sample
 - iii. Fresh TCE @ 65C 10 min
 - iv. Rinse ACE
 - g. Clean
 - i. ACE 5 min
 - ii. IPA 1 min
 - iii. Met 1 min
 - iv. Air dry
 - h. Remove AP300
 - i. 10% BOE, ~5-8s
 - ii. Gently rinse with H2O
 - iii. N2 dry
- VII. Metallization III: Conductors
- a. Photo lithography
 - i. *Check that spinner is clean & dry!! Have experienced PMGI adhesion trouble when PMMA residue is in spinner bowl.*
 - ii. Spin PMGI SF-9

1. 300/84/20
2. 3000/252/40
3. Bake 180C 1 min
- iii. Spin PMGI SF-9
 1. 300/84/20
 2. 3000/252/40
 3. Bake 180C 5 min
- iv. Spin Az5124e
 1. 300/84/20
 2. 5000/840/70
- v. Bake 95C 2 min
- vi. Expose MA6 hard contact 8s “Su8 Beams – Metal 04”
- vii. Bake 110C 2 min
- viii. Expose MJB-3 60s flood
- ix. Develop MF-CD 26 3 min (*develop immediately – do not wait overnight! 3 min exactly & do not agitate during development*)
- x. Stop h₂o
- xi. Dry N₂
- b. Ebeam Evaporate, $P_{\text{BASE}} < 1 \times 10^{-6}$ T
 - i. UVOC @ 65C 5 min
 - ii. Goal of 800nm, break into multiple evaps to avoid over heating.
 - iii. Repeat 4 times:
 1. 200nm Au at 2-4 Å/s
 2. wait ~60 min to cool and for pressure to drop: $P < 1 \times 10^{-6}$ T
 - iv. cool in evaporator 45 minutes after last evaporation
- c. Liftoff
 - i. Remover PG @ RT ~60 min
 - ii. Agitate w/pipette
 - iii. Remove metal with tweezers
 - iv. Fresh Remover PG ~ 10 min
- d. Clean
 - i. ACE 3 min
 - ii. IPA 1 min
 - iii. Met 1 min
 - iv. N₂ dry
- e. Softbake to remove liftoff solvent from Su8 without damaging gold
 - i. Ramp 20C → 150C @ 6C/hr and hold 36 hours
 - ii. Ramp 150C → 20C @ fast, turn off hotplate
- VIII. Su8 Layer 3: Well – thin/adhesion layer
 - a. UVOC @ 65C 2 min
 - b. In Watson 173:
 - i. Spin Su8-2000.5
 1. 300/84/30
 2. 1000/60/252
 - ii. Soft Bake 95C 1min
 - iii. Expose MA6 8s “Su8 Beams – Su8 Well 04”
 - iv. Post exposure bake
 1. 95C 1 min
 - v. Develop Su8 developer 1 min
 - vi. Rinse ACE
 - vii. Rinse IPA
 - viii. Stop IPA

- ix. Rinse ETOH
- x. Dry N₂
- IX. Su8 Layer 3: Well – thick
 - a. In Watson 173:
 - i. Spin Su8-2050
 - 1. 400/84/30
 - 2. 2000/60/10k
 - ii. Rest 60 min
 - iii. Soft Bake (9/11 9a)
 - 1. Ramp RT → 35C 5min
 - 2. Ramp 35C → 45C 5min
 - 3. Ramp 45C → 55C 240min
 - 4. auto shutoff & cool to room temp
 - iv. Expose MA6 55s “Su8 Beams – Su8 Well 05” (9/11 5p)
 - v. Rest overnight
 - vi. Post exposure bake
 - 1. Ramp RT → 40C 10min
 - 2. Ramp 40C → 55C 10min
 - 3. Ramp 55C → 65C 120min
 - 4. auto shutoff & cool to room temp
 - vii. Develop Su8 developer 2 min
 - viii. Rinse ACE
 - ix. Rinse IPA
 - x. Stop IPA
 - xi. Rinse ETOH
 - xii. Dry N₂
 - xiii. Check with scope to confirm developing is complete! Develop longer if necessary.
 - xiv. Target SU-8 thickness: 60-80 μm
 - b. Hardbake
 - i. Ramp 20C → 95C 4 hrs @ 100C/hr
 - ii. Ramp 95C → 20C @ 100C/hr
- X. Release
 - a. Wet, including wells
 - i. Immerse in ETOH
 - 1. Confirm vias are wet
 - ii. Quickly transfer to water
 - 1. Confirm with scope that wells are still wet
 - b. Etch
 - i. Quickly transfer to Cr etchant
 - 1. confirm that beams release ok
 - ii. Etch
 - 1. should take 6-7 hours if stresses optimally balanced
 - c. Clean
 - i. Immerse H₂O in CPD holder
 - 1. use CPD holder top that allows curling
 - ii. Immerse H₂O in CPD holder
 - iii. Immerse IPA in CPD holder
 - iv. Tousimis CPD with 20 min purge
- XI. Adhere to Glass Substrate
 - a. Prep glass slide
 - i. No. 1 cover glass, 18, 22 or 25mm square

- ii. sping 10:1 PDMS
 - 1. 6000/60/15
- iii. bake 80C 25 min
- b. Apply beams to PDMS using stamp
- c. Softbake (hotplate with cover)
 - i. Preserve beams, but not cells:
 - 1. Ramp 20C \rightarrow 80C @ 5C/hr overnight
 - 2. Ramp 80 \rightarrow 20C @ 5C/hr
 - ii. Preserve cells, but not beamss:
 - 1. Ramp 20C \rightarrow 120C @ 5C/hr hold at temp 48+ hours
 - 2. Ramp 120 \rightarrow 20C @ 5C/hr

Appendix 3: Silicon nitride membrane fabrication process details

- I. Metallization I: Alignment Marks
 - a. Photo lithography
 - i. HMDS vapor prime
 - ii. Spin Az5124e
 1. 300/20/84
 2. 5000/60/10k
 - iii. Bake 95C 5 min
 - iv. Expose MA6 2s “Alignment 04” low- vacuum-contact mode
 - v. Bake 115C 2 min
 - vi. Expose MA6 10s flood
 - vii. Develop CD-26 50s
 - viii. Stop h2o
 - ix. Dry N2
 - b. Electron beam evaporate: $P \sim 3 \times 10^{-7}$ T
 - i. 20Å (on TM) Ti
 - ii. 800Å (on TM) Au
 - c. Liftoff
 - i. ACE @ RT 1 hr
 - ii. Rinse ACE
 - d. Clean
 - i. ACE w/US 3 min
 - ii. IPA ~ 2 min
 - iii. Met ~ 1 min
 - iv. Dry N2
 - v. UVOC @ 100C 10min
- II. Metallization II: Cell PAD
 - a. Spin PMMA
 - i. Spin 495 A5
 1. 300/20/84
 2. 4000/60/2k
 - ii. Bake 180C 1 min
 - iii. Spin 950 A2
 1. 300/20/84
 2. 4000/60/2k
 - iv. Bake 180C 5 min
 - b. EBPG beamwrite
 - i. “LAYOUT-PAD-0307.COM”
 - ii. beam: 54na
 - iii. Dose = 1100 $\mu\text{C}/\text{cm}^2$
 - c. Develop 3:1 IPA:MIBK 60s
 - i. Rinse IPA
 - ii. Dry N2
 - d. Ebeam Evaporator – ($P_{\text{BASE}} \sim 8 \times 10^{-7}$ T)
 - i. 20Å Ti (4Å on TM#5; from carbon crucible)
 - ii. 275Å Au (250Å on TM#5; from tungsten boat)
 - iii. cool ~10 minutes before venting chamber
 - e. Liftoff in TCE
 - i. TCE @ RT overnight
 - ii. Rinse TCE
 - f. Clean

- i. ACE 3 min (in ultrasound)
 - ii. ACE 1 min
 - iii. IPA 1 min
 - iv. Met 1 min
 - v. N2 dry
 - vi. UVOC @ 100C 5 min
- III. Polymer I: Beam Top
 - a. Optional quick clean:
 - i. Rinse ETOH
 - ii. N2 dry
 - iii. 120C ~ 5min
 - b. Wafers A & B: Spin SU-8 3005
 - i. Spin 14:1 Su8-3005 – (140nm formulation)
 - 1. 300/20/84
 - 2. 3000/60/1k
 - ii. Bake 95C 2 min
 - iii. Expose MA6 20s flood
 - iv. Bake 95C 2 min
 - v. Develop Su8 developer 60s
 - 1. Rinse ACE
 - 2. Rinse IPA
 - 3. Stop IPA
 - 4. Rinse MET
 - 5. Dry N2
 - vi. Hardbake
 - 1. 95C → 180C Watson Hotplate ~ 2 hour
- IV. Metallization III: Piezoresistive Strain-Gauge
 - a. Spin AP300
 - i. 300/20/84
 - ii. 4000/60/252
 - b. Spin PMMA
 - i. Spin 495 A5
 - 1. 300/20/84
 - 2. 4000/60/10k
 - ii. Bake 180C 1 min
 - iii. Spin 950 A2
 - 1. 300/20/84
 - 2. 4000/60/10k
 - iv. Bake 180C 5 min
 - c. Height error work around: Ebeam Evaporate ($P_{BASE} 7 \times 10^{-7} T$)
 - i. 80Å Cr (30Å on TM#5; from carbon crucible)
 - ii. cool ~5 minutes before venting chamber
 - d. EBPG beamwrite
 - i. "LAYOUT-PZR-0307.COM"
 - ii. beam: 5na1
 - iii. Dose = 1150 $\mu C/cm^2$
 - iv. **slight increase in dose to compensate for Cr layer.*
 - e. Develop 3:1 IPA:MIBK 60s
 - i. Rinse IPA
 - ii. Dry N2
 - f. Ebeam Evaporate ($P_{BASE} 2 \times 10^{-7} T$)
 - i. 10 Cr (monitor read: 4 Å on film 5) (from carbon crucible)

- ii. 500Å Au (monitor read: 400 Å on film 5) (from tungsten boat)
 - iii. cool ~10 minutes before venting chamber
 - 1. *Check film setting!!!!!!!!!!!!!!!!!!!!!!*
 - g. Liftoff in TCE
 - i. TCE @ RT overnight
 - ii. Rinse TCE
 - h. Clean
 - i. ACE 3 min (in ultrasound)
 - ii. IPA 1 min
 - iii. Met 1 min
 - iv. N2 dry
 - i. Remove AP300
 - i. 1% BOE 10s – careful not to over etch!!
 - ii. Gently rinse with H2O
 - iii. N2 dry
- V. Polymer II: Beam Bottom
 - a. Wafers A & B: Spin SU-8 3005
 - i. UVOC 65C 2min
 - ii. Spin 14:1 Su8-3005 – (140nm formulation)
 - 1. 300/20/84
 - 2. 3000/60/1k
 - iii. Bake 95C 2 min
 - iv. Expose MA6 20s flood
 - v. Bake 95C 2 min
 - vi. Develop Su8 developer 60s
 - 1. Rinse ACE
 - 2. Rinse IPA
 - 3. Stop IPA
 - 4. Rinse MET
 - 5. Dry N2
 - vii. Hardbake
 - 1. 95C → 180C Watson Hotplate ~ 2 hour
- VI. Etch Pattern Beams
 - a. Rinse ETOH
 - b. Dry 120C ~5min
 - c. Spin AP300
 - i. 300/20/84
 - ii. 4000/60/252
 - d. Spin PMMA
 - i. Spin 495 A5
 - 1. 300/20/84
 - 2. 4000/60/10k
 - ii. Bake 180C 1 min
 - iii. Spin 950 A2
 - 1. 300/20/84
 - 2. 4000/60/10k
 - iv. Bake 180C 5 min
 - e. Height error work around: Ebeam Evaporate ($P_{\text{BASE}} = 7 \times 10^{-7}$ T)
 - i. 80Å Cr (30Å on TM#5; from carbon crucible)
 - ii. cool ~5 minutes before venting chamber
 - f. EBPG beamwrite
 - i. “LAYOUT-BEAM-0307.COM”

- ii. 53na beam
 - iii. Dose = 1200 $\mu\text{C}/\text{cm}^2$
 - iv. **slight increase in dose to compensate for Cr layer.*
 - g. Develop 3:1 IPA:MIBK 60s
 - i. Rinse IPA
 - ii. Dry N2
 - h. Evaporate ($P_{\text{BASE}} \sim 2 \times 10^{-7}$ T)
 - i. 300Å Ti (75Å on TM#5; carbon crucible)
 - 1. *It is critical that there be NO cracks in the mask layer!*
 - ii. profilometer:
 - i. Liftoff in TCE
 - i. TCE RT overnight
 - ii. Rinse TCE
 - j. Clean
 - i. ACE 3 min (in ultrasound)
 - ii. IPA 1 min
 - iii. Met 1 min
 - iv. N2 dry
 - k. MicroRIE polymer etch
 - i. CF4 & O2
 - 1. O2 30 sccm
 - 2. CF4 7 sccm
 - 3. power 5%
 - 4. 140s
 - ii. O2 only – without breaking vacuum
 - 1. O2 30 sccm
 - 2. power 5%
 - 3. 120s
 - a. B: 3min O2, break vac check under scope, 2.5min more.
 - b. C: 2 min O2, break vac check under scope, 1min more.
 - iii. confirm with AFM – skip AFM has trouble, visually very good.
 - l. Remove metal etch mask
 - i. Chrome mask:
 - 1. Cr etchant (CR-7S) ~2min
 - 2. Gently rinse with H2O
 - ii. Ti mask:
 - 1. 10% BOE – 30s
 - 2. Gently since with H2O
 - m. Remove AP300
 - i. 1% BOE 10s – careful not to over etch!!
 - ii. Gently rinse with H2O
 - iii. N2 dry
 - n. Clean
 - i. ACE 3 min (in ultrasound)
 - ii. IPA 1 min
 - iii. Met 1 min
 - iv. N2 dry
- VII. Metallization V: Conductors
- a. Photo lithography
 - i. *Check that spinner is clean & dry!! Have experienced PMGI adhesion trouble when PMMA residue is in spinner bowl.*
 - ii. Spin PMGI SF-9

1. 300/84/20
 2. 3000/252/40
 3. Bake 190C 5 min
 - iii. Spin Az5124e
 1. 300/84/20
 2. 3000/840/70
 - iv. Bake 95C 2 min
 - v. Expose MA6 hard contact 8s “PB01 – Metal 05”
 - vi. Bake 115C 2 min
 - vii. Expose MA6 10s flood
 - viii. Develop MF-CD 26 4 min (*develop immediately – do not wait overnight! 3 min exactly & do not agitate during development*)
 - ix. Stop h2o
 - x. Dry N2
 - xi. MicroRie: 30sccmO2, 7sccmCF4, 10% pw, 15s.
 - b. Ebeam Evaporate ($P_{\text{BASE}} < 3 \times 10^{-7}$ T)
 - i. 20 Cr (8Å on TM#5; tungsten boat)
 - ii. 5000Å Au (monitor read: 45000 Å on film 5) (from tungsten boat)
 1. 1-3 Å/s
 - iii. cool ~45 minutes before venting chamber
 - c. Liftoff
 - i. Remover PG 3 hours
 - ii. Agitate with pipette
 - iii. Ultra sound 1 min
 - iv. Back into Remover PG 1 hour more
 - v. Fresh Remover PG ~ 2 min
 - d. Clean
 - i. ACE 3 min w/US
 - ii. IPA 1 min
 - iii. Met 1 min
 - iv. N2 dry
 - e. Remove Au defects
 - i. Au etchant applied with q-tip ~10min
 - ii. Rinse H2O
 - iii. Dry N2
- VIII. KOH Etch-Mask Pattern
- a. Etch Mask – MicroRIE
 - i. Vapor deposit AP001 2 min
 - ii. Spin Az9245
 1. 3000/60/1000
 - iii. bake 110C 2 min
 - iv. Expose MA6 Hard Contact (PB1_WinMemb02_590) 60s
 - a. PR is getting old, higher dose to compensate (previously 44s)
 2. BSA alignment objective placement:
 3. Left: (24.42, 50.66)
 4. Right: (21.94, 50.31)
 5. (*don't forget the pedal!!!*)
 - v. Develop Az400 4:1 4min
 - vi. Stop H2O
 - vii. N2 Dry
 - b. Etch Mask – KOH
 - i. MicroRIE SiN etch

1. O₂ 3.5 sccm
 2. CF₄ 25 sccm
 3. power 15% (~100mW)
 - a. time: 4min
 - ii. Rinse ACE
 - iii. ACE w/US 3 min
 - iv. Rinse ACE
 - v. Rinse IPA
 - vi. Rinse MET
 - vii. N₂ dry
- IX. KOH Etch
- a. Remove oxide from KOH windows (*If time has passed since etch mask patterning*)
 - i. MicroRIE SiN etch
 1. O₂ 3.5 sccm
 2. CF₄ 25 sccm
 3. power 15% (~100mW)
 4. time: 15s
 - b. KOH solution:
 - i. 1kG KOH pellets, 2.5L water
 - ii. 85C probe temp
 - iii. 250rpm stirbar; preferably using bi-directional stirrer.
 - iv. 4 hours to clear Si.
 - c. Additional etch time as necessary until window to alignment marks.
 - i. Assume lateral etch rate of 8um/hour
- X. Beam Release
- a. MicroRIE SiN etch:
 - i. O₂ 3.5 sccm
 - ii. CF₄ 25 sccm
 - iii. power 10% (~80W)
 - iv. 140s
 - b. MicroRIE SiN Selective etch:
 - i. CF₄ 10 sccm
 - ii. Power 10%
 - iii. 10-60s intervals until membranes grey/white; rotate wafers to improve uniformity.
 1. deep blue ~ 90s
 2. red/purple ~ 60s
 3. pea green ~ 40s
 4. yellow/grey ~20s
 - c. Selective wet etch release:
 - i. Wet in H₂O.
 - ii. 0.1% HF @ 80C
 1. Facedown
 2. stir/agitate by pipetting HF into via regions every 20 min
 3. 2 hours
 - iii. Rinse H₂O.
 - d. Critical Point Dry
 - i. Soak H₂O
 - ii. Soak IPA
 - iii. Critical Point Dry:
 1. single wafer: 20min purge. (wafer facing down)
 2. double wafer: 30min purge.

- e. Check resistance of each device on probe station.
 - f. Dice
- XI. Adhere to Glass Substrate
- a. Prep glass slide
 - i. No. 1 cover glass 22 or 25mm square
 - ii. sping 10:1 PDMS
 - 1. 6000/60/15
 - iii. bake 80C 25 min
 - iv. apply to PDMS with tweezers.
 - v. Bake: 80C overnight.

Appendix 4: Microfluidics fabrication process molds

Incubator Layer Mold

Layer 1: humidity & CO₂ lines

Su8-2005 300/20/84
 1000/60/1k

65C 2 min

95C 5 min

MJB-3: 2.5min, *FC20_Inc20 CAS02*

65C 1 min

95C 3 min

Su8 Dev ~15 sec

rinse ACE

rinse IPA

stop IPA

hard bake 180C 2 hours

Flow Layer Mold

Layer 1: high resistance flow lines

Su8-2005 300/20/84
 1000/60/1k

65C 2 min

95C 5 min

MA6: 24s, *FC20 Flow SU8 10um 2*

65C 1 min

95C 3 min

Su8 Dev ~20 sec

rinse ACE

rinse IPA

stop IPA

hard bake ~ 1 hour

layer 2: flow

hmds prime

Az50 300/30/84
 1000/60/1k

rest ~2 min

65C 2 min (no petri dish)

115C 8 min

65C 2 min

cool 5+ min

MA6: 80s, *FC20_Flow2 - az50 4layer*dev in 3:1 h₂o:2401 for 5 minstop h₂o

hard reflow bake: 20C → 200C @ 180C/hr, hold 4 hours, 200C → 20C @ 180C/hr

layer 3: leaks & vias

Su8-2025 400/30/84
 1600/60/252

65C 2 min

95C 5 min

MA6: 28s, *FC20_Flow SU8 - 30u 2*

65C 2 min

95C 4 min

Su8 Dev 1½ min
 rinse ACE
 rinse IPA
 stop IPA
 hard bake 2 hour 180C

Control Layer Mold

Layer 1: lines

Su8-2010 300/20/84
 2000/60/1k

 65C 2 min
 95C 5 min
 MA6: 24s, *FC20 Control1 – 10u*
 65C 1 min
 95C 3 min
 Su8 Dev ~20 sec
 rinse ACE
 rinse IPA
 stop IPA
 hard bake 180C 2 hours

Layer 2: valves

Su8-2025 300/20/84
 2500/60/252

 rest ~5 min
 65C 2 min
 95C 5 min
 MA6: 20s, *FC20_Control25um3*
 (5" IronOx mask)
 65C 1 min
 95C 3 min
 Su8 Dev 2-3 min
 rinse ACE
 rinse IPA
 stop IPA
 hard bake 180C 2 hours

Layer 3: vias

Su8-2050 400/30/84
 1600/60/252

 rest ~5 min
 65C 5 min
 95C 12 min
 MA6: 44s, *FC20_Control3 – 60u*
 65C 5 min
 95C 8 min
 Su8 Dev 4 min
 rinse ACE
 rinse IPA
 stop IPA
 N2 dry
 hard bake 180C 2 hours

Base Layer Mold

Layer 1: flow

Su8-5 300/20/84
1000/60/10k
65C 2 min
95C 5 min
MA6: 16s, *FC20_Base1a - 10u*
65C 1 min
95C 3 min
Su8 Dev 1 min
rinse ACE
rinse IPA
stop IPA
hard bake ~ 1 hour

Layer 2: vias

Su8-2025 300/20/84
2000/60/252
rest ~5 min
65C 3 min
95C 6 min
MA6: 20s, *FC20_Base2 - 30u*
65C 2 min
95C 4 min
Su8 Dev 4 min
rinse ACE
rinse IPA
stop IPA
hard bake ~ 1 hour

Appendix 5: Microfluidics fabrication process soft lithography

Incubator Layer

5:1 (40g A : 8g B)
 mix: 1 min; de-foam: 5 min
 pour: 32.5g
 pump: 30 min
 bake 80C: 45min

Flow Layer

5:1 same batch as incubator
 350/60/10
 rest ~ 10min
 bake 80C: 20min
 cool ~ 8min
 20:1 (20g A : 1g B)
 2000/60/15
 bake 80C: 25min

Control Layer

25:1 (25.0g A : 1.0g B)
 mix: 2 min; de-foam: 2 min
 1300-1500/60/15
 1300 for Flow16
 1500 for Flow15
 rest: 60+ min
 bake 80C: 45min

Base Layer

30:1 (25.0g A: 1.0g B)
 mix: 2 min; de-foam: 2 min
 3000/60/15
 rest: 60+ min
 bake 80C: 45 min

Bake Incubator & Flow

Cut, tape & align

Bake 80C: Inc/Flow & control for 45 min

Cut, tape & align.

Bake 80C: Inc/Flow/Control for 60 min

Cut, punch with Schmidt press, tape & bake base; then align.

Bake 80C: Inc/Flow/Control/Base for 1-3hrs

Cut, dice, tape & align to substrate.

Bake 80C: Inc/Flow/Control/Base/substrate 36+ hours

Appendix 6: Additional dynamics data

(Figure 36)

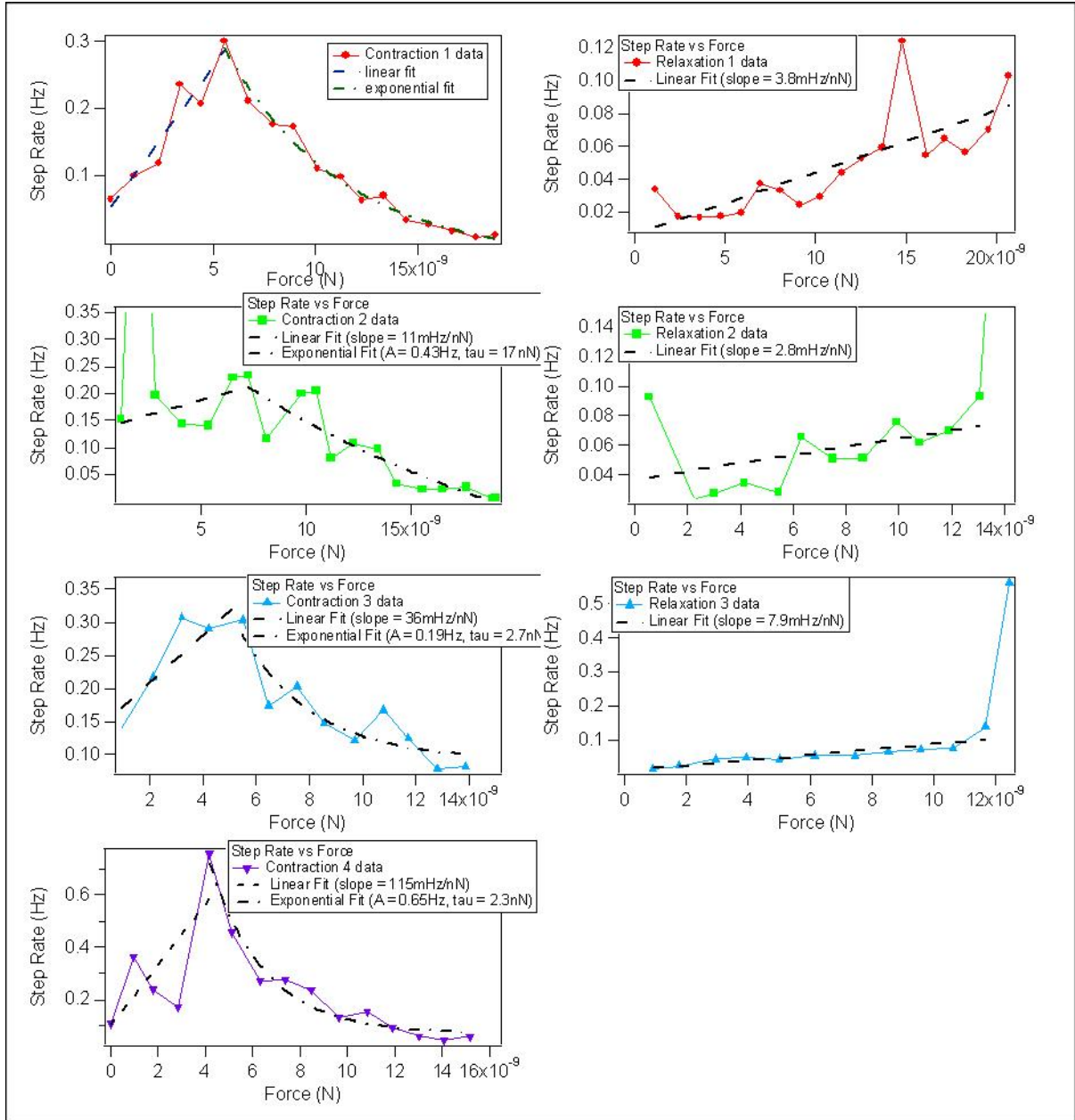


Figure 36. The complete data set of step rate versus force for the contraction and relaxation cycles.

(Figure 37)

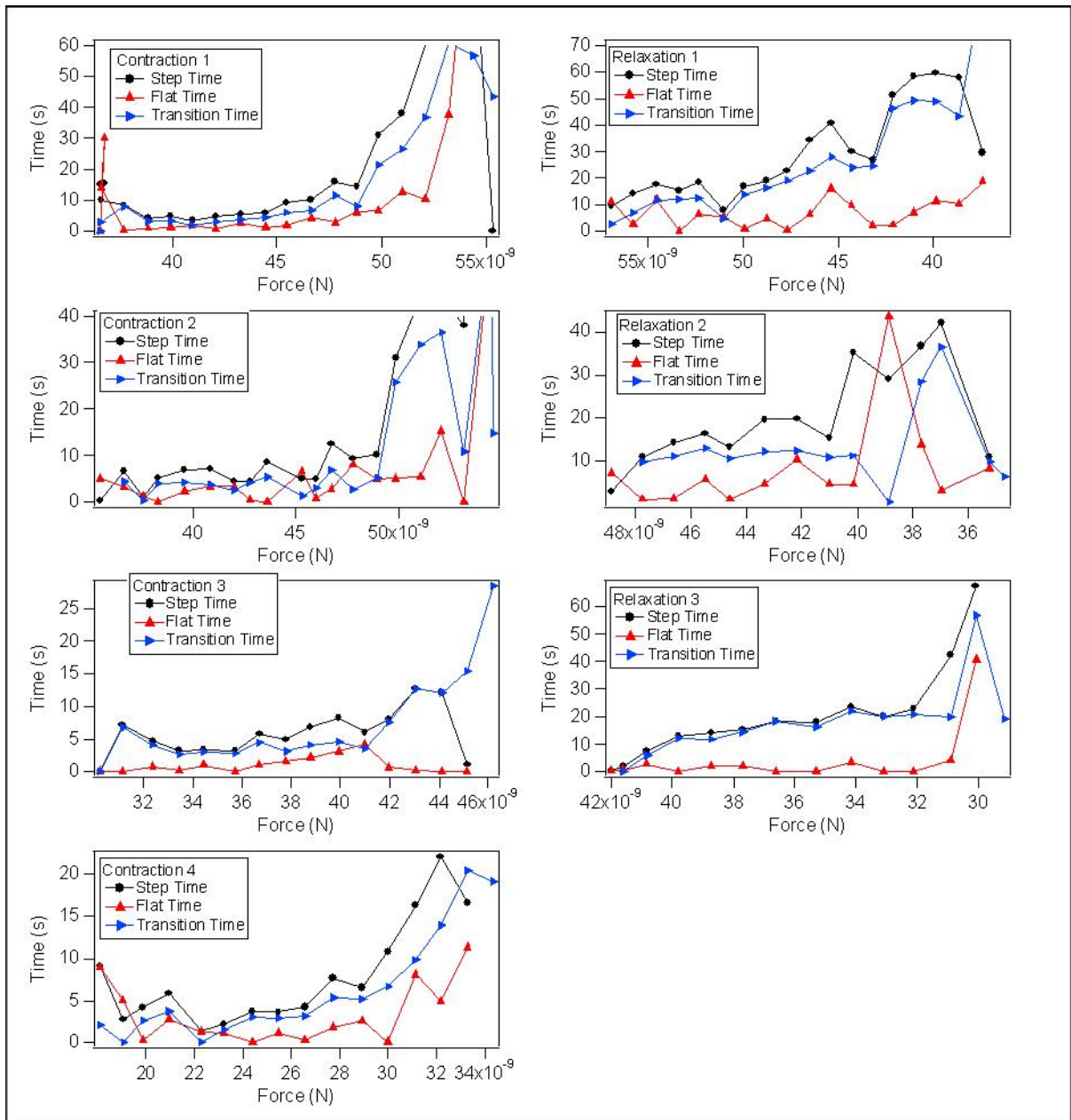


Figure 37. Step time, flat time and transition time (see Figure 34) for the contraction and relaxation cycles. I was looking for changes in the flat versus transition dynamics as a function of force, but nothing is jumping out at me.

1. Megason, S.G. and S.E. Fraser, *Imaging in systems biology*. Cell, 2007. 130: p. 784-795.
2. Tan, J.L., et al., *Cells lying on a bed of microneedles: An approach to isolate mechanical force*. Proceedings of the National Academy of Sciences of the United States of America, 2003. 100(4): p. 1484-1489.
3. Dembo, M., et al., *Imaging the traction stresses exerted by locomoting cells with the elastic substratum method*. Biophysical Journal, 1996. 70(4): p. 2008-2022.
4. Dembo, M. and Y.L. Wang, *Stresses at the cell-to-substrate interface during locomotion of fibroblasts*. Biophysical Journal, 1999. 76(4): p. 2307-2316.
5. Cross, S.E., et al., *Nanomechanical analysis of cells from cancer patients*. Nature Nanotechnology, 2007. 2(12): p. 780-783.
6. Jiang, G.Y., et al., *Two-piconewton slip bond between fibronectin and the cytoskeleton depends on talin*. Nature, 2003. 424(6946): p. 334-337.
7. Kress, H., et al., *Filopodia act as phagocytic tentacles and pull with discrete steps and a load-dependent velocity*. Proceedings of the National Academy of Sciences of the United States of America, 2007. 104(28): p. 11633-11638.
8. Hamill, O.P., et al., *IMPROVED PATCH-CLAMP TECHNIQUES FOR HIGH-RESOLUTION CURRENT RECORDING FROM CELLS AND CELL-FREE MEMBRANE PATCHES*. Pflügers Archiv-European Journal of Physiology, 1981. 391(2): p. 85-100.
9. Dunlop, J., et al., *High-throughput electrophysiology: an emerging paradigm for ion-channel screening and physiology*. Nature Reviews Drug Discovery, 2008. 7(4): p. 358-368.
10. Tehovnik, E.J., *Electrical stimulation of neural tissue to evoke behavioral responses*. Journal of Neuroscience Methods, 1996. 65(1): p. 1-17.
11. Pearce, T.M. and J.C. Williams, *Microtechnology: Meet neurobiology*. Lab on a Chip, 2007. 7(1): p. 30-40.
12. Born, M.a.W., E., *Principles of Optics*. 2002, Cambridge: Cambridge University Press.
13. Meiners, J.C. and S.R. Quake, *Direct measurement of hydrodynamic cross correlations between two particles in an external potential*. Physical Review Letters, 1999. 82(10): p. 2211-2214.
14. Batchelor, G.K., *BROWNIAN DIFFUSION OF PARTICLES WITH HYDRODYNAMIC INTERACTION*. Journal of Fluid Mechanics, 1976. 74(MAR9): p. 1-29.
15. Johnson, J.B., *Thermal agitation of electricity in conductors*. Physical Review, 1928. 32(1): p. 97-109.
16. Nyquist, H., *Thermal agitation of electric charge in conductors*. Physical Review, 1928. 32(1): p. 110-113.
17. Ekinici, K.L. and M.L. Roukes, *Nanoelectromechanical systems*. Review of Scientific Instruments, 2005. 76(6).
18. Hell, S.W., *Far-field optical nanoscopy*. Science, 2007. 316(5828): p. 1153-1158.
19. Lezec, H.J., J.A. Dionne, and H.A. Atwater, *Negative refraction at visible frequencies*. Science, 2007. 316(5823): p. 430-432.
20. Ryu, W., et al., *Open micro-fluidic system for atomic force microscopy-guided in situ electrochemical probing of a single cell*. Lab on a Chip, 2008. 8(9): p. 1460-1467.
21. Sims, C.E. and N.L. Allbritton, *Analysis of single mammalian cells on-chip*. Lab on a Chip, 2007. 7(4): p. 423-440.
22. Fraser, S.E. and R.M. Harland, *The molecular metamorphosis of experimental embryology*. Cell, 2000. 100(1): p. 41-55.
23. Weinberg, R.A., *One Renegade Cell: The Quest For The Origin Of Cancer*. 1998: Basic Books.
24. Suel, G.M., et al., *An excitable gene regulatory circuit induces transient cellular differentiation*. Nature, 2006. 440(7083): p. 545-550.

25. Rosenfeld, N., et al., *Gene regulation at the single-cell level*. Science, 2005. 307(5717): p. 1962-1965.
26. Wolf, S.a.T.R.N., *Silicon Processing for the VLSI Era*. 2 ed. 2000, Sunset Beach, CA: Lattice Press.
27. Li, M., H.X. Tang, and M.L. Roukes, *Ultra-sensitive NEMS-based cantilevers for sensing, scanned probe and very high-frequency applications*. Nature Nanotechnology, 2007. 2(2): p. 114-120.
28. Arlett, J.L., *Properties of piezoresistive silicon nano-scale cantilevers with applications to BioNEMS*, in *Physics*. 2006, California Institute of Technology: Pasadena, CA.
29. Jen, S.U., et al., *Piezoresistance and electrical resistivity of Pd, Au, and Cu films*. Thin Solid Films, 2003. 434(1-2): p. 316-322.
30. Balagadde, F.K., et al., *Long-term monitoring of bacteria undergoing programmed population control in a microchemostat*. Science, 2005. 309(5731): p. 137-140.
31. Gomez-Sjoberg, R., et al., *Versatile, fully automated, microfluidic cell culture system*. Analytical Chemistry, 2007. 79(22): p. 8557-8563.
32. Melin, J. and S.R. Quake, *Microfluidic large-scale integration: The evolution of design rules for biological automation*. Annual Review of Biophysics and Biomolecular Structure, 2007. 36: p. 213-231.
33. Thorsen, T., S.J. Maerkl, and S.R. Quake, *Microfluidic large-scale integration*. Science, 2002. 298(5593): p. 580-584.
34. Ingber, D.E., *Tensegrity I. Cell structure and hierarchical systems biology*. Journal of Cell Science, 2003. 116(7): p. 1157-1173.
35. Ingber, D.E., *Tensegrity II. How structural networks influence cellular information processing networks*. Journal of Cell Science, 2003. 116(8): p. 1397-1408.
36. Ingber, D.E., *Tensegrity-based mechanosensing from macro to micro*. Progress in Biophysics & Molecular Biology, 2008. 97(2-3): p. 163-179.
37. Chen, C.S., *Mechanotransduction - a field pulling together?* Journal of Cell Science, 2008. 121(20): p. 3285-3292.
38. Bershadsky, A., M. Kozlov, and B. Geiger, *Adhesion-mediated mechanosensitivity: a time to experiment, and a time to theorize*. Current Opinion in Cell Biology, 2006. 18(5): p. 472-481.
39. Paszek, M.J. and V.M. Weaver, *The tension mounts: Mechanics meets morphogenesis and malignancy*. Journal of Mammary Gland Biology and Neoplasia, 2004. 9(4): p. 325-342.
40. Polte, T.R., et al., *Extracellular matrix controls myosin light chain phosphorylation and cell contractility through modulation of cell shape and cytoskeletal prestress*. American Journal of Physiology-Cell Physiology, 2004. 286(3): p. C518-C528.
41. Ghosh, K., et al., *Cell adaptation to a physiologically relevant ECM mimic with different viscoelastic properties*. Biomaterials, 2007. 28(4): p. 671-679.
42. Lopez, J.I., J.K. Mouw, and V.M. Weaver, *Biomechanical regulation of cell orientation and fate*. Oncogene, 2008. 27(55): p. 6981-6993.
43. Bray, D., *Cell Movements: From Molecules to Motility*. 2nd ed. 2001, New York: Garland Publishing.
44. Lee, J., et al., *PRINCIPLES OF LOCOMOTION FOR SIMPLE-SHAPED CELLS*. Nature, 1993. 362(6416): p. 167-171.
45. Engler, A.J., et al., *Matrix elasticity directs stem cell lineage specification*. Cell, 2006. 126(4): p. 677-689.
46. Lo, C.M., et al., *Cell movement is guided by the rigidity of the substrate*. Biophysical Journal, 2000. 79(1): p. 144-152.
47. Ingber, D.E., *Mechanical control of tissue morphogenesis during embryological development*. International Journal of Developmental Biology, 2006. 50(2-3): p. 255-266.

48. Shraiman, B.I., *Mechanical feedback as a possible regulator of tissue growth*. Proceedings of the National Academy of Sciences of the United States of America, 2005. 102(9): p. 3318-3323.
49. Geiger, B. and A. Bershadsky, *Assembly and mechanosensory function of focal contacts*. Current Opinion in Cell Biology, 2001. 13(5): p. 584-592.
50. Bershadsky, A.D., N.Q. Balaban, and B. Geiger, *Adhesion-dependent cell mechanosensitivity*. Annual Review of Cell and Developmental Biology, 2003. 19: p. 677-695.
51. Vogel, V. and M. Sheetz, *Local force and geometry sensing regulate cell functions*. Nature Reviews Molecular Cell Biology, 2006. 7(4): p. 265-275.
52. Sawada, Y., et al., *Force sensing by mechanical extension of the Src family kinase substrate p130Cas*. Cell, 2006. 127(5): p. 1015-1026.
53. Chan, C.E. and D.J. Odde, *Traction Dynamics of Filopodia on Compliant Substrates*. Science, 2008. 322(5908): p. 1687-1691.
54. Janmey, P.A., *The cytoskeleton and cell signaling: Component localization and mechanical coupling*. Physiological Reviews, 1998. 78(3): p. 763-781.
55. Ingber, D.E., *Mechanobiology and diseases of mechanotransduction*. Annals of Medicine, 2003. 35(8): p. 564-577.
56. Pienta, K.J. and D.S. Coffey, *CELL MOTILITY AS A CHEMOTHERAPEUTIC TARGET*. Cancer Surveys, 1991. 11: p. 255-263.
57. de Bouard, S., et al., *Invasion of human glioma biopsy specimens in cultures of rodent brain slices: a quantitative analysis*. Journal of Neurosurgery, 2002. 97(1): p. 169-176.
58. Jordan, M.A. and L. Wilson, *Microtubules as a target for anticancer drugs*. Nature Reviews Cancer, 2004. 4(4): p. 253-265.
59. Small, J.V. and I. Kaverina, *Microtubules meet substrate adhesions to arrange cell polarity*. Current Opinion in Cell Biology, 2003. 15(1): p. 40-47.
60. Bershadsky, A., et al., *Involvement of microtubules in the control of adhesion-dependent signal transduction*. Current Biology, 1996. 6(10): p. 1279-1289.
61. Pollard, T.D., *RATE CONSTANTS FOR THE REACTIONS OF ATP-ACTIN AND ADP-ACTIN WITH THE ENDS OF ACTIN-FILAMENTS*. Journal of Cell Biology, 1986. 103(6): p. 2747-2754.
62. Pollard, T.D., *ASSEMBLY AND DYNAMICS OF THE ACTIN FILAMENT SYSTEM IN NONMUSCLE CELLS*. Journal of Cellular Biochemistry, 1986. 31(2): p. 87-95.
63. Pollard, T.D., *MECHANISM OF ACTIN FILAMENT SELF-ASSEMBLY AND REGULATION OF THE PROCESS BY ACTIN-BINDING PROTEINS*. Biophysical Journal, 1986. 49(1): p. 149-151.
64. Pelham, R.J. and Y.L. Wang, *Cell locomotion and focal adhesions are regulated by substrate flexibility*. Proceedings of the National Academy of Sciences of the United States of America, 1997. 94(25): p. 13661-13665.
65. Romer, L.H., K.G. Birukov, and J.G.N. Garcia, *Focal adhesions - Paradigm for a signaling nexus*. Circulation Research, 2006. 98(5): p. 606-616.
66. Geiger, B., et al., *Transmembrane extracellular matrix-cytoskeleton crosstalk*. Nature Reviews Molecular Cell Biology, 2001. 2(11): p. 793-805.
67. Calderwood, D.A., et al., *The talin head domain binds to integrin beta subunit cytoplasmic tails and regulates integrin activation*. Journal of Biological Chemistry, 1999. 274(40): p. 28071-28074.
68. Giancotti, F.G., *A structural view of integrin activation and signaling*. Developmental Cell, 2003. 4(2): p. 149-151.
69. Hynes, R.O., *Integrins: Bidirectional, allosteric signaling machines*. Cell, 2002. 110(6): p. 673-687.
70. Gilmore, A.P. and K. Burridge, *Regulation of vinculin binding to talin and actin by phosphatidylinositol-4-5-bisphosphate*. Nature, 1996. 381(6582): p. 531-535.

71. DeMali, K.A., C.A. Barlow, and K. Burridge, *Recruitment of the Arp2/3 complex to vinculin: coupling membrane protrusion to matrix adhesion*. Journal of Cell Biology, 2002. 159(5): p. 881-891.
72. Humphries, J.D., et al., *Vinculin controls focal adhesion formation by direct interactions with talin and actin*. Journal of Cell Biology, 2007. 179(5): p. 1043-1057.
73. Martel, V., et al., *Conformation, localization, and integrin binding of talin depend on its interaction with phosphoinositides*. Journal of Biological Chemistry, 2001. 276(24): p. 21217-21227.
74. Bjorge, J.D., A. Jakymiw, and D.J. Fujita, *Selected glimpses into the activation and function of Src kinase*. Oncogene, 2000. 19(49): p. 5620-5635.
75. Baneyx, G., L. Baugh, and V. Vogel, *Coexisting conformations of fibronectin in cell culture imaged using fluorescence resonance energy transfer*. Proceedings of the National Academy of Sciences of the United States of America, 2001. 98(25): p. 14464-14468.
76. Baneyx, G., L. Baugh, and V. Vogel, *Fibronectin extension and unfolding within cell matrix fibrils controlled by cytoskeletal tension*. Proceedings of the National Academy of Sciences of the United States of America, 2002. 99(8): p. 5139-5143.
77. Krammer, A., et al., *Forced unfolding of the fibronectin type III module reveals a tensile molecular recognition switch*. Proceedings of the National Academy of Sciences of the United States of America, 1999. 96(4): p. 1351-1356.
78. Krammer, A., et al., *A structural model for force regulated integrin binding to fibronectin's RGD-synergy site*. Matrix Biology, 2002. 21(2): p. 139-147.
79. Garcia, A.J. and N.D. Gallant, *Stick and grip - Measurement systems and quantitative analyses of integrin-mediated cell adhesion strength*. Cell Biochemistry and Biophysics, 2003. 39(1): p. 61-73.
80. Footer, M.J., et al., *Direct measurement of force generation by actin filament polymerization using an optical trap*. Proceedings of the National Academy of Sciences of the United States of America, 2007. 104(7): p. 2181-2186.
81. Laan, L., et al., *Force-generation and dynamic instability of microtubule bundles*. Proceedings of the National Academy of Sciences of the United States of America, 2008. 105(26): p. 8920-8925.
82. Finer, J.T., R.M. Simmons, and J.A. Spudich, *SINGLE MYOSIN MOLECULE MECHANICS - PICONEWTON FORCES AND NANOMETER STEPS*. Nature, 1994. 368(6467): p. 113-119.
83. Vogel, V., *Mechanotransduction involving multimodular proteins: Converting force into biochemical signals*. Annual Review of Biophysics and Biomolecular Structure, 2006. 35: p. 459-488.
84. Smith, M.L., et al., *Force-induced unfolding of fibronectin in the extracellular matrix of living cells*. Plos Biology, 2007. 5(10): p. 2243-2254.
85. Norman, J.J., et al., *Microsystems for biomechanical measurements*. Pediatric Research, 2008. 63(5): p. 576-583.
86. Addae-Mensah, K.A. and J.P. Wikswo, *Measurement techniques for cellular biomechanics in vitro*. Experimental Biology and Medicine, 2008. 233(7): p. 792-809.
87. Sniadecki, N.J., et al., *Magnetic microposts as an approach to apply forces to living cells*. Proceedings of the National Academy of Sciences of the United States of America, 2007. 104(37): p. 14553-14558.
88. Sabass, B., et al., *High resolution traction force microscopy based on experimental and computational advances*. Biophysical Journal, 2008. 94(1): p. 207-220.
89. Berns, M.W., *Optical tweezers: Tethers, wavelengths, and heat*, in *Laser Manipulation of Cells and Tissues*. 2007, Elsevier Academic Press Inc: San Diego. p. 457-466.
90. Solon, J., et al., *Fibroblast adaptation and stiffness matching to soft elastic substrates*. Biophysical Journal, 2007. 93(12): p. 4453-4461.

91. Giannone, G., et al., *Periodic lamellipodial contractions correlate with rearward actin waves*. Cell, 2004. 116(3): p. 431-443.
92. Giannone, G., et al., *Lamellipodial actin mechanically links myosin activity with adhesion-site formation*. Cell, 2007. 128(3): p. 561-575.
93. Zimerman, B., T. Volberg, and B. Geiger, *Early molecular events in the assembly of the focal adhesion-stress fiber complex during fibroblast spreading*. Cell Motility and the Cytoskeleton, 2004. 58(3): p. 143-159.
94. Cavalcanti-Adam, E.A., et al., *Cell spreading and focal adhesion dynamics are regulated by spacing of integrin ligands*. Biophysical Journal, 2007. 92(8): p. 2964-2974.
95. Danuser, G. and C.M. Waterman-Storer, *Quantitative fluorescent speckle microscopy: where it came from and where it is going*. Journal of Microscopy-Oxford, 2003. 211: p. 191-207.
96. Waterman-Storer, C.M. and G. Danuser, *New directions for fluorescent speckle microscopy*. Current Biology, 2002. 12(18): p. R633-R640.
97. Vallotton, P., et al., *Simultaneous mapping of filamentous actin flow and turnover in migrating cells by quantitative fluorescent speckle microscopy*. Proceedings of the National Academy of Sciences of the United States of America, 2004. 101(26): p. 9660-9665.
98. Ponti, A., et al., *Periodic patterns of actin turnover in Lamellipodia and lamellae of migrating epithelial cells analyzed by quantitative Fluorescent Speckle Microscopy*. Biophysical Journal, 2005. 89(5): p. 3456-3469.
99. Roukes, M.L., Chung, F.W., Lee, W., Tang, H.X., Axelrod, B.W. and Tan, J.L., *Polymer NEMS for cell physiology and microfabricated cell positioning system for micro-biocalorimeter*, U.S.P. Office, Editor. 2007: United States of America.
100. Landau, L.D.a.L.E.M., *Theory of Elasticity*. 3 ed. Course of Theoretical Physics. 1959, Oxford: Butterworth-Heinemann.
101. Arlett, J.L., et al., *Self-sensing micro- and nanocantilevers with attonewton-scale force resolution*. Nano Letters, 2006. 6(5): p. 1000-1006.
102. Thaysen, J., et al., *Polymer-based stress sensor with integrated readout*. Journal of Physics D-Applied Physics, 2002. 35(21): p. 2698-2703.
103. Diaz Cuenca, A., et al. *Comparison of microstrain indicators measurements based on Anderson's Loop and Wheatstone Bridge*. in *Electronics, Communications and Computers, 2006. CONIELECOMP 2006. 16th International Conference on*. 2006.
104. Horowitz, P.a.H., W., *The Art of Electronics*. 2 ed. 1980, New York: Cambridge University Press.
105. Boisen, A., et al., *Environmental sensors based on micromachined cantilevers with integrated read-out*. Ultramicroscopy, 2000. 82(1-4): p. 11-16.
106. Hooge, F.N., *1/F NOISE IS NO SURFACE EFFECT*. Physics Letters A, 1969. A 29(3): p. 139-&.
107. Johansson, A., et al., *Temperature effects in Au piezoresistors integrated in SU-8 cantilever chips*. Journal of Micromechanics and Microengineering, 2006. 16(12): p. 2564-2569.
108. Kasap, S.O., *Principles of Electronic Materials and Devices*. 2nd ed. 2002, New York: McGraw-Hill.
109. Nordstrom, M., et al., *SU-8 cantilevers for bio/chemical sensing; Fabrication, characterisation and development of novel read-out methods*. Sensors, 2008. 8(3): p. 1595-1612.
110. Gelorme, J.D., Cox, . J. , and Gutierrez, S. A. R. , *Photoresist composition and printed circuit boards and packages made therewith* U.S.P. Office, Editor. 1989, International Business Machines Corporation (Armonk, NY)

111. Shaw, J.M., Gelome, J.D., Labianca, N.C., Conley, W.E., and Holmes, S.J., *Negative Photoresists for Optical Lithography*. IBM Journal of Research and Development, 1997. 41.
112. Lorenz, H., et al., *SU-8: a low-cost negative resist for MEMS*. Journal of Micromechanics and Microengineering, 1997. 7(3): p. 121-124.
113. Wong, W.H. and E.Y.B. Pun, *Exposure characteristics and three-dimensional profiling of SU8C resist using electron beam lithography*. Journal of Vacuum Science & Technology B, 2001. 19(3): p. 732-735.
114. Liu, C., *Recent developments in polymer MEMS*. Advanced Materials, 2007. 19(22): p. 3783-3790.
115. Feng, R. and R.J. Farris, *Influence of processing conditions on the thermal and mechanical properties of SU8 negative photoresist coatings*. Journal of Micromechanics and Microengineering, 2003. 13(1): p. 80-88.
116. Hopcroft, M., et al., *Micromechanical testing of SU-8 cantilevers*. Fatigue & Fracture of Engineering Materials & Structures, 2005. 28(8): p. 735-742.
117. Hennemeyer, M., et al., *Cell proliferation assays on plasma activated SU-8*. Microelectronic Engineering, 2008. 85(5-6): p. 1298-1301.
118. Voskerician, G., et al., *Biocompatibility and biofouling of MEMS drug delivery devices*. Biomaterials, 2003. 24(11): p. 1959-1967.
119. Pater, R.H., *THERMOSETTING POLYIMIDES - A REVIEW*. Sampe Journal, 1994. 30(5): p. 29-38.
120. Microsystems, H., *PI-2545 Wet Etch Polyimide*, in *Technical Bulletin*.
121. Inc., P.T.C. *Parylene Technology*. 2008 [cited; Available from: <http://www.parylene.com/technology/parylene-technology.html>].
122. Sedgwick, T.O., B.J. Agule, and A.N. Broers, *NOVEL METHOD FOR FABRICATION OF ULTRAFINE METAL LINERS BY ELECTRON-BEAMS*. Journal of the Electrochemical Society, 1972. 119(12): p. 1769-&.
123. Bassous, E., et al., *HIGH TRANSMISSION X-RAY MASKS FOR LITHOGRAPHIC APPLICATIONS*. Solid State Technology, 1976. 19(9): p. 55-58.
124. Hohm, D. and G. Hess, *A SUBMINIATURE CONDENSER MICROPHONE WITH SILICON-NITRIDE MEMBRANE AND SILICON BACK PLATE*. Journal of the Acoustical Society of America, 1989. 85(1): p. 476-480.
125. Albrecht, T.R., et al., *MICROFABRICATION OF CANTILEVER STYLI FOR THE ATOMIC FORCE MICROSCOPE*. Journal of Vacuum Science & Technology a-Vacuum Surfaces and Films, 1990. 8(4): p. 3386-3396.
126. Knotter, D.M. and T.J.J. Denteneer, *Etching mechanism of silicon nitride in HF-based solutions*. Journal of the Electrochemical Society, 2001. 148(3): p. F43-F46.
127. Ling, T.G.I., et al., *Fabrication and characterization of a molecular adhesive layer for micro- and nanofabricated electrochemical electrodes*. Microelectronic Engineering, 2003. 67-8: p. 887-892.
128. Hansen, C.L., M.O.A. Sommer, and S.R. Quake, *Systematic investigation of protein phase behavior with a microfluidic formulator*. Proceedings of the National Academy of Sciences of the United States of America, 2004. 101(40): p. 14431-14436.
129. Lee, J.N., et al., *Compatibility of mammalian cells on surfaces of poly(dimethylsiloxane)*. Langmuir, 2004. 20(26): p. 11684-11691.
130. Merkel, T.C., et al., *Gas sorption, diffusion, and permeation in poly(dimethylsiloxane)*. Journal of Polymer Science Part B-Polymer Physics, 2000. 38(3): p. 415-434.
131. Materials, G.S.M.P. *RTV 615*. [cited; Available from: <http://www.gesilicones.com/siliconesweb/am1/en/documents/datasheets/1854.html>].
132. Lee, J.N., C. Park, and G.M. Whitesides, *Solvent compatibility of poly(dimethylsiloxane)-based microfluidic devices*. Analytical Chemistry, 2003. 75(23): p. 6544-6554.

133. Eddington, D.T., J.P. Puccinelli, and D.J. Beebe, *Thermal aging and reduced hydrophobic recovery of polydimethylsiloxane*. Sensors and Actuators B-Chemical, 2006. 114(1): p. 170-172.
134. Park, J.Y., C.M. Hwang, and S.H. Lee, *Effective methods to improve the biocompatibility of poly (dimethylsiloxane)*. Biochip Journal, 2008. 2(1): p. 39-43.
135. Millet, L.J., et al., *Microfluidic devices for culturing primary mammalian neurons at low densities*. Lab on a Chip, 2007. 7(8): p. 987-994.
136. Ozinsky, A. 2008.
137. Hansen, C.L., and Taylor, J. 2008.
138. Heo, Y.S., et al., *Characterization and resolution of evaporation-mediated osmolality shifts that constrain microfluidic cell culture in poly(dimethylsiloxane) devices*. Analytical Chemistry, 2007. 79(3): p. 1126-1134.
139. Batchelor, G.K., *An Introduction to Fluid Dynamics*. 1967, New York, NY: cambridge University Press.
140. Chien, S., S. Li, and J.Y.J. Shyy. *Effects of mechanical forces on signal transduction and gene expression in endothelial cells*. 1998: Lippincott Williams & Wilkins.
141. Papadaki, M. and S.G. Eskin, *Effects of fluid shear stress on gene regulation of vascular cells*. Biotechnology Progress, 1997. 13(3): p. 209-221.
142. Purcell, E.M., *LIFE AT LOW REYNOLDS-NUMBER*. American Journal of Physics, 1977. 45(1): p. 3-11.
143. Squires, T.M. and S.R. Quake, *Microfluidics: Fluid physics at the nanoliter scale*. Reviews of Modern Physics, 2005. 77(3): p. 977-1026.
144. Toepke, M.W. and D.J. Beebe, *PDMS absorption of small molecules and consequences in microfluidic applications*. Lab on a Chip, 2006. 6(12): p. 1484-1486.
145. BASF, *Pluronic® F127 Block Copolymer Surfactant*, in *Technical Bulletin*. 2002: Mount Olive.
146. Tan, J.L., et al., *Simple approach to micropattern cells on common culture substrates by tuning substrate wettability*. Tissue Engineering, 2004. 10(5-6): p. 865-872.
147. Torres, A.J., et al., *Nanobiotechnology and cell biology: Micro- and nanofabricated surfaces to investigate receptor-mediated signaling*. Annual Review of Biophysics, 2008. 37: p. 265-288.
148. Liu, W.F. and C.S. Chen, *Cellular and multicellular form and function*. Advanced Drug Delivery Reviews, 2007. 59(13): p. 1319-1328.
149. Deshpande, V.S., et al., *A bio-mechanical model for coupling cell contractility with focal adhesion formation*. Journal of the Mechanics and Physics of Solids, 2008. 56(4): p. 1484-1510.
150. They, M., et al., *The extracellular matrix guides the orientation of the cell division axis*. Nature Cell Biology, 2005. 7(10): p. 947-U29.
151. Parker, K.K., et al., *Directional control of lamellipodia extension by constraining cell shape and orienting cell tractional forces*. Faseb Journal, 2002. 16(10): p. 10.
152. Kadler, K.E., A. Hill, and E.G. Canty-Laird, *Collagen fibrillogenesis: fibronectin, integrins, and minor collagens as organizers and nucleators*. Current Opinion in Cell Biology, 2008. 20(5): p. 495-501.
153. Berrier, A.L. and K.M. Yamada, *Cell-matrix adhesion*. Journal of Cellular Physiology, 2007. 213(3): p. 565-573.
154. Canaria, C.A., et al., *Formation and removal of alkylthiolate self-assembled monolayers on gold in aqueous solutions*. Lab on a Chip, 2006. 6(2): p. 289-295.
155. Vulto, P., et al., *Microfluidic channel fabrication in dry film resist for production and prototyping of hybrid chips*. Lab on a Chip, 2005. 5(2): p. 158-162.
156. Xie, J., et al., *Surface micromachined electrostatically actuated micro peristaltic pump*. Lab on a Chip, 2004. 4(5): p. 495-501.

157. Chen, P.J., C.Y. Shih, and Y.C. Tai, *Design, fabrication and characterization of monolithic embedded parylene microchannels in silicon substrate*. Lab on a Chip, 2006. 6(6): p. 803-810.
158. Gomez-Sjoberg, R. 2008.
159. Wang, Z.H., et al., *High-density microfluidic arrays for cell cytotoxicity analysis*. Lab on a Chip, 2007. 7(6): p. 740-745.
160. Jeon, N.L., et al., *Neutrophil chemotaxis in linear and complex gradients of interleukin-8 formed in a microfabricated device*. Nature Biotechnology, 2002. 20(8): p. 826-830.
161. Hung, P.J., et al., *Continuous perfusion microfluidic cell culture array for high-throughput cell-based assays*. Biotechnology and Bioengineering, 2005. 89(1): p. 1-8.
162. Thompson, D.M., et al., *Dynamic gene expression profiling using a microfabricated living cell array*. Analytical Chemistry, 2004. 76(14): p. 4098-4103.
163. Z. T. F. Yu, K.K., C. J. Shu, R. Silverman, C. G. Radu, O. N. Witte, H.-R. Tseng *Integrated Microfluidic Chip for Parallel Culture and Multiparametric Analysis of Murine and Human Cell Lines*. Submitted, 2008.
164. Tseng, H.-R., Kamei, K., Yu, T. F., Guo, S., Witte, O. N., Radu, C., and Suh, J., *Microfluidic Platform for Cell Culture and Assay*, U.S.P. Office, Editor. 2008.
165. Taylor, A.M., et al., *A microfluidic culture platform for CNS axonal injury, regeneration and transport*. Nature Methods, 2005. 2(8): p. 599-605.
166. Meyvantsson, I., et al., *Automated cell culture in high density tubeless microfluidic device arrays*. Lab on a Chip, 2008. 8(5): p. 717-724.
167. Freshney, R.I., *Culture of Animal Cells, A Manual of Basic Technique*. 4th ed. 2000, New York: John Wiley & Sons.
168. Walker, G.M., H.C. Zeringue, and D.J. Beebe, *Microenvironment design considerations for cellular scale studies*. Lab on a Chip, 2004. 4(2): p. 91-97.
169. Lepezuniga, J.L., J.S. Zigler, and I. Gery, *TOXICITY OF LIGHT-EXPOSED HEPES MEDIA*. Journal of Immunological Methods, 1987. 103(1): p. 145-145.
170. Mukhopadhyay, R., *When PDMS isn't the best*. Analytical Chemistry, 2007. 79(9): p. 3248-3253.
171. Stamenovic, D., *Rheological behavior of mammalian cells*. Cellular and Molecular Life Sciences, 2008. 65(22): p. 3592-3605.
172. Foissner, I. and G.O. Wasteneys, *Wide-ranging effects of eight cytochalasins and latrunculin A and B on intracellular motility and actin filament reorganization in characean internodal cells*. Plant and Cell Physiology, 2007. 48(4): p. 585-597.
173. Brenner, S.L. and E.D. Korn, *SUBSTOICHIOMETRIC CONCENTRATIONS OF CYTOCHALASIN-D INHIBIT ACTIN POLYMERIZATION - ADDITIONAL EVIDENCE FOR AN F-ACTIN TREADMILL*. Journal of Biological Chemistry, 1979. 254(20): p. 9982-9985.
174. Brown, S.S. and J.A. Spudich, *CYTOCHALASIN INHIBITS THE RATE OF ELONGATION OF ACTIN FILAMENT FRAGMENTS*. Journal of Cell Biology, 1979. 83(3): p. 657-662.
175. Flanagan, M.D. and S. Lin, *CYTOCHALASINS BLOCK ACTIN FILAMENT ELONGATION BY BINDING TO HIGH-AFFINITY SITES ASSOCIATED WITH F-ACTIN*. Journal of Biological Chemistry, 1980. 255(3): p. 835-838.
176. Macleanfletcher, S. and T.D. Pollard, *MECHANISM OF ACTION OF CYTOCHALASIN-B ON ACTIN*. Cell, 1980. 20(2): p. 329-341.
177. Pollard, T.D. and M.S. Mooseker, *DIRECT MEASUREMENT OF ACTIN POLYMERIZATION RATE CONSTANTS BY ELECTRON-MICROSCOPY OF ACTIN-FILAMENTS NUCLEATED BY ISOLATED MICROVILLUS CORES*. Journal of Cell Biology, 1981. 88(3): p. 654-659.
178. Wakatsuki, T., et al., *Effects of cytochalasin D and latrunculin B on mechanical properties of cells*. Journal of Cell Science, 2001. 114(5): p. 1025-1036.

179. Bonder, E.M. and M.S. Mooseker, *CYTOCHALASIN-B SLOWS BUT DOES NOT PREVENT MONOMER ADDITION AT THE BARBED END OF THE ACTIN FILAMENT*. Journal of Cell Biology, 1986. 102(1): p. 282-288.
180. Goddette, D.W. and C. Frieden, *ACTIN POLYMERIZATION - THE MECHANISM OF ACTION OF CYTOCHALASIN-D*. Journal of Biological Chemistry, 1986. 261(34): p. 5974-5980.
181. Goddette, D.W. and C. Frieden, *THE KINETICS OF CYTOCHALASIN D BINDING TO MONOMERIC ACTIN*. Journal of Biological Chemistry, 1986. 261(34): p. 5970-5973.
182. Carrier, M.F., et al., *INTERACTION OF CYTOCHALASIN-D WITH ACTIN-FILAMENTS IN THE PRESENCE OF ADP AND ATP*. Journal of Biological Chemistry, 1986. 261(5): p. 2041-2050.
183. Sampath, P. and T.D. Pollard, *EFFECTS OF CYTOCHALASIN, PHALLOIDIN, AND PH ON THE ELONGATION OF ACTIN-FILAMENTS*. Biochemistry, 1991. 30(7): p. 1973-1980.
184. Edds, K.T., *EFFECTS OF CYTOCHALASIN AND COLCEMID ON CORTICAL FLOW IN CELOMOCYTES*. Cell Motility and the Cytoskeleton, 1993. 26(3): p. 262-273.
185. Henson, J.H., et al., *Two components of actin-based retrograde flow in sea urchin coelomocytes*. Molecular Biology of the Cell, 1999. 10(12): p. 4075-4090.
186. Mortensen, K. and L.I. Larsson, *Effects of cytochalasin D on the actin cytoskeleton: association of neoformed actin aggregates with proteins involved in signaling and endocytosis*. Cellular and Molecular Life Sciences, 2003. 60(5): p. 1007-1012.
187. Forscher, P. and S.J. Smith, *ACTIONS OF CYTOCHALASINS ON THE ORGANIZATION OF ACTIN-FILAMENTS AND MICROTUBULES IN A NEURONAL GROWTH CONE*. Journal of Cell Biology, 1988. 107(4): p. 1505-1516.
188. Bray, D. and J.G. White, *CORTICAL FLOW IN ANIMAL-CELLS*. Science, 1988. 239(4842): p. 883-888.
189. Pollard, T.D. and G.G. Borisy, *Cellular motility driven by assembly and disassembly of actin filaments*. Cell, 2003. 112(4): p. 453-465.
190. Medeiros, N.A., D.T. Burnette, and P. Forscher, *Myosin II functions in actin-bundle turnover in neuronal growth cones*. Nature Cell Biology, 2006. 8(3): p. 215-226.
191. Ponti, A., et al., *Two distinct actin networks drive the protrusion of migrating cells*. Science, 2004. 305(5691): p. 1782-1786.
192. Watanabe, N. and T.J. Mitchison, *Single-molecule speckle analysis of Aactin filament turnover in lamellipodia*. Science, 2002. 295(5557): p. 1083-1086.
193. Verkhovskiy, A.B., T.M. Svitkina, and G.G. Borisy, *Self-polarization and directional motility of cytoplasm*. Current Biology, 1999. 9(1): p. 11-20.
194. Paul, M.R., M.T. Clark, and M.C. Cross, *The stochastic dynamics of micron and nanoscale elastic cantilevers in fluid: fluctuations from dissipation*. Nanotechnology, 2006. 17(17): p. 4502-4513.
195. Paul, M.R. and M.C. Cross, *Stochastic dynamics of nanoscale mechanical oscillators immersed in a viscous fluid*. Physical Review Letters, 2004. 92(23).
196. Gupton, S.L. and C.M. Waterman-Storer, *Spatiotemporal feedback between actomyosin and focal-adhesion systems optimizes rapid cell migration*. Cell, 2006. 125(7): p. 1361-1374.
197. Koestler, S.A., et al., *Differentially oriented populations of actin filaments generated in lamellipodia collaborate in pushing and pausing at the cell front*. Nature Cell Biology, 2008. 10(3): p. 306-U33.
198. Kerssemakers, J.W.J., et al., *Assembly dynamics of microtubules at molecular resolution*. Nature, 2006. 442(7103): p. 709-712.
199. Higuchi, H. and Y.E. Goldman, *SLIDING DISTANCE BETWEEN ACTIN AND MYOSIN-FILAMENTS PER ATP MOLECULE HYDROLYZED IN SKINNED MUSCLE-FIBERS*. Nature, 1991. 352(6333): p. 352-354.

200. Yanagida, T., M. Iwaki, and Y. Ishii, *Single molecule measurements and molecular motors*. Philosophical Transactions of the Royal Society B-Biological Sciences, 2008. 363(1500): p. 2123-2134.
201. Leduc, C., et al., *Detection of fractional steps in cargo movement by the collective operation of kinesin-1 motors*. Proceedings of the National Academy of Sciences of the United States of America, 2007. 104(26): p. 10847-10852.
202. Klumpp, S. and R. Lipowsky, *Cooperative cargo transport by several molecular motors*. Proceedings of the National Academy of Sciences of the United States of America, 2005. 102(48): p. 17284-17289.
203. Balaban, N.Q., et al., *Force and focal adhesion assembly: a close relationship studied using elastic micropatterned substrates*. Nature Cell Biology, 2001. 3(5): p. 466-472.
204. Nicolas, A., B. Geiger, and S.A. Safran, *Cell mechanosensitivity controls the anisotropy of focal adhesions*. Proceedings of the National Academy of Sciences of the United States of America, 2004. 101(34): p. 12520-12525.
205. Riveline, D., et al., *Focal contacts as mechanosensors: Externally applied local mechanical force induces growth of focal contacts by an mDia1-dependent and ROCK-independent mechanism*. Journal of Cell Biology, 2001. 153(6): p. 1175-1185.
206. Schwarz, U.S., T. Erdmann, and I.B. Bischofs, *Focal adhesions as mechanosensors: The two-spring model*. Biosystems, 2006. 83(2-3): p. 225-232.
207. Xia, N., et al., *Directional control of cell motility through focal adhesion positioning and spatial control of Rac activation*. FASEB Journal, 2008. 22(6): p. 1649-1659.
208. Elliott, G.F. and C.R. Worthington, *The muscle motor: 'simultaneous' levers or sequential impulses?* International Journal of Biological Macromolecules, 1997. 21(3): p. 271-275.
209. Redaelli, A., M. Soncini, and F.M. Montevecchi, *Myosin cross-bridge mechanics: geometrical determinants for continuous sliding*. Journal of Biomechanics, 2001. 34(12): p. 1607-1617.
210. Eisenberg, E. and L.E. Greene, *RELATION OF MUSCLE BIOCHEMISTRY TO MUSCLE PHYSIOLOGY*. Annual Review of Physiology, 1980. 42: p. 293-309.
211. Baker, J.E. and D.D. Thomas, *Thermodynamics and kinetics of a molecular motor ensemble*. Biophysical Journal, 2000. 79(4): p. 1731-1736.
212. Julicher, F. and J. Prost, *COOPERATIVE MOLECULAR MOTORS*. Physical Review Letters, 1995. 75(13): p. 2618-2621.
213. Campas, O., et al., *Collective dynamics of interacting molecular motors*. Physical Review Letters, 2006. 97(3).
214. Dudaicevs, H., et al., *SURFACE MICROMACHINED PRESSURE SENSORS WITH INTEGRATED CMOS READ-OUT ELECTRONICS*. Sensors and Actuators a-Physical, 1994. 43(1-3): p. 157-163.
215. Paul, O. and H. Baltes, *NOVEL FULLY CMOS-COMPATIBLE VACUUM SENSOR*. Sensors and Actuators a-Physical, 1995. 46(1-3): p. 143-146.
216. Scheiter, T., et al., *Full integration of a pressure-sensor system into a standard BiCMOS process*. Sensors and Actuators a-Physical, 1998. 67(1-3): p. 211-214.
217. Usui, T., *Actin- and microtubule-targeting bioprobes: Their binding sites and inhibitory mechanisms*. Bioscience Biotechnology and Biochemistry, 2007. 71(2): p. 300-308.
218. Fenteany, G. and S.T. Zhu, *Small-molecule inhibitors of actin dynamics and cell motility*. Current Topics in Medicinal Chemistry, 2003. 3(6): p. 593-616.
219. Garcia-Manyes, S., et al., *Force-clamp spectroscopy of single-protein monomers reveals the individual unfolding and folding pathways of I27 and ubiquitin*. Biophysical Journal, 2007. 93(7): p. 2436-2446.
220. Sarkar, A., S. Caamano, and J.M. Fernandez, *The mechanical fingerprint of a parallel polyprotein dimer*. Biophysical Journal, 2007. 92(4): p. L36-L38.

221. Ainavarapu, S.R.K., et al., *A single-molecule assay to directly identify solvent-accessible disulfide bonds and probe their effect on protein folding*. Journal of the American Chemical Society, 2008. 130(2): p. 436-+.
222. Coue, M., et al., *INHIBITION OF ACTIN POLYMERIZATION BY LATRUNCULIN-A*. Febs Letters, 1987. 213(2): p. 316-318.
223. Yarmola, E.G., et al., *Actin-latrunculin A structure and function - Differential modulation of actin-binding protein function by latrunculin A*. Journal of Biological Chemistry, 2000. 275(36): p. 28120-28127.
224. Bubb, M.R., et al., *Effects of jasplakinolide on the kinetics of actin polymerization - An explanation for certain in vivo observations*. Journal of Biological Chemistry, 2000. 275(7): p. 5163-5170.
225. Cramer, L.P., *Role of actin-filament disassembly in lamellipodium protrusion in motile cells revealed using the drug jasplakinolide*. Current Biology, 1999. 9(19): p. 1095-1105.
226. Ruppel, K.M. and J.A. Spudich, *Structure-function analysis of the motor domain of myosin*. Annual Review of Cell and Developmental Biology, 1996. 12: p. 543-573.
227. Kovacs, M., et al., *Mechanism of blebbistatin inhibition of myosin II*. Journal of Biological Chemistry, 2004. 279(34): p. 35557-35563.
228. Allingham, J.S., R. Smith, and I. Rayment, *The structural basis of blebbistatin inhibition and specificity for myosin II*. Nature Structural & Molecular Biology, 2005. 12(4): p. 378-379.
229. Stull, J.T., et al., *VASCULAR SMOOTH-MUSCLE CONTRACTILE ELEMENTS - CELLULAR-REGULATION*. Hypertension, 1991. 17(6): p. 723-732.
230. Krylyshkina, O., et al., *Nanometer targeting of microtubules to focal adhesions*. Journal of Cell Biology, 2003. 161(5): p. 853-859.
231. Wani, M.C., et al., *PLANT ANTITUMOR AGENTS .6. ISOLATION AND STRUCTURE OF TAXOL, A NOVEL ANTILEUKEMIC AND ANTITUMOR AGENT FROM TAXUS-BREVIFOLIA*. Journal of the American Chemical Society, 1971. 93(9): p. 2325-&.
232. Schiff, P.B. and S.B. Horwitz, *TAXOL STABILIZES MICROTUBULES IN MOUSE FIBROBLAST CELLS*. Proceedings of the National Academy of Sciences of the United States of America-Biological Sciences, 1980. 77(3): p. 1561-1565.
233. Pryor, D.E., et al., *The microtubule stabilizing agent laulimalide does not bind in the taxoid site, kills cells resistant to paclitaxel and epothilones, and may not require its epoxide moiety for activity*. Biochemistry, 2002. 41(29): p. 9109-9115.
234. Ishiguro, J. and Y. Uhara, *ISOLATION AND CHARACTERIZATION OF MUTANTS SUPERSENSITIVE TO THE SPINDLE POISON, ISOPROPYL N-3-CHLOROPHENYL CARBAMATE (CIPC) IN THE FISSION YEAST SCHIZOSACCHAROMYCES-POMBE*. Japanese Journal of Genetics, 1992. 67(2): p. 97-109.
235. Cavalcanti-Adam, E.A., et al., *Cell adhesion and response to synthetic nanopatterned environments by steering receptor clustering and spatial location*. Hfsp Journal, 2008. 2(5): p. 276-285.
236. Sethi, K.K., et al., *Contraction-mediated pinocytosis of RGD-peptide by dermal fibroblasts: inhibition of matrix attachment blocks contraction and disrupts microfilament organisation*. Cell Motility and the Cytoskeleton, 2002. 52(4): p. 231-241.
237. Ridley, A.J., et al., *THE SMALL GTP-BINDING PROTEIN RAC REGULATES GROWTH-FACTOR INDUCED MEMBRANE RUFFLING*. Cell, 1992. 70(3): p. 401-410.
238. Ridley, A.J. and A. Hall, *THE SMALL GTP-BINDING PROTEIN RHO REGULATES THE ASSEMBLY OF FOCAL ADHESIONS AND ACTIN STRESS FIBERS IN RESPONSE TO GROWTH-FACTORS*. Cell, 1992. 70(3): p. 389-399.
239. Hall, A., *Rho GTPases and the actin cytoskeleton*. Science, 1998. 279(5350): p. 509-514.

240. Etienne-Manneville, S. and A. Hall, *Rho GTPases in cell biology*. Nature, 2002. 420(6916): p. 629-635.
241. Burridge, K. and K. Wennerberg, *Rho and Rac take center stage*. Cell, 2004. 116(2): p. 167-179.
242. Chrzanowska-Wodnicka, M. and K. Burridge, *Rho-stimulated contractility drives the formation of stress fibers and focal adhesions*. Journal of Cell Biology, 1996. 133(6): p. 1403-1415.
243. Hart, M.J., et al., *Direct stimulation of the guanine nucleotide exchange activity of p115 RhoGEF by G alpha(13)*. Science, 1998. 280(5372): p. 2112-2114.
244. Kozasa, T., et al., *p115 RhoGEF, a GTPase activating protein for G alpha(12) and G alpha(13)*. Science, 1998. 280(5372): p. 2109-2111.
245. Watanabe, N., et al., *Cooperation between mDia1 and ROCK in Rho-induced actin reorganization*. Nature Cell Biology, 1999. 1(3): p. 136-143.
246. Barbieri, J.T., M.J. Riese, and K. Aktories, *Bacterial toxins that modify the actin cytoskeleton*. Annual Review of Cell and Developmental Biology, 2002. 18: p. 315-344.
247. Itoh, K., et al., *An essential part for Rho-associated kinase in the transcellular invasion of tumor cells*. Nature Medicine, 1999. 5(2): p. 221-225.
248. Kempiak, S.J., et al., *A neural Wiskott-Aldrich syndrome protein-mediated pathway for localized activation of actin polymerization that is regulated by cortactin*. Journal of Biological Chemistry, 2005. 280(7): p. 5836-5842.
249. Clark, K., et al., *Myosin II and mechanotransduction: a balancing act*. Trends in Cell Biology, 2007. 17(4): p. 178-186.
250. Ingber, D.E., *Cellular mechanotransduction: putting all the pieces together again*. FASEB Journal, 2006. 20(7): p. 811-827.
251. Tan, J.L.a.C., C.S. 2005.
252. Bischofs, I.B. and U.S. Schwarz, *Cell organization in soft media due to active mechanosensing*. Proceedings of the National Academy of Sciences of the United States of America, 2003. 100(16): p. 9274-9279.
253. Haston, W.S., J.M. Shields, and P.C. Wilkinson, *THE ORIENTATION OF FIBROBLASTS AND NEUTROPHILS ON ELASTIC SUBSTRATA*. Experimental Cell Research, 1983. 146(1): p. 117-126.
254. Bell, E., B. Ivarsson, and C. Merrill, *PRODUCTION OF A TISSUE-LIKE STRUCTURE BY CONTRACTION OF COLLAGEN LATTICES BY HUMAN-FIBROBLASTS OF DIFFERENT PROLIFERATIVE POTENTIAL INVITRO*. Proceedings of the National Academy of Sciences of the United States of America, 1979. 76(3): p. 1274-1278.
255. Eastwood, M., et al., *Effect of precise mechanical loading on fibroblast populated collagen lattices: Morphological changes*. Cell Motility and the Cytoskeleton, 1998. 40(1): p. 13-21.
256. Takakuda, K. and H. Miyairi, *Tensile behaviour of fibroblasts cultured in collagen gel*. Biomaterials, 1996. 17(14): p. 1393-1397.
257. Marganski, W.A., M. Dembo, and Y.L. Wang, *Measurements of cell-generated deformations on flexible substrata using correlation-based optical flow, in Biophotonics, Pt B*. 2003. p. 197-211.
258. Bruinsma, R., *Theory of force regulation by Nascent adhesion sites*. Biophysical Journal, 2005. 89(1): p. 87-94.
259. Storm, C., et al., *Nonlinear elasticity in biological gels*. Nature, 2005. 435(7039): p. 191-194.
260. Giannone, G. and M.P. Sheetz, *Substrate rigidity and force define form through tyrosine phosphatase and kinase pathways*. Trends in Cell Biology, 2006. 16(4): p. 213-223.
261. Tamada, M., M.P. Sheetz, and Y. Sawada, *Activation of a signaling cascade by cytoskeleton stretch*. Developmental Cell, 2004. 7(5): p. 709-718.

262. Geiger, B., *A role for p130Cas in mechanotransduction*. Cell, 2006. 127(5): p. 879-881.
263. Korn, K. and E. Krausz, *Cell-based high-content screening of small-molecule libraries*. Current Opinion in Chemical Biology, 2007. 11(5): p. 503-510.
264. Jordan, A., et al., *Tubulin as a target for anticancer drugs: Agents which interact with the mitotic spindle*. Medicinal Research Reviews, 1998. 18(4): p. 259-296.
265. Abraham, V.C., D.L. Taylor, and J.R. Haskins, *High content screening applied to large-scale cell biology*. Trends in Biotechnology, 2004. 22(1): p. 15-22.
266. Hong, J., *Microfluidic systems for high throughput screening*. Biochip Journal, 2008. 2(1): p. 12-26.
267. Wen, Y. and S.T. Yang, *The future of microfluidic assays in drug development*. Expert Opinion on Drug Discovery, 2008. 3(10): p. 1237-1253.
268. Yarrow, J.C., et al., *Phenotypic screening of small molecule libraries by high throughput cell imaging*. Combinatorial Chemistry & High Throughput Screening, 2003. 6(4): p. 279-286.
269. Eggert, U.S. and T.J. Mitchison, *Small molecule screening by imaging*. Current Opinion in Chemical Biology, 2006. 10(3): p. 232-237.
270. Nicholson, R.L., et al., *Small-molecule screening: Advances in microarraying and cell-imaging technologies*. Acs Chemical Biology, 2007. 2(1): p. 24-30.
271. Wakatsuki, T., J.A. Fee, and E.L. Elson, *Phenotypic screening for pharmaceuticals using tissue constructs*. Current Pharmaceutical Biotechnology, 2004. 5(2): p. 181-189.
272. Vandeburgh, H., et al. *Drug-screening platform based on the contractility of tissue-engineered muscle*. 2008: John Wiley & Sons Inc.
273. Axelrod, B.W.a.R., M. L., *Micro-Fluidics Embedded Polymer NEMS Force Sensors Applied to Phenotypic Screening for Pharmaceuticals*, U.S.P. Office, Editor. 2008.